

HYDROGEN EMBRITTLEMENT TESTING OF AUSTENITIC
STAINLESS STEELS SUS 316 AND 316L

by

DARREN MICHAEL BROMLEY

B.A.Sc., The University of British Columbia, 2005

A THESIS SUBMITTED IN PARTIAL FULFILLMENT OF
THE REQUIREMENTS FOR THE DEGREE OF

MASTER OF APPLIED SCIENCE

in

THE FACULTY OF GRADUATE STUDIES

(Materials Engineering)

THE UNIVERSITY OF BRITISH COLUMBIA

(Vancouver)

April 2008

© Darren Michael Bromley, 2008

Abstract

The imminent emergence of the hydrogen fuel industry has resulted in an urgent mandate for very specific material testing. Although storage of pressurized hydrogen gas is both practical and attainable, demands for increasing storage pressures (currently around 70 MPa) continue to present unexpected material compatibility issues. It is imperative that materials commonly used in gaseous hydrogen service are properly tested for hydrogen embrittlement resistance. To assess material behavior in a pressurized hydrogen environment, procedures were designed to test materials for susceptibility to hydrogen embrittlement.

Of particular interest to the field of high-pressure hydrogen in the automotive industry, austenitic stainless steels SUS 316 and 316L were used to validate the test programs. Tests were first performed in 25 MPa helium and hydrogen at room temperature and at -40°C. Tests in a 25 MPa hydrogen atmosphere caused embrittlement in SUS 316, but not in 316L. This indicated that alloys with higher stacking fault energies (316L) are more resistant to hydrogen embrittlement. Decreasing the test temperature caused slight embrittlement in 316L and significantly enhanced it in 316. Alternatively, a second set of specimens was immersed in 70 MPa hydrogen at 100°C until reaching a uniform concentration of absorbed hydrogen. Specimens were then loaded in tension to failure to determine if a bulk saturation of hydrogen provided a similar embrittling effect. Neither material succumbed to the effects of gaseous pre-charging, indicating that the embrittling mechanism requires a constant supply of hydrogen at the material surface rather than having bulk concentration of dissolved hydrogen. Permeation tests were also performed to ensure that hydrogen penetrated the samples and to develop material specific permeation constants.

To pave the way for future work, prototype equipment was constructed allowing tensile or fatigue tests to be performed at much higher hydrogen pressures. To determine the effect of pressure on hydrogen embrittlement, additional tests can be performed in hydrogen pressures up to 85 MPa hydrogen. The equipment will also allow for cyclic loading of notched tensile or compact tension specimens for fatigue studies.

Table of Contents

Abstract.....	ii
Table of Contents.....	iii
List of Tables.....	v
List of Figures.....	vi
List of Abbreviations.....	ix
List of Symbols.....	x
1.0 Introduction.....	1
2.0 Literature Review.....	3
2.1 Mechanism of Hydrogen Ingress.....	3
2.1.1 Electrolytic Hydrogen Charging.....	4
2.1.2 Gaseous Hydrogen Charging.....	4
2.2 Proposed Mechanisms of Hydrogen Embrittlement.....	5
2.2.1 Hydrogen-Enhanced Decohesion.....	5
2.2.2 Hydrogen-Enhanced Localized Plasticity.....	7
2.2.3 Hydride-Induced Embrittlement (HIE).....	9
2.3 Effect of Strain Rate on Hydrogen Embrittlement.....	10
2.4 Hydrogen's Effect on Austenite Stability.....	11
2.4.1 The Martensite Phase Transformation.....	12
2.4.2 Phase Transformation from Hydrogen Charging.....	14
2.4.3 Change in M_s and M_d Temperatures.....	15
2.4.4 Decrease in Stacking Fault Energy.....	17
2.5 Martensite's Role in Hydrogen Embrittlement.....	18
2.5.1 Opposing Arguments.....	18
2.5.2 Supporting Arguments.....	19
2.5.3 Comparison of Views.....	21
3.0 Scope and Objectives.....	23
4.0 Experimental Design and Development.....	24
4.1 Materials Tested.....	24
4.2 Hydrogen Environment Tensile Tests.....	25
4.3 Bulk Material Hydrogen Effects.....	31
4.3.1 Permeation Tests.....	31
4.3.2 Tensile Tests.....	36
4.4 Martensite Content Analysis.....	41
4.4.1 Ferritescope Validity Testing.....	42
4.4.2 Magnetic Measurement Procedure.....	45
4.5 Microscopy.....	51
5.0 Results.....	53
5.1 Hydrogen Environment Tensile Tests.....	53
5.1.1 Tensile Test Results.....	53
5.1.2 Stereo Microscopy.....	58
5.1.3 Optical Microscopy.....	60
5.1.4 Scanning Electron Microscopy.....	65
5.1.5 Martensite Content Analysis.....	69

5.2	Hydrogen Charge Tensile Tests.....	69
5.2.1	Permeation Test Results.....	70
5.2.2	Tensile Test Results	70
5.2.3	Scanning Electron Microscopy	74
6.0	Discussion	78
6.1	Permeation Properties of SS 316L	78
6.2	Phase Stability and Hydrogen Embrittlement.....	81
6.3	Martensite's Role in Hydrogen Embrittlement.....	82
6.4	Surface Versus Bulk Hydrogen Concentration.....	83
6.5	Effect of Temperature on Hydrogen Embrittlement.....	84
7.0	Future Work	87
8.0	Conclusions.....	89
	References.....	91

List of Tables

Table 1: SUS 316 and 316L chemical compositions	24
Table 2: Initial geometry measurements	26
Table 3: Tension test parameters	27
Table 4: Parameters used in calculation of maximum permeation pressure	36
Table 5: Thin tensile test conditions	41
Table 6: Mechanical properties of SS 301LN	42
Table 7: Martensite measurement results	44
Table 8: Reference sample martensite measurements	48
Table 9: Initial magnetic attraction measurements	51
Table 10: Summary of tensile test results for SUS 316	56
Table 11: Summary of tensile test results for SUS 316L	57
Table 12: Martensite content of fractured tensile specimens	69
Table 13: Hydrogen charge tensile test results	73
Table 14: Measured permeability values	79

List of Figures

Figure 1: Carbon fibre fully wrapped tank with SS 316 liner.....	2
Figure 2: Effect of absorbed hydrogen on the shear stress of dislocation interaction	8
Figure 3: Variation in normalized dislocation velocity with hydrogen gas pressure	9
Figure 4: Ratio of fracture load in hydrogen to air versus displacement rate.....	11
Figure 5: Variation of SFE of SS 304 with temperature change	13
Figure 6: Martensite transformation regimes.....	16
Figure 7: Round tensile specimen geometry.....	25
Figure 8: Integration of pressure vessel, environment chamber, and tensile test frame...	28
Figure 9: Setting balance point for load cell reading.....	29
Figure 10: Measured versus calculated strains	31
Figure 11: Permeation test setup schematic.....	32
Figure 12: Permeation sample jig	33
Figure 13: Diffusion of hydrogen through thin disk sample.....	34
Figure 14: Time to reach steady state hydrogen diffusion for SS 316.....	35
Figure 15: Strength of SS 316L as a function of temperature	36
Figure 16: Dimensions of thin tensile specimens	37
Figure 17: Hydrogen concentration profiles for samples stored in 70 MPa at 373 K	38
Figure 18: High-temperature hydrogen charge apparatus	39
Figure 19: Estimated desorption of hydrogen from a saturated sample in contact with a vacuum.....	40
Figure 20: Actual applied strains for ferritescope validity test.....	43
Figure 21: Diffraction patterns of deformed specimens	44
Figure 22: Martensite measurements from ferritescope and XRD	45
Figure 23: XRD scan of reference sample R1	47
Figure 24: XRD scan of reference sample R2	47
Figure 25: XRD scan of reference sample R3	48
Figure 26: Magnetic balance method test setup.....	49
Figure 27: Magnetic response of reference samples.....	50
Figure 28: 316 tested in 25 MPa He at 20°C	54
Figure 29: 316 tested in 25 MPa H ₂ at 20°C.....	54
Figure 30: 316 tested in 25 MPa He at -40°C	54
Figure 31: 316 tested in 25 MPa H ₂ at -40°C.....	54
Figure 32: 316L tested in 25 MPa He at 20°C	55
Figure 33: 316L tested in 25 MPa H ₂ at 20°C	55
Figure 34: 316L tested in 25 MPa He at -40°C.....	55
Figure 35: 316L tested in 25 MPa H ₂ at -40°C	55
Figure 36: Stress-strain behavior of SUS 316 tested in helium and hydrogen	56
Figure 37: Stress-strain behavior of SUS 316L tested in helium and hydrogen.....	57
Figure 38: 316 tested in 25 MPa He at 20°C (7x).....	58
Figure 39: 316 tested in 25 MPa H ₂ at 20°C (7x)	58
Figure 40: 316 tested in 25 MPa He at -40°C (7x)	59
Figure 41: 316 tested in 25 MPa H ₂ at -40°C (7x).....	59

Figure 42: 316L tested in 25 MPa He at 20°C (7x)	59
Figure 43: 316L tested in 25 MPa H ₂ at 20°C (7x).....	59
Figure 44: 316L tested in 25 MPa He at -40°C (7x)	60
Figure 45: 316L tested in 25 MPa H ₂ at -40°C (7x)	60
Figure 46: SS 316 microstructure as-received (200x)	61
Figure 47: SS 316L microstructure as-received (200x).....	61
Figure 48: Example of martensite distribution in hydrogen environment tensile sample	62
Figure 49: 316 tested in 25 MPa He at 20°C showing very little martensite (200x)	62
Figure 50: 316 tested in 25 MPa H ₂ at 20°C showing nearly no martensite (500x)	62
Figure 51: 316 tested in 25 MPa He at -40°C showing lots of martensite (500x)	63
Figure 52: 316 tested in 25 MPa H ₂ at -40°C showing lots of martensite (200x).....	63
Figure 53: 316L tested in 25 MPa He at 20°C showing almost no martensite (200x)	63
Figure 54: 316L tested in 25 MPa H ₂ at 20°C showing almost no martensite (200x).....	63
Figure 55: 316L tested in 25 MPa He at -40°C showing some martensite (200x)	63
Figure 56: 316L tested in 25 MPa H ₂ at -40°C showing some martensite (200x)	63
Figure 57: 316 tested in 25 MPa H ₂ at 20°C showing martensite ahead of a crack tip (500x).....	65
Figure 58: 316 tested in 25 MPa He at 20°C showing ductile fracture (1000x).....	66
Figure 59: 316 tested in 25 MPa H ₂ at 20°C showing brittle fracture (1000x).....	66
Figure 60: 316 tested in 25 MPa He at -40°C showing ductile fracture (1000x).....	66
Figure 61: 316 tested in 25 MPa H ₂ at -40°C showing brittle fracture (1000x)	66
Figure 62: 316 tested in 25 MPa H ₂ at -40°C showing ductile features near center (220x)	67
Figure 63: 316L tested in 25 MPa He at 20°C showing ductile fracture (1000x)	67
Figure 64: 316L tested in 25 MPa H ₂ at 20°C showing ductile fracture (1000x).....	67
Figure 65: 316L tested in 25 MPa He at -40°C showing ductile fracture (1000x)	68
Figure 66: 316L tested in 25 MPa H ₂ at -40°C showing ductile fracture (1000x).....	68
Figure 67: 316L tested in 25 MPa H ₂ at -40°C showing brittle-to-ductile transition (300x)	68
Figure 68: Permeation test results.....	70
Figure 69: 316 sample 1 tested as received	71
Figure 70: 316 sample 2 tested as received	71
Figure 71: 316 sample 3 charged in 100°C air.....	71
Figure 72: 316 sample 4 charged in 100°C air.....	71
Figure 73: 316 sample 5 charged in 100°C H ₂	71
Figure 74: 316 sample 6 charged in 100°C H ₂	71
Figure 75: 316L sample L1 tested as received.....	71
Figure 76: 316L sample L2 tested as received.....	71
Figure 77: 316L sample L3 charged in 100°C air.....	71
Figure 78: 316L sample L4 charged in 100°C air.....	71
Figure 79: 316L sample L5 charged in 100°C H ₂	71
Figure 80: 316L sample L6 charged in 100°C H ₂	71
Figure 81: Stress-strain curves of samples 1 through 6	72
Figure 82: Stress-strain curves of samples L1 through L6	73
Figure 83: Sample 1 tested as-received (300x).....	74
Figure 84: Sample 1 tested as-received (1000x).....	74

Figure 85: Sample 4 thermally aged (300x)	75
Figure 86: Sample 4 thermally aged (1000x)	75
Figure 87: Sample 6 hydrogen charged (300x).....	75
Figure 88: Sample 6 hydrogen charged (1000x).....	75
Figure 89: Sample L1 tested as-received (300x)	76
Figure 90: Sample L1 tested as-received (1000x)	76
Figure 91: Sample L4 thermally aged (300x)	76
Figure 92: Sample L4 thermally aged (1000x)	76
Figure 93: Sample L6 hydrogen charged (300x)	77
Figure 94: Sample L6 hydrogen charged (1000x)	77
Figure 95: Permeation test $\ln(P_H)$ versus $1/T$	80
Figure 96: Austenite phase stability grid	81
Figure 97: Surface crack experiencing dislocation emission versus crack propagation...	86

List of Abbreviations

BCC	Body centered cubic
COD	Crack-opening displacement
EDM	Electrical discharge machining
FCC	Face centered cubic
GC	Gas chromatograph
HCP	Hexagonal close packed
HEDE	Hydrogen-enhanced decohesion
HELP	Hydrogen-enhanced localized plasticity
HIE	Hydride-induced embrittlement
M_d	Highest temperature for strain-induced martensite
M_s	Highest temperature for spontaneous martensite formation
M_s^σ	Highest temperature for stress-assisted martensite
PTFE	Polytetrafluoroethylene
SEM	Scanning electron microscope
SFE	Stacking fault energy
SS	Stainless steel
TEM	Transmission electron microscope
XRD	X-ray diffraction

List of Symbols

A	Exposed area of permeation disk sample
b	Burgers vector
B_{meas}	Force of magnetic attraction
B_{ref}	Force of magnetic attraction of reference sample
$c_{\alpha'}$	α' -martensite concentration
$c_{\alpha' ref}$	α' -martensite concentration of reference sample
c_H	Local concentration of hydrogen
C_o	Hydrogen-to-metal atomic ratio
c_s	Concentration of hydrogen at the surface
C_{TS}	Terminal solid solubility
$C_{TS,0}$	Terminal solid solubility in absence of applied stress
D_H	Diffusivity of hydrogen through the metal
ϵ_f	Strain to failure for sub-sized tensile specimens
η	Hydrogen overpotential
E_d	Activation energy for diffusion
E_p	Activation energy for permeation
F	Applied force
F_c	Fracture load in hydrogen
F_m	Resistive force between atoms
F_o	Fracture load in air
γ	Number of hydrogen atoms in a metal hydride molecule
J	Hydrogen flux
k_{eff}	Effective spring constant
k_m	Spring constant of tensile test frame
k_s	Spring constant of specimen gauge section
L	Disk sample thickness
L_m	Deflection of tensile test frame
M_{ijkl}	Elastic compliance tensor
n	Number of hydrogen atoms in a metal hydride molecule
n_H	Moles of hydrogen
n_N	Moles of nitrogen
ν	Poisson's ratio
P	Hydrogen gas pressure
P_H	Permeability of hydrogen through a material
P_{max}	Maximum allowable gas pressure to avoid yielding
P_N	Nitrogen gas pressure
P_o	Permeability at absolute zero
Q	Amount of solute penetrating per unit area at a given time
R	Ideal gas constant
σ_{ij}	Applied stress tensor
σ_{kl}	Applied stress tensor
σ_{UTS}	Ultimate tensile strength
σ_{ys}	0.2% offset yield strength

σ_z	Local maximum tensile stress normal to the plane of a crack
T	Temperature
t	Exposure time
θ	Coverage of hydrogen on a surface
V_H	Partial molal volume of hydrogen
w_{acc}	Material strain energy per mole of hydride in absence of applied stress
w_{int}	Interaction energy per mole of hydride while under applied stress
x	Depth into sample

1.0 Introduction

The issue of hydrogen embrittlement has been prominent in discussions of welding, material processing, and corrosion for many years. With the potential for using hydrogen as a fuel, it is natural to question whether hydrogen will have the same detrimental effect on components incorporated in our personal fuel cells or related equipment.

Currently, austenitic stainless steel AISI 316 (SS 316) is the predominant material of construction for high-pressure hydrogen components and tubing, and has recently been incorporated into the construction of high-pressure hydrogen storage tank liners. A type-III storage tank consists of a metallic liner fully wrapped in glass or carbon fibres¹. The main function of the fibre is to provide the strength required to contain the pressure. Tanks with higher storage pressure capacity will typically use a carbon fibre wrap because glass fibres can be susceptible to stress corrosion cracking. The principal function of the liner is to prevent escape of the gas, although it will also offer contribution to the overall strength. On average, metallic liner materials are expected to sustain about 20% of the load imparted during pressurization¹. It is important for the liner material to have low permeability of hydrogen for containment of the gas, high toughness for impact resistance, and resistance to corrosion and hydrogen embrittlement, but would it would be an additional asset to have high strength for additional support during pressurization. Figure 1 shows an example of a type-III cylinder that incorporates a SS 316 liner.



Figure 1: Carbon fibre fully wrapped tank with SS 316 liner

Although hydrogen embrittlement has been recognized and researched as early as 1825, the governing mechanisms are still not clearly understood. The phenomenon has been well documented, and hundreds of investigations have been performed. General trends and concepts have formed and are used as guidelines in predicting the behavior of engineering alloys exposed to hydrogen². The interaction between hydrogen and metastable austenitic stainless steels is a unique case. Hydrogen can facilitate the phase transformation of austenite to martensite, and the martensite phase is suspected to be more susceptible to hydrogen embrittlement. Competing factors add to the complexity of the phenomenon, but must be examined in order to learn how to limit hydrogen's detrimental effect. It is of great importance to the hydrogen economy to reveal details of hydrogen's effect on austenitic stainless steel.

Currently, target pressures for on-board hydrogen storage are upwards of 70 MPa (10,000 psi). Further increasing complexity, high pressures alter the stress state and driving force for diffusion into the material, potentially changing the failure mechanism as well. As the allowable working pressure of hydrogen systems increases, materials must be re-examined to confirm their compatibility. The purpose of this thesis is to investigate the use of SS 316 in the high-pressure hydrogen industry.

2.0 Literature Review

Possessing a large internal hydrogen concentration and fluctuating pressures, metallic hydrogen components and storage cylinders are susceptible to formation of blisters or cracks on internal surfaces, both indications of hydrogen embrittlement. Such flaw initiation can be detrimental to the lifetime of a cylinder and, therefore, to the safety of its user. In order to prevent damage, it is essential to understand how it occurs. In this section, background will be provided on how hydrogen enters and moves through the metallic structure. The various mechanisms of embrittlement will be reviewed as well as the effect of strain rate. Hydrogen's influence on the austenite phase stability will be discussed with particular reference to martensite's role in the embrittlement process. Providing the relevant research to date will justify the need for the testing and research described in this master's thesis.

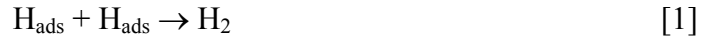
2.1 Mechanism of Hydrogen Ingress

Hydrogen is absorbed at the metallic surface as atomic hydrogen. The atomic hydrogen may form due to dissociation of gaseous (molecular) hydrogen at the metal surface due to reaction of metal hydrides, or may arise due to electrochemical reactions. The atomic hydrogen is transported by diffusion through the metallic lattice either interstitially or by dislocation movement².

The diffusion of hydrogen through lattice sites is primarily governed by a hydrogen chemical potential gradient. For a given region, this is affected both by the hydrogen concentration as well as the mechanical and chemical environment. For example, in regions of tensile hydrostatic stress, there is an increase in free volume so the chemical potential of interstitial hydrogen is low. Thus, such regions will tend to attract hydrogen atoms. Similarly, hydrogen may be trapped in the tensile field surrounding a dislocation and move with the dislocation motion. This generally constitutes a faster mode of transport and is primarily affected by plastic strain. With regards to hydrogen embrittlement testing, two methods are generally employed to infuse a material with hydrogen: electrolytic and gaseous charging.

2.1.1 Electrolytic Hydrogen Charging

When a metal is exposed to a hydrogen-containing environment, it is possible for hydrogen to be adsorbed onto the surface³. When the hydrogen-containing medium is aqueous, more severe conditions are encountered. This is due to the high fugacity involved with corrosion reactions³. As a hydrogen atom is adsorbed onto the surface of the metal, it will either combine with another to form hydrogen gas (equation 1) or it will be absorbed into the bulk of the material (equation 2)^{3,4}.



It is the energetics of a metal's surface that dictates which of the two reactions will occur³. The kinetics of the permeation is governed by the nature of the metal, applied potential, state of the cathodic surface, pH, and chemical composition of the charging solution⁵. Generally, the rate of reaction 2 is governed by the coverage of hydrogen on the steel surface, θ ^{3,5}. Chou and Makhoul³ report that since θ is directly proportional to the hydrogen overpotential, η , a surface with a higher value of hydrogen overpotential will have more adsorbed hydrogen atoms, and, thus, more hydrogen transported into the bulk of the metal.

Applying a current density provides added driving force for the diffusion of hydrogen. A very large hydrogen concentration is produced at the surface, but not as large a concentration in the bulk of the material. A similar state of material might be seen in processes such as electroplating, cathodic protection, acidic pickling, or welding, but gaseous exposure will provide a different gradient.

2.1.2 Gaseous Hydrogen Charging

In the hydrogen fueled vehicle industry, less severe conditions of hydrogen ingress will be encountered. This is mostly because much smaller gradients in absorbed hydrogen concentration will be present. In order to more accurately represent conditions

faced by the liner material for on-board storage of compressed hydrogen, test specimens should be gaseously charged.

Molecular hydrogen cannot enter into the stainless steel components in the molecular state. In order for hydrogen to be absorbed, the gas molecule, H_2 , must dissociate into two hydrogen atoms. This typically occurs due to the reaction of metal hydrides or from electrochemical reactions⁶. As reported by H.W. Liu and P.J. Ficalora⁷, an energy of 434.2 kJ/mol is required for the dissociation of a hydrogen gas molecule. It was proposed that the energy requirement may be supplemented at the specimen surface via a dislocation terminus. From here, the atomic hydrogen can be transported through the atomic lattice by diffusion or by dislocation movement.

In the case of high-pressure gaseous charging, diffusion is the main method of transport. Diffusion of hydrogen is driven both by temperature and chemical potential gradients⁸⁻¹⁰. Compared to electrolytic charging, gaseous charging provides a reduced concentration gradient more representative of what would be encountered in service.

2.2 Proposed Mechanisms of Hydrogen Embrittlement

Hydrogen embrittlement is a very complicated process with many underlying mechanisms. Often, failure will result from a combination of several influences, making the determination of governing mechanism very difficult. To date, three main embrittlement mechanisms have been proposed: hydrogen-enhanced decohesion (HEDE), hydrogen-enhanced localized plasticity (HELP), and hydride-induced embrittlement (HIE). In the following sections, each mechanism will be reviewed.

2.2.1 Hydrogen-Enhanced Decohesion

Early results from tests dealing with steel temper embrittlement show that there are chemical interactions of impurities with metallic components¹¹. This reveals that a transition from ductile to brittle fracture can depend on electrons and their bonding characteristics. As hydrogen is absorbed at an atomically sharp crack tip, there is a decrease in electron charge density between metal atoms^{12,13}. It has been claimed that there exists an electron transfer from the 1s band of hydrogen to the 3d and 4s bands of

the metal that decreases the cohesive energy (results are presented for both nickel and iron)^{11,14}. The final decohesion results from tensile separation of the atoms, which is planar in nature¹⁵. Fracture by the HEDE mechanism is characterized by limited activity of dislocations¹². By performing scanning electron microscopy, this becomes evident by the appearance of atomically flat fracture surfaces (i.e. the absence of microvoids and dimples).

Diffusion of hydrogen is influenced both by temperature and chemical potential gradients⁸⁻¹⁰. In this case, the chemical potential gradient refers to the force imposed on the atoms due to a concentration gradient. A lattice expansion caused by the hydrostatic tensile stress surrounding a crack tip locally reduces the effective hydrogen concentration and, thus, the chemical potential, resulting in a flux of hydrogen toward it.

The elevated hydrogen content lowers the resistive force (F_m) between the atoms. The crack will propagate when the resistive force reaches a value causing the local maximum tensile stress normal to the plane of the crack (σ_z) to equal the maximum lattice cohesive force, given by the following equation:

$$\sigma_z = nF_m c_H \quad [3]$$

Here n is the number of atoms per unit area of crystallographic plane and c_H is the local concentration of hydrogen⁹.

According to Shivanyuk et al.¹², hydrogen-enhanced decohesion can be detected by measuring changes in elastic constants, atomic force constants (measured as a function of the interaction forces between atoms' nuclei and their displacements from one equilibrium position to another¹⁶), and surface energy. Body centered cubic (BCC) metals of group V periodic table elements experience an increase in phonon frequency, which corresponds to the atomic force constant, with increasing concentration of hydrogen. The change in phonon frequency is seemingly unaffected by the change in volume upon hydrogenation. Hydrogen causes a decrease in elastic constants of face centered cubic (FCC) metals, attributed to expansion of the cubic lattice¹².

The HEDE mechanism is often coupled with a less widespread proposal: the hydrogen adsorption method. Because chemical reactions at grain boundaries behave

similarly to free surfaces in some respect, the local affinity for hydrogen at grain boundaries may lower the free energy, thus promoting fracture^{11,14,17}. The segregation of hydrogen along a developing fracture path can, thus, reduce the cohesive energy, resulting in a reduction in atomic binding.

2.2.2 Hydrogen-Enhanced Localized Plasticity

The main principle behind the HELP mechanism is that increases in hydrogen concentration on a local scale can increase dislocation activity in the immediate vicinity^{11,15,18,19}. As reported by Abraham and Altstetter¹⁰, it has been suggested that absorbed hydrogen at a crack tip will facilitate the injection of dislocations. The increase in local dislocation activity causes local stress concentration, contributing to failure initiation at planar defects where hydrogen is not present¹⁵. A brittle fracture surface facilitated by the HELP mechanism will have evidence of slip, dimples, and tear ridges^{11,19}.

The increase in dislocation activity stems from the affinity of absorbed hydrogen for dislocations and other defects (e.g. precipitates, interstitial impurities, grain boundaries). As earlier mentioned, hydrogen is attracted to areas of local hydrostatic tensile stress, such as those surrounding defects. As two dislocations on the same slip plane having the same Burgers vector approach one another, their stress fields merge and the surrounding hydrogen atmosphere is redistributed. As the hydrogen concentration increases, there is a decrease in shear stress experienced by one dislocation due to the other²⁰. The effect is enhanced with increasing hydrogen contents and is graphically represented in Figure 2 (adapted from Robertson²⁰) with C_o as the hydrogen-to-metal atomic ratio H/M). For edge dislocations separated by three times the Burgers vector, b , an H/M ratio of 0.01 decreases the separation force by 8% and an H/M ratio of 0.1 decreases the separation force by 21%²⁰.

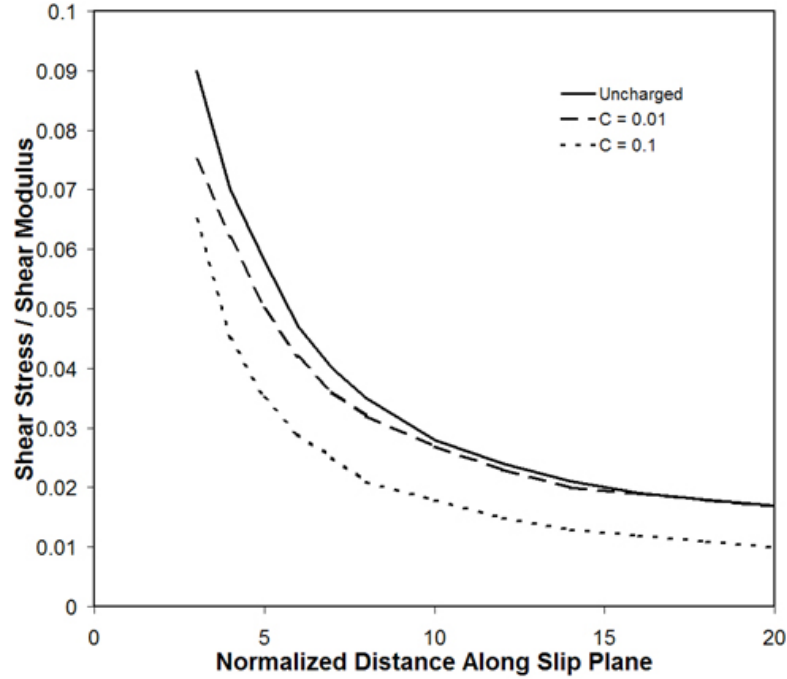


Figure 2: Effect of absorbed hydrogen on the shear stress of dislocation interaction

The hydrogen atmosphere that develops around dislocations and defects create a shielding mechanism that limits interaction with precipitates and forest dislocations, thus easing dislocation glide and enhancing plasticity. In essence, the repulsive interaction energy with the obstacles is decreased, allowing dislocations to move at lower levels of applied stress. The effect is confirmed through successive transmission electron microscope (TEM) images taken inside an environmental cell²⁰. Immediately after straining, the dislocations in α -Ti are stationary when in an evacuated chamber. Upon introducing 13.3 kPa hydrogen gas and without applying further stress, it is seen that new dislocations are formed and existing dislocations become quite mobile. An increase in hydrogen pressure tended to increase the velocity of dislocations. Figure 3 shows the variation in dislocation velocity as dependent on hydrogen gas pressure (adapted from Robertson²⁰).

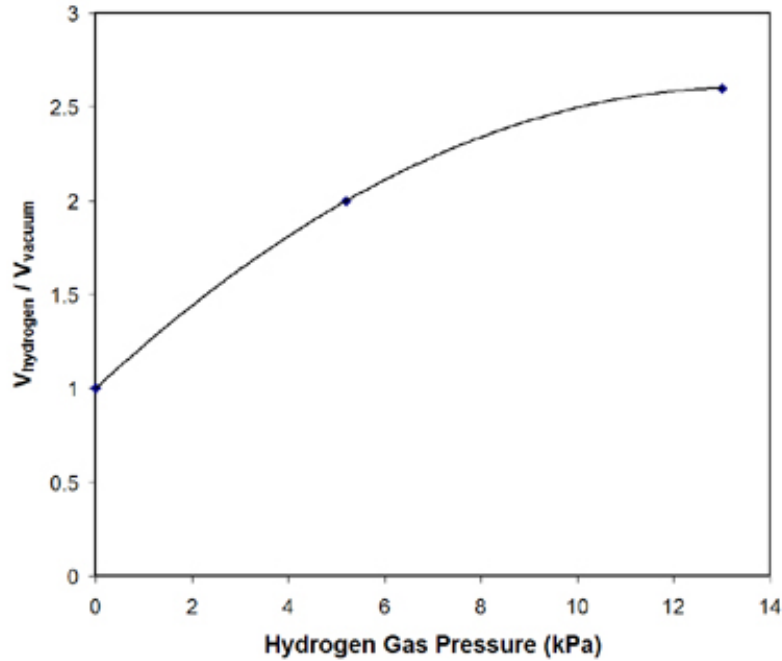


Figure 3: Variation in normalized dislocation velocity with hydrogen gas pressure

It should be noted that the thin foils (< 200 nm) necessary for TEM inspection obey plane stress conditions, but a considerable amount of similar evidence is available from tests on thick samples. Past TEM tests on Fe, Ni, Si-S alloy, Al, Al-alloys, Ni₃Al, Ti, Ti alloys, 316 stainless steel, IN-903, FeAl, and Fe₃Al show identical effects of hydrogen on the mobility of dislocations^{20,21}. This indicates that the mechanism is independent of crystal structure and is the same for edge, screw, mixed, and partial dislocations.

2.2.3 Hydride-Induced Embrittlement (HIE)

The formation of brittle hydrides both in the grain matrix and at the grain boundaries can be detrimental to the mechanical properties of the metal. The process consists of the diffusion of hydrogen, precipitation of hydrides, heat flow, and material deformation¹⁰. With the same driving force for hydrogen diffusion as previously mentioned, a flux of hydrogen is created toward stress concentrators. Once the particular terminal solid solubility (C_{TS}) of hydrogen is reached, a hydride will precipitate^{8,10,22}.

The terminal solid solubility is dependant also on temperature and applied stress^{8,10}. As derived by Varias and Massih²³, the terminal solid solubility for a system is:

$$C_{TS} = C_{TS,0} \exp\left(\frac{w_{acc} + w_{int}}{\gamma RT}\right) \exp\left[\frac{V_H}{RT} \left(\frac{\sigma_{mn}}{3} - \frac{1}{2} M_{ijkl} \sigma_{ij} \sigma_{kl}\right)\right] \quad [4]$$

where $C_{TS,0}$ is the terminal solid solubility in absence of applied stress, w_{acc} is the material strain energy per mole of hydride in absence of applied stress, w_{int} is the interaction energy per mole of hydride while under applied stress, γ is the number of hydrogen atoms in the metal hydride molecule, R is the ideal gas constant, T is the temperature, V_H is the partial molal volume of hydrogen, M_{ijkl} is the elastic compliance tensor, and σ_{ij} and σ_{kl} are the applied stress tensors .

Crack propagation is assisted through the repeated formation and cleavage of hydrides in the stress zone at the crack tip¹⁰. A hydride nucleates in an area reaching terminal solid solubility, and creates an additional stress concentration at its tip. The stress field between the hydride and crack tips facilitates the growth of the precipitate toward the crack²⁴.

2.3 Effect of Strain Rate on Hydrogen Embrittlement

All the embrittlement mechanisms discussed above require the presence of sufficient levels of hydrogen at specific locations. Thus, the embrittlement is limited by the capacity of the hydrogen atoms to move through the metallic lattice by interstitial diffusion. As assisted by dislocation transport, diffusion of hydrogen can be accelerated.

Völkl and Wipf²⁵ have summarized a number of studies on diffusion of H in Fe. Diffusivity values range from 10^{-7} to 10^{-11} m²/s at room temperature. For fracture processes critically dependent on hydrogen diffusion, an increase in the loading rate signifies less time for hydrogen diffusion and thus less embrittlement.

Toribio²⁶ has examined the embrittlement process in steels at different strain rates. He observed that the deleterious effect of hydrogen generally decreased with increasing displacement rate. This is illustrated in Figure 4 (adapted from Toribio²⁶) as the ratio of

the fracture load in presence of hydrogen (F_c) and that in air (F_o) as a function of displacement rate for steels.

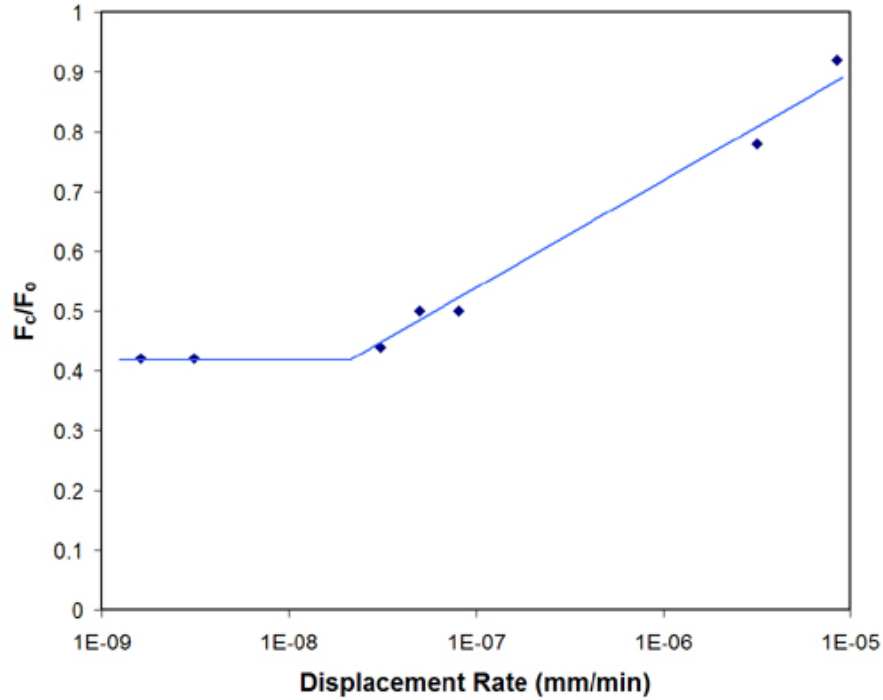


Figure 4: Ratio of fracture load in hydrogen to air versus displacement rate

However, below a critical displacement rate, the diffusion of hydrogen was no longer the limiting parameter, and the hydrogen embrittlement was independent of the displacement rate. The effective hydrogen transport may be aided by dislocation motion. However, such an effect is dependent on many factors including the dislocation density and the presence of oxide and nitride inclusions. Both a high dislocation density and inclusions would deter dislocation motion and thus lower the hydrogen transport. Moreover, it is extremely difficult to determine the effective transport velocity of the hydrogen due to dislocation motion.

2.4 Hydrogen's Effect on Austenite Stability

To date, extensive research and experimentation has been completed on the effect of hydrogen on phase transformation in austenitic stainless steels^{17,27-32}. At room

temperature, SS 316 has a fully austenitic FCC structure, but is metastable. Hydrogen is said to lower the driving force required for a phase transformation even further. Although the literature review focuses on austenitic stainless steels, a more direct link to SS 316 will be made.

It has been observed that γ -austenite can be transformed into either hexagonal close packed (HCP) ϵ -martensite or BCC α' -martensite under various conditions, and effects are often enhanced in the presence of hydrogen. In this report, the transformation from austenite to martensite will first be presented, including an overview of the influence of temperature, stress, and chemistry. The effects of hydrogen and the current models to predict austenite stability will be discussed and each will be critically evaluated and the results of a comparison will suggest the most logical direction for future research.

2.4.1 The Martensite Phase Transformation

A martensitic phase transformation is classified as being diffusionless and involving coordinated shear³³⁻³⁵. It is usually associated with very large distortions due to the accompanying volume change. A transformation from FCC to HCP involves an increase in volume of approximately 1.5-3.5%²⁷. The dilation experienced induces slip or twinning in the austenite matrix. The martensitic transformation has been proposed to evolve in any of the following sequences:

$$\begin{array}{ll} \gamma \rightarrow \epsilon & \text{FCC to HCP} \\ \gamma \rightarrow \epsilon \rightarrow \alpha' & \text{FCC to HCP to BCC} \\ \gamma \rightarrow \alpha' & \text{FCC to BCC} \end{array}$$

The path of martensite formation is said to depend on the stacking fault energy (SFE). The SFE is a material property that dictates a material's propensity to form planar dislocation structures³⁵. As a Shockley partial dislocation, possibly originating from a pole mechanism³⁶⁻³⁸, is passed through the $\{111\}$ plane of the FCC lattice, the regular stacking sequence of ABCABC is altered to ABABC. The ABAB stacking sequence is the HCP structure of ϵ -martensite, so a single stacking fault will nucleate an ϵ -martensite

layer two atoms in thickness. The passage of successive Shockley partial dislocations (Burgers vector of $a/6 \langle 112 \rangle$) across every other $\{111\}$ plane will control the martensite growth^{29,36-38,40}.

Intersecting bands of ϵ -martensite have been noticed to host nucleation sites of α' -martensite^{13,33,36,40-42}. The α' phase forms when a fault on the $\{111\}$ plane is traversed by a second with a Burgers vector of $a/6$ in the $\langle 2\bar{1}1 \rangle$ direction. The volume at the intersection is BCC, forming a lath or needle of α' -martensite in the $\langle 110 \rangle$ direction^{33,36}. At the conjunction, the α' -martensite is only a few nanometers in diameter and is surrounded by the HCP ϵ -martensite, rather than the FCC γ -austenite matrix^{33,40}.

The SFE is dependant on both alloy composition and temperature^{36,38}. For instance, in the range of 95 to 335 K, the SFE can increase from 7 to 32 mJ/m². This effect is shown in Figure 5 (adapted from Spencer³⁶). Alternatively, increasing the nickel or carbon content also results in elevated SFE, changing deformation mode at room temperature from slip to mechanical twinning, inhibiting formation of ϵ -martensite.

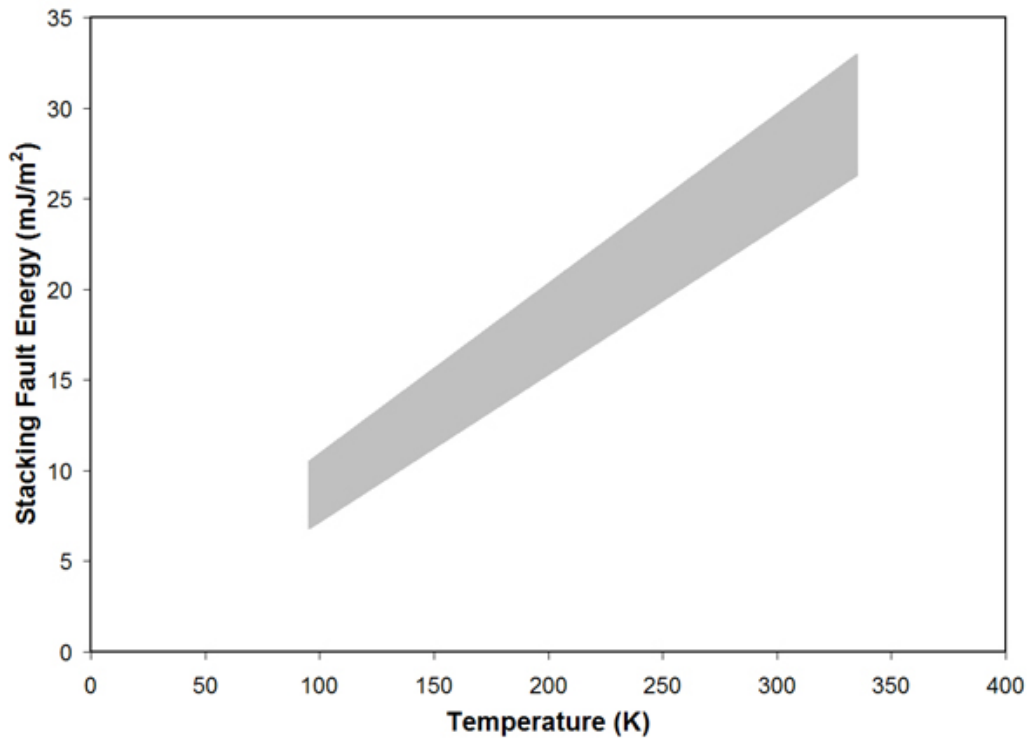


Figure 5: Variation of SFE of SS 304 with temperature change

2.4.2 Phase Transformation from Hydrogen Charging

Phase transformation can occur spontaneously upon charging a sample with hydrogen^{27-29,32,34,43}. This is more frequently seen when performing cathodic charging (as opposed to loading via diffusion during gaseous hydrogen exposure) because relatively large surface concentrations of hydrogen can be obtained. By supersaturating the surface with hydrogen, a large compressive stress is developed over a thin surface layer^{32,34}. Combined with the effect of the small lattice diffusivity of austenite, the result is a large concentration gradient through the thickness^{27,29,32}. Derived from Fick's second law, an expression is developed for the concentration of hydrogen (c_H) through the thickness of the sample:

$$c_H = c_s \operatorname{erfc} \left(\frac{x}{2\sqrt{D_H t}} \right) \quad [5]$$

where c_s is the concentration of hydrogen at the surface, x is the depth into the sample, D_H is the diffusivity coefficient, and t is the duration of exposure. According to Hwang, Chiu, and Johnson, the "solubility is given by the ratio of permeability to diffusivity"⁴⁴. By applying Sievert's law to the equilibrium of hydrogen at the surface, the solubility is shown to be dependent on the square root of hydrogen gas pressure. The surface concentration can then be expressed as:

$$c_s = \frac{P_H}{D_H} \sqrt{P} \quad [6]$$

where P is hydrogen pressure and P_H is the permeability of hydrogen through SS 316.

Yang and Luo report a transformation from 100% γ -austenite to a combined 70% of ε -martensite and α' -martensite after a 16 hour charging period (measured using XRD, confirmed with optical microscopy)²⁷. From tests performed on SS 304 samples, it was determined that a current density of 0.2 mA/cm² is for the formation of martensite. Below this threshold current density, the hydrogen concentrations reached are not sufficient to lower the chemical free energy of the system.

Using Rietveld x-ray diffraction (XRD) analysis, Sugiyama et al. report a decrease in γ -austenite coinciding with an increase in both ε -martensite and α' -martensite³¹. Similar XRD techniques have shown a noted increase in lattice parameter of the γ -austenite phase of stainless steel 310 with continued hydrogenation⁴. The expansion of the austenite lattice upon hydrogenation can result in high multiaxial compressive stresses at the surface and tension beneath^{30,31}. As ample experimentation has shown^{9,29,33,41,45-47}, the transformation from austenite to martensite can be strain-induced or stress-assisted. With the volume change experienced, both the lattice strain and the internal stress state (in addition to the lack of constraint at the surface) lowers the free energy for martensite formation, thus facilitating transformation³⁰.

During room temperature ageing of hydrogen charged specimens, hydrogen is permitted to diffuse out of the crystal lattice. Just as before, the surface concentration changes more rapidly than the bulk material (due to small diffusivity coefficient), creating a severe gradient. In the outgassing process, hydrogen leaves the ε -martensite near the surface, decreasing the lattice parameter of cubic cell and again changing the internal stress state of the material^{27,30,31}. The high tensile stresses formed are said to assist the transformation of ε -martensite to both γ -austenite and α' -martensite^{27,30,31,34}.

2.4.3 Change in M_s and M_d Temperatures

Another way in which hydrogen effects the stability of the austenite phase is by raising the maximum temperature at which thermal martensite will form (M_s) and the highest temperature for martensite induced by plastic deformation (M_d)^{27-30,34}. With a significant enough increase in M_s , martensite can become the stable phase at room temperature. Between the M_s and M_d is the M_s^σ temperature. Up to the M_s^σ temperature, an applied stress below the elastic limit may supplement sufficient energy for a transformation to occur^{36,40,42}. The apparent “yielding” occurs due to the phase transformation. The effect is deemed “stress-assisted” nucleation. Above M_s^σ , elastic stress still contributes chemical driving force, but not enough to supplement a spontaneous transformation. Even stress up to the elastic limit will be insufficient to induce transformation; therefore, yielding occurs due to the regular slip processes. In this

case, the product is strain-induced martensite. Whether the martensite is stress-assisted or strain-induced, they are nucleated at the same sites³⁶. The general trend governing the three temperatures of interest can be seen in Figure 6 (adapted from Spencer³⁶).

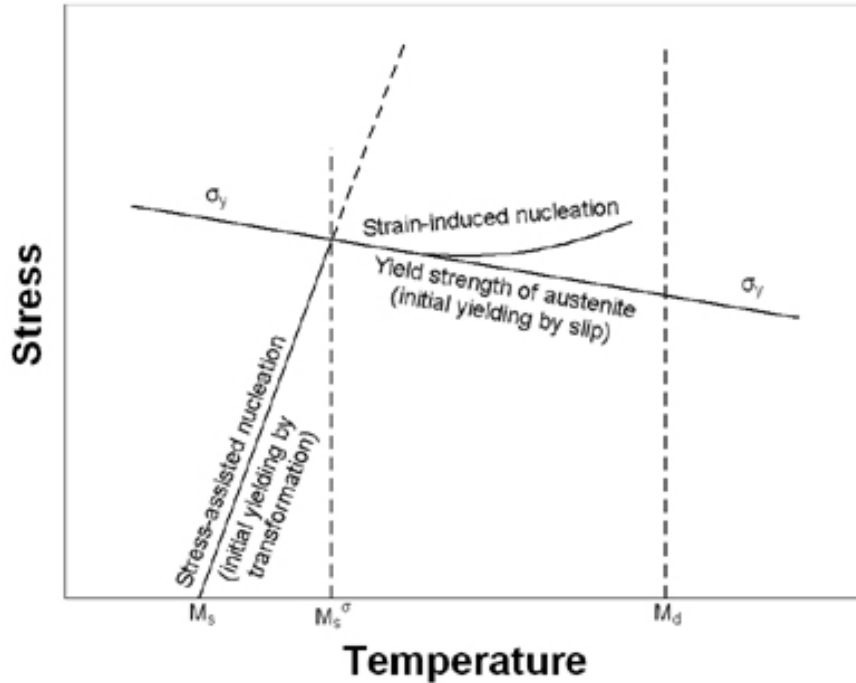


Figure 6: Martensite transformation regimes

As noted by Narita, Altstetter, and Birnbaum²⁹, in samples uniformly charged with hydrogen, γ -austenite was transformed to ϵ -martensite. In the same series of tests, it was also observed that a stainless steel 310 (a normally stable austenitic stainless steel) would not maintain its austenitic structure under deformation in a hydrogen environment. Normally having values much less than 300 K, the M_s and M_d temperatures are shown by the results to increase, causing ϵ -martensite to be stable at room temperature. Because, the motion of partial dislocations on the $\{111\}$ planes leave behind arrays of stacking faults, it has been proposed that dissolved hydrogen changes in M_s and M_d by decreasing the SFE^{29,30}.

2.4.4 Decrease in Stacking Fault Energy

The SFE of an alloy has a significant influence on its properties because of its dependence on temperature and composition³⁸. Properties such as strength, toughness, and fracture are dictated by the prominent role of the SFE in slip mode, deformation twinning, and phase transformation⁴⁸.

Resulting from the relationship between material characteristics and SFE, numerous attempts have been made at modelling changes in stacking fault energy. A thermodynamically based approach was employed by authors of several papers^{38,48-50}. Since stacking faults are nucleation sites for the martensite transformation, they supposed that the SFE will equal the Gibbs energy required to create a platelet of ϵ -martensite two atomic layers thick. As an alternate model, other researchers claim that the decrease in SFE is due to the recombination of hydrogen atoms occupying neighboring interstitial lattice sites^{17,29,32}. It is believed that the binding energy released during the formation of a hydrogen pair is equal to the decrease in SFE. While both models are supported by reasonable conclusions from particular test results, neither is completely accepted by the community of embrittlement researchers.

Several different testing methods have been employed to show a decrease in SFE due to the presence of solute hydrogen^{17,27}. Because each stacking fault is, in essence, a nucleation of HCP ϵ -martensite, a shift in the energy required to form the fault will unavoidably change the metal's inclination to phase transformation. As reported by Hermida and Roviglione, an unstable austenitic stainless steel 304 showed a 37% decrease in SFE in the presence of 274 ppm hydrogen at room temperature¹⁷. As studied by Pontini and Hermida, there occurs a significant drop in SFE of 304 austenitic stainless steel cathodically charged with hydrogen³².

Using XRD and a transmission electron microscope, the SFE was quantified and related to hydrogen content prior to martensite transformation. A plausible cause for the phenomenon is from the electronic effect of the formation of hydrogen pairs¹⁷. Further Rietveld analysis has been performed to confirm the presence of hydrogen in octahedral sites in 304 and 310 austenitic steels³⁰. From calculations of binding energy for H-H pair formation in a faulted zone, it has been suggested that the pair formation is most likely to occur along directions connecting octahedral interstices of HCP stacking sequences

(normal to $\{111\}$ planes). Slip on the $\{111\}$ plane causes hydrogen in the octahedral interstices of austenite to become close to those of HCP martensite¹⁷. Thus, in order to predict the formation of martensite, a model must be developed to estimate changes in stacking fault energy.

2.5 Martensite's Role in Hydrogen Embrittlement

Although the formation of martensite in austenitic stainless steels is believed to be a route to hydrogen embrittlement, research and experimentation has yet to confirm its role in the process. Some hypotheses claim that martensite formation is the sole contributor to the embrittlement, some testify it is a partial contributor, and some say it plays no role at all^{2,8,9,12-15}. All agree that martensite is often present at the fracture surface, but to date, very little work has been done to verify martensite's role, or lack thereof, in hydrogen assisted fracture.

2.5.1 Opposing Arguments

The main argument against martensite's role in hydrogen embrittlement is that the original theory was based on the embrittled fracture surface coinciding with the (111) habit plane of BCC martensite¹²⁻¹⁵. Some researchers state that this is a coincidence rather than the cause because the role of ϵ -martensite has yet to be proven¹². As reported by Shivanyuk, Foct, and Gavriljuk¹², (111) is also a slip plane of the FCC crystal structure, which is an important factor when considering the FCC γ -austenite matrix. The same paper also mentioned that high nitrogen austenitic stainless steels also experience slip band cleavage-like cracking along (111) without the presence of any second phase.

Han, He, Fukuyama, and Yokogawa¹³ present tensile test results from both hydrogen environment and cathodic charging of a range of austenitic stainless steels. It was shown that although the stable grade 310 was embrittled by severe cathodic hydrogen charging, it remained unaffected by a gaseous hydrogen environment. Unstable and metastable grades 304 and 316, however, displayed signs of embrittlement in all cases. It was then proposed that strain-induced martensite is not responsible for the

embrittlement of the stable grade of austenitic stainless steel because it was not formed¹³. The embrittlement was claimed to be due to its low stacking fault energy.

Tensile tests performed by Han et al.¹³ show the effect of hydrogen on the properties of SS 304. Tests were performed at 80, 220, and 295 K in both helium and hydrogen atmospheres to produce varying amounts of strain-induced martensite. As indicated by the slope of the stress-strain curve, hydrogen was not shown to enhance the formation of martensite as both the hydrogen and helium curves share the same work hardening rates. With decreasing temperature, a higher degree of martensite was formed. The point of interest here is that hydrogen seemed to cause premature failure in the samples forming the least amount of martensite.

Another concept investigates the cause of embrittlement using silicon as an alloying element to compare altered properties of austenitic stainless steels^{12,15}. The intent was to use silicon to decrease the stacking fault energy of the γ -austenite phase, thus promoting the formation of ϵ -martensite. Comparing XRD patterns of a Cr25Ni20 to a Cr25Ni20Si3 alloy (SS 310) show that more martensite was formed upon charging the alloy containing silicon additions. Due to the additional alloying, the material experienced an increase in ductility, suggesting that ϵ -martensite does not have a deleterious effect on the integrity of the steel. The ϵ -martensite plates are claimed to strengthen the material by acting as obstacles for dislocation slip¹².

2.5.2 Supporting Arguments

Two alternate mechanisms of hydrogen embrittlement were compared by Han et al.¹³: hydrogen embrittlement due to strain-induced martensite versus the presence of carbides. At grain boundaries, chromium carbides precipitate, forming a zone depleted of chromium and carbon. Hydrogen is accumulated and trapped at the precipitate and intergranular fracture results¹³. Strain-induced ϵ - and α' -martensite are also found along the grain boundaries, indicating that they are preferentially formed in chromium and carbon depleted zones. Because both occur simultaneously along grain boundaries, it is difficult to distinguish whether intergranular cracking is the result of one or the other.

A method implemented to determine the rank of the competing factors is to test hydrogen's effect on the total elongation of sensitized versus desensitized and solution annealed tensile samples¹³. Commercially available 304 austenitic stainless steel samples were either solution annealed to produce a 100% γ -austenite microstructure, sensitized to develop chromium carbides at grain boundaries, or desensitized to remove chromium and carbon depleted zones. Tests were conducted at 220 K in order to ensure that martensite would be formed and that hydrogen would expedite the failure. The total elongation to failure was drastically affected by the sensitization when tested in a hydrogen environment, but not as much in helium. The desensitization heat treatment helps to recover much of the lost ductility and changes failure mode from intergranular back to transgranular.

The question is then raised of the difference between strain-induced martensite and martensite formed from hydrogen charging. According to Shivanyuk et al.¹², TEM observations have shown that hydrogen-induced ϵ -martensite is both crystallographically and morphologically identical to strain-induced ϵ -martensite, so, in theory, they should respond similarly. Based on their research, Pan, Chu, Li, Liang, Su, Gao, and Qiao⁸ propose the opposite – the effect of martensite induced by cold work is different than that induced by hydrogen charging. There is not necessarily any difference in crystal structure, but cold rolling may introduce other defects. Their research revealed that cold rolling of type 304 steel at 77 K generated martensite but also increased dislocation density, both factors contributing to the brittleness.

Martensite has been considered to be the root of hydrogen embrittlement due to several observations of microstructure and fractography and from revealing experimental results. Han et al.¹³ noticed that transgranular fracture along α' -martensite laths occurred when tested in a hydrogen atmosphere. The martensite in this case was believed to be strain-induced as the nucleation point is located at intersections of microscopic shear bands consisting of stacking faults and ϵ -martensite which was homogeneously distributed throughout the grains.

A notion common to many researchers of differing opinions is that hydrogen embrittlement is controlled by the transportation and accumulation of hydrogen at or near the crack tip^{9,12-14,51}. Experimentation by Huang and Altstetter⁵¹ showed that a large

concentration of α' distributed throughout the bulk of a specimen facilitated the distribution of hydrogen in the specimen. Because crack propagation is governed by hydrogen penetration of the metal by diffusion, it really becomes a function of temperature, chemical potential, and microstructure^{13,14}. Strain-induced α' -martensite has higher diffusion and permeation coefficients than both ϵ -martensite and γ -austenite, giving it the potential to act as a path for hydrogen transportation to the triaxial stress field ahead of the crack tip^{2,13,52}. This phenomenon was confirmed through measurements of diffusivity and permeability of deformed unstable austenitic stainless steels⁹. In type 301 stainless steel, it was shown that increased deformation caused elevations in diffusivity and permeability. By comparing to test results of a stable austenitic sample (type 310), it was confirmed that the change in properties was a function of martensite content rather than the deformation⁹. Also shown by Perng and Alstetter⁹ was that γ -austenite could dissolve much more hydrogen than α' -martensite. The same increase in deformation (that is, the same increase in α' -martensite content) produced a considerable decrease in hydrogen solubility. Herms, Olive, and Puiggali² and Chêne, Aucouturier, Arnould-Laurent, Tison, and Fidelle⁵² agree that the high solubility of hydrogen in face centered cubic structures, such as austenite, contributes to its resistance to hydrogen embrittlement.

2.5.3 Comparison of Views

Arguments provided by Han et al.¹³ act against the role of strain-induced martensite in stable austenitic stainless steels. It was stated that embrittlement is not due to strain-induced martensite, but rather the low stacking fault energy. Shivanyuk et al.¹² successfully show that lowering the stacking fault energy promotes the transformation from γ -austenite to ϵ -martensite, and they reconfirm the influence of hydrogen on the degradation of ductility. Their tensile test results adequately prove that the performance of a sensitized SS 304 sample is compromised in a hydrogen atmosphere. Sensitization causes a depletion of chromium and carbon at the grain boundaries, which is said to promote the formation of martensite. TEM images prove the presence of both ϵ - and α' -martensite at the grain boundaries in the sensitized samples and their absence in the

desensitized and solution annealed samples. Because the sensitized material contained carbides and martensite at the grain boundaries and the desensitized material had carbides, but no martensite at the grain boundaries, it is assumed that the transition from ductile to brittle is due to the presence of martensite.

Huang and Altstetter⁵¹ claim that martensite formation is not a necessary condition for hydrogen embrittlement, but it will aid in the transport of hydrogen through the metallic lattice. This means that an evenly distributed martensite concentration will help to evenly distribute dissolved hydrogen. On the other hand, if martensite formed locally at the crack tip, a local concentration of hydrogen would be available for accelerated dislocation motion and reduction of granular cohesion.

The arguments presented both for and against martensite's role in hydrogen embrittlement of austenitic stainless steels have solid foundations with legitimate experimental evidence. The evidence supporting the effects of martensite is difficult to deny, but many doubts have surfaced. Although there is insufficient evidence from the literature to prove martensite does not play a role in hydrogen embrittlement, not all grades of austenitic stainless steel have been proven to have contributions from martensite. It is clear that there is a significant difference between phase transformations of stable versus unstable grades, so it is possible that martensite's effect is variable. Martensite can form in stable grades, but the material behaves differently when it does. Therefore, it is of more significant interest to conduct research on a case-to-case basis of each grade before making any final verdict.

3.0 Scope and Objectives

The main function of this thesis is to determine the significance of martensite's role in the hydrogen embrittlement of austenitic stainless steel. In doing so, it is sought to discover hydrogen's contribution to the austenite-to-martensite phase transformation and the importance of stacking fault energy with regards to hydrogen embrittlement resistance. The difference between the effects of only a surface concentration of hydrogen will be contrasted with those of a bulk hydrogen concentration. This will answer the question of immediacy of hydrogen embrittlement. To do so, samples tensile tested in a hydrogen atmosphere without prior exposure will be compared to those tested in air after being fully saturated with hydrogen.

The secondary purpose of the work is to develop innovative testing methods for assessing hydrogen embrittlement of metals. The work was supported by Powertech Labs, Inc., whose interest lies in the development and standardization of testing practices. There are several published standards pertaining to material performance in a hydrogen atmosphere, but not one accurately represents the state of the material in service. Significant deviations from foreseen use of the material can result in the rejection of suitable materials, or, much worse, the acceptance of unsuitable materials. The outcomes are, therefore, of particular interest to Powertech because they will contribute to the evolution of test standards for the hydrogen compatibility of materials as well as contribute to the knowledge of material behavior in high-pressure hydrogen. Coinciding with Powertech's interests, specific attention will be paid to austenitic stainless steels.

To achieve the goals, two alloys will be focused upon: SUS 316 and SUS 316L. Austenitic stainless steel 316 was selected because it is the main material of construction for many high-pressure hydrogen components, tubing, and tank liners. Although it has been safely used in pressurized hydrogen atmospheres for several years, it can still become brittle when deformed to large strains in hydrogen gas. SUS 316L was also tested because it is very similar in properties, but differs slightly in chemistry.

4.0 Experimental Design and Development

In order to achieve the objectives of this thesis, a series of experiments were designed to thoroughly examine the behavior of the material. Since the principal function of this thesis is to develop new experimental techniques, not only will the methodology be discussed, but the supporting rationale will also be presented with attention to how and why the tests were developed. The following section describes the materials tested and a detailed procedure of tests performed, including discussions of calculations supporting the designs, setup, and apparatus involved.

4.1 Materials Tested

Stainless steels SUS 316 and 316L were selected as test materials because they are both used in the high-pressure hydrogen industry and they represent varying degrees of austenite stability. Powertech Labs supplied the materials, as 316 and 316L were the focus of an ongoing study and the work conducted in this thesis was of particular interest. The chemistries of the alloys are listed in Table 1.

Table 1: SUS 316 and 316L chemical compositions

Element	SUS 316	SUS 316L
C	0.027	0.025
Mn	2.00	1.52
Si	0.70	0.48
P	0.05	0.032
S	0.01	0.018
Ni	10.30	12.04
Cr	16.80	16.84
Mo	2.20	2.04
Cu	0.45	-

Pickering reported the following empirical relation between SFE (in mJ/m^2) and content of alloying elements⁵³:

$$\text{SFE} = 25.7 + 2(\% \text{Ni}) + 410(\% \text{C}) - 0.9(\% \text{Cr}) - 77(\% \text{N}) - 13(\% \text{Si}) - 1.2(\% \text{Mn}) \quad [7]$$

Here, it is seen that higher nickel content increases its stacking fault energy, and thus its phase stability. According to equation 7, SUS 316 has a SFE of 30.8 mJ/m^2 and 316L has a SFE of 36.8 mJ/m^2 . Therefore, SUS 316L is meant to demonstrate a higher resistance to phase transformation for a basis of comparison. Conclusions will be drawn on the importance of phase stability with regards to hydrogen embrittlement.

4.2 Hydrogen Environment Tensile Tests

In order to test the effect of hydrogen acting at the surface of the material, cylindrical tensile samples were pulled in uniaxial tension within various pressures of gaseous hydrogen atmospheres. Assuming a local equilibrium of hydrogen will exist directly at the surface, its concentration is not a function of time (it depends only on temperature and pressure). Therefore, by performing tensile tests in a gaseous hydrogen environment, the immediate effect of hydrogen can be established.

The specimens used were sub-sized round-type tensile samples with 25.4 mm gauge lengths. A diagram showing specimen geometry can be seen in Figure 7.

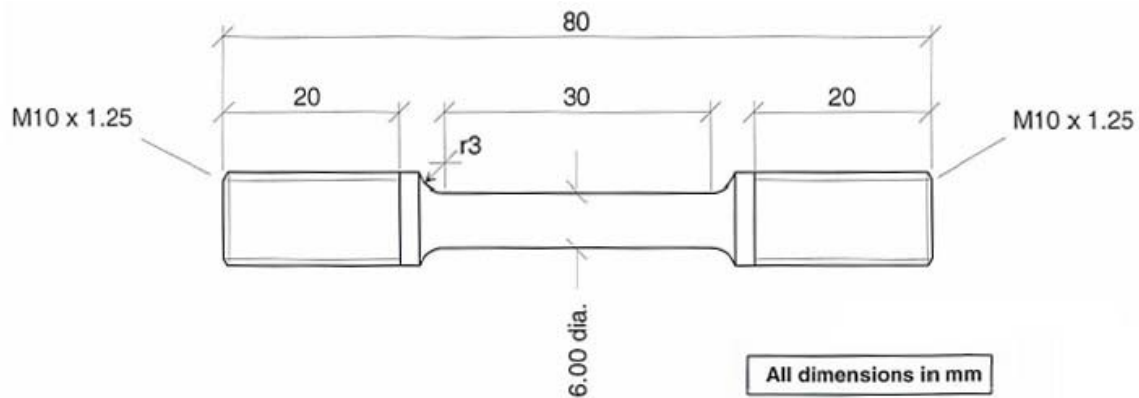


Figure 7: Round tensile specimen geometry

Machining marks were removed from gauge section of the specimen surface by polishing with a fine silicon-carbide paper (600 grit). The surface was then ultrasonically cleaned in acetone to remove any dirt or oil. To account for slight differences in

machining or polishing, the diameter of each specimen was measured in three locations across the gauge length. From the minimum of these measurements (i.e. the expected location of final failure), the initial cross-sectional area was calculated. The initial measurements can be seen in Table 2.

Table 2: Initial geometry measurements

SUS 316			SUS 316L		
Sample	Diameter	Area	Sample	Diameter	Area
T1	5.83 mm	26.7 mm ²	TL1	5.87 mm	27.1 mm ²
T2	5.89 mm	27.2 mm ²	TL2	5.91 mm	27.4 mm ²
T3	5.93 mm	27.6 mm ²	TL3	6.02 mm	28.5 mm ²
T4	5.86 mm	27.0 mm ²	TL4	5.90 mm	27.3 mm ²

The tensile tests compared the behavior of the material in different environments. A comparison was made with respect to gaseous medium and temperature. A summary of the test conditions is located in Table 3. As seen in the table, a slow strain rate was used. The purpose of this was to limit changes in temperature and to provide ample opportunity for the hydrogen molecules to migrate to the sample surface. With a sample gauge length of 25.4 mm, the strain rate corresponds to a crosshead motion of 0.064 mm/min.

Table 3: Tension test parameters

Sample ID	Material	Gaseous Medium	Pressure (MPa)	Temperature (°C)	Strain Rate (1/s)
T1	SUS 316	He	25	20	4.2×10^{-5}
T2	SUS 316	H ₂	25	20	4.2×10^{-5}
T3	SUS 316	He	25	-40	4.2×10^{-5}
T4	SUS 316	H ₂	25	-40	4.2×10^{-5}
TL1	SUS 316L	He	25	20	4.2×10^{-5}
TL2	SUS 316L	H ₂	25	20	4.2×10^{-5}
TL3	SUS 316L	He	25	-40	4.2×10^{-5}
TL4	SUS 316L	H ₂	25	-40	4.2×10^{-5}

Several samples from each material were pulled in uniaxial tension until failure. Tests were performed in 25 MPa gaseous helium and hydrogen at both room temperature and at -40°C. Each gas was supplied as 99.999% pure. To achieve the low temperature conditions, a Sintech 20/G mechanical testing frame was equipped with pull rods that reach through an environment chamber into a pressure vessel to engage with the specimen. Prior to testing, both the chamber and the specimen were conditioned at -40°C for a minimum of 4 hours. The test setup is shown in Figure 8.

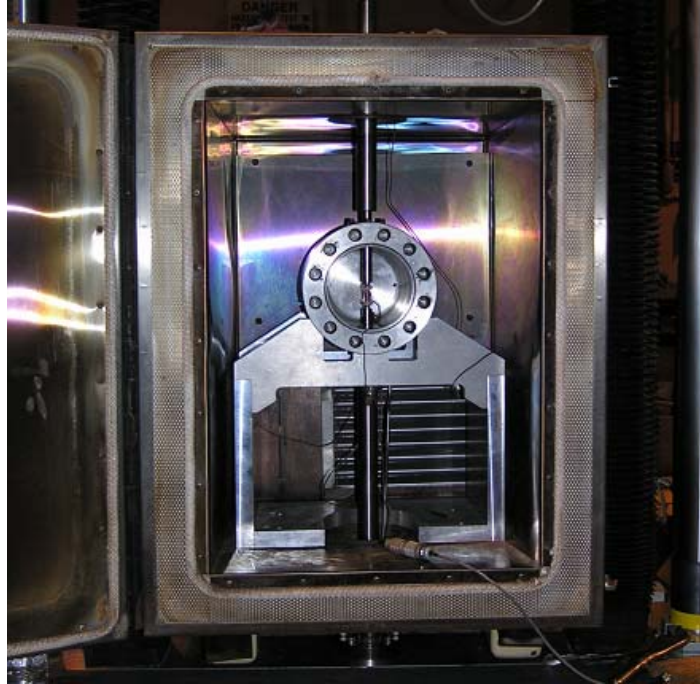


Figure 8: Integration of pressure vessel, environment chamber, and tensile test frame

Once the specimen was affixed to the pull rods, the pressure vessel was sealed and purged three times with nitrogen to eliminate moisture and other contaminants. As the test gas was introduced, the internal pressure acted against the pull rod and pushed it outward. The test frame prevented it from moving, thus imposing a compressive load on the load cell. At this point, the crosshead (and the pull rod) was set in motion at the specified rate. The friction from the seal was noted to be very small (~ 300 N), but also had an effect on the measured load and later subtracted from the data. The specimen was still loose within the chamber, so the residual compressive load was set as the balance, or zero point. During each test, the gas pressure decreased slightly due to a change in internal volume associated with extraction of the pull rod (pressure never dropped more than 2%), so the compressive load was constantly changing. The internal pressure is directly proportional to the volume of the chamber, so a linear offset line was included to account for the effect of pressure degradation on the measured load. Figure 9 provides an example of the measured load, the zero line, and the final zeroed load.

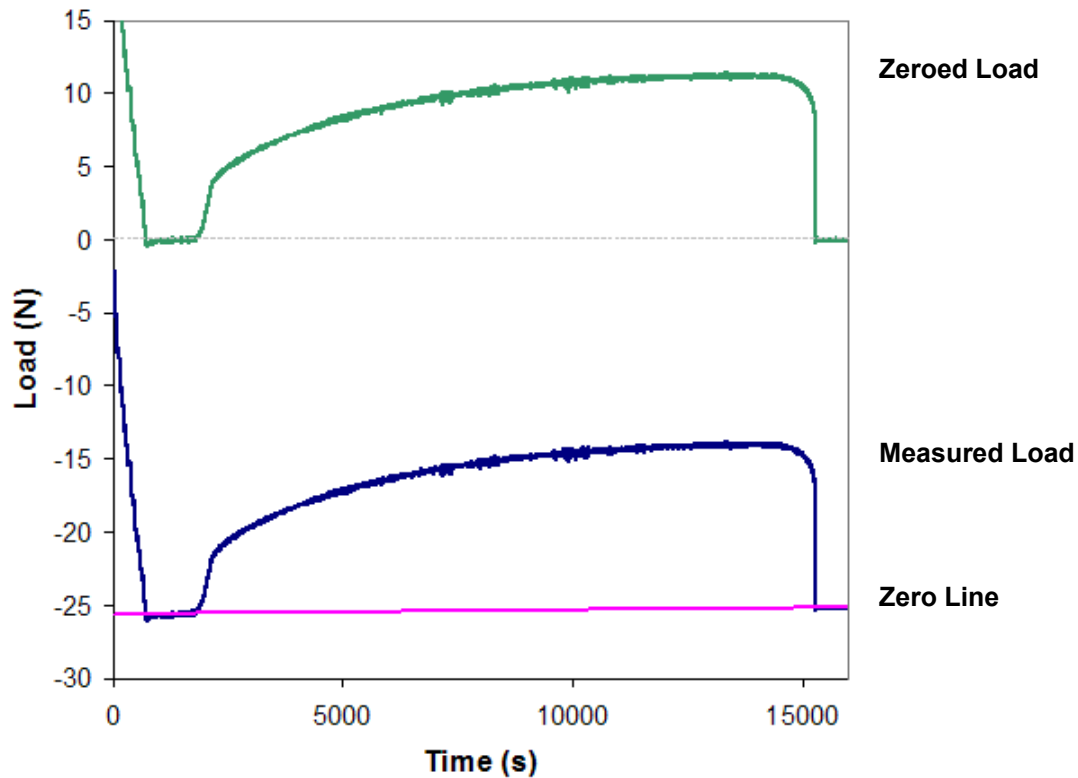


Figure 9: Setting balance point for load cell reading

Each specimen was pulled at the specified strain rate until failure. The yield strength was determined using the offset method described in ASTM test standard E8⁵⁴. A line of equal slope to the elastic portion of the stress-strain curve is drawn with an offset of 0.2% strain. The point at which this line intersects the stress-strain curve represents the yield stress occurring at a plastic strain of 0.2%. The reported ultimate tensile strength is simply determined by the maximum stress reached. The full stress strain curve was calculated from the crosshead displacement, and the compliance of the equipment. The magnetic balance method (see section 4.4.2) was used to quantify the α' -martensite content, and then the fracture surfaces were viewed with a scanning electron microscope (SEM) to determine the failure mechanisms.

Following the test, the specimens were measured for total elongation and reduction of cross-sectional area. Two gauge sections 25.4 mm long were marked with a fine-tipped pen on the reduced section of each specimen prior to testing. The fractured specimens were re-assembled and the gauge marks were re-measured after final fracture

to calculate the percent elongation. The diameter of the specimens at the point of fracture was measured and used to calculate the total reduction of cross-sectional surface area.

An extensometer capable of reaching the full elongation-to-failure could not be accommodated within the pressure vessel, so complete stress-strain curves were interpreted from the crosshead displacement. The crosshead displacement includes a combination of strain in the machine, the grip fixtures, and the grip and gauge sections of the specimen. To differentiate between strain in the specimen gauge and the test equipment, it is reasonable to assume that all deformation in the machine will remain elastic (i.e. the relationship between the applied load and the amount of deflection will remain linear and reversible). Spring constant equations were applied to the system as follows:

$$k_{eff} = \left(\frac{1}{k_m} + \frac{1}{k_g} \right)^{-1} \quad [8]$$

where k_m is the spring constant of the machine, k_g is the spring constant for the gauge section of the sample, and k_{eff} is the effective spring constant for the entire system. The value of k_{eff} is calculated from the slope of the linear elastic portion in the load versus crosshead displacement curve and k_g is calculated from the slope of the linear elastic portion in the load versus extensometer displacement curve. Equation 8 was then used to calculate k_m . The deflection of the machine, ΔL_m , for a given load, P , is governed by:

$$\Delta L_m = \frac{P}{k_m} \quad [9]$$

This deflection can be subtracted from the crosshead displacement to provide a theoretically derived gauge section displacement, which is then converted to a strain value. Figure 10 shows a sample comparison between the strain measured from the strain gauge and the strain calculated from crosshead displacement.

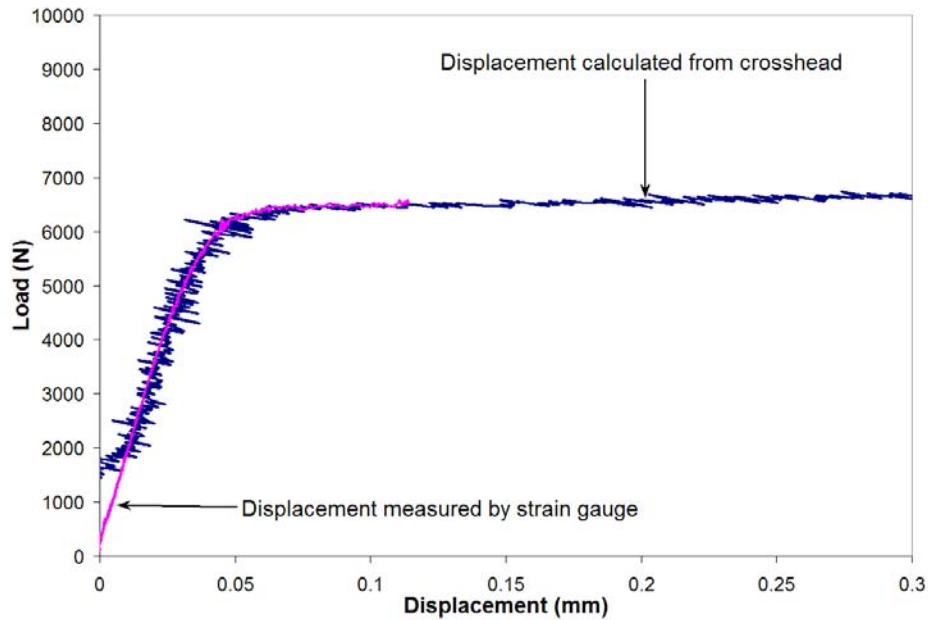


Figure 10: Measured versus calculated strains

4.3 Bulk Material Hydrogen Effects

To determine how absorbed hydrogen affects the bulk of the material, it was desired to test samples uniformly charged with hydrogen. A series of permeation tests were conducted to determine how much hydrogen exposure would result in a fully saturated sample. Specimens could then be tested in different conditions to determine the effect of hydrogen.

4.3.1 Permeation Tests

In order to resolve the effect of solute hydrogen on bulk material properties, tensile tests were performed on samples charged with hydrogen. Because a concentration gradient will affect both the stability of the austenite phase and the internal stress, an even distribution of absorbed hydrogen was sought. Although a higher concentration of solute hydrogen can be obtained from electrolytic charge techniques, large concentration gradients are often associated. In order to achieve the appropriate hydrogen distribution, specimens were gaseously charged at elevated temperature.

To ensure that hydrogen will sufficiently penetrate and diffuse through the test material, a series of permeation tests were designed and performed. A schematic of the test setup developed as part of this thesis is shown in Figure 11. As can be seen, a hydrogen gas supply pressure is regulated and delivered to the disk permeation jig contained within the convection oven.

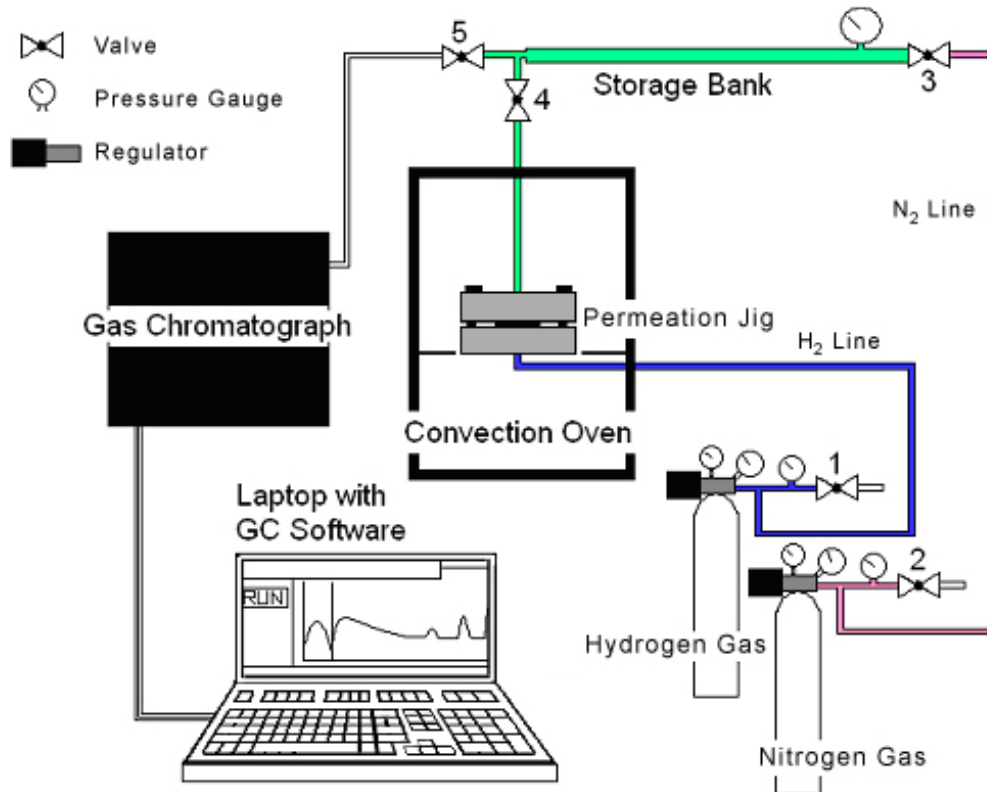


Figure 11: Permeation test setup schematic

With valves 3 and 5 closed, hydrogen was allowed to permeate the material, mixing with the nitrogen in the storage bank. Pressure gauges were used to monitor pressure on either side of the disk to help detect and prevent leaks. After the prescribed amount of time, valve 4 was closed and valve 5 was opened. The positive pressure pushed a sample of the gas to the gas chromatograph (GC) to be analyzed for presence of hydrogen. As shown in Figure 12, the thin disk is sandwiched between a flanged jig having an inlet port on one side and an outlet port on the other. The flanges compress the

sample between an o-ring on the inlet side and a high strength ring on the outlet side. The tests were performed repeatedly at several different temperatures.

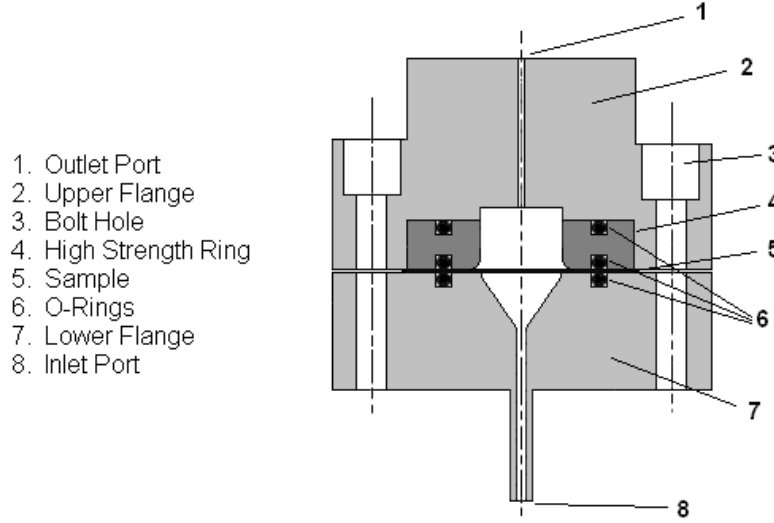


Figure 12: Permeation sample jig

In order to determine the hydrogen permeation properties of the material, the test was started after reaching steady state. Time to reach steady state was estimated based on equations derived from Fick's Laws of diffusion. Assuming that the initial concentration of hydrogen is zero and the concentration on the outlet side of the disk is zero, the following equation describes the diffusion behavior with a constant hydrogen supply⁵⁵:

$$\frac{Q}{LC} = \frac{D_H t}{L^2} - \frac{1}{6} - \frac{2}{\pi} \sum_{n=1}^{\infty} \frac{(-1)^n}{n^2} \exp \left[-D_H t \left(\frac{\pi n}{L} \right)^2 \right] \quad [10]$$

Here, Q is the amount of solute hydrogen penetrating the disk per unit area at a given time, L is the sample thickness, C is the concentration of hydrogen supplied to the surface, D_H is the diffusivity of hydrogen through the material, and t is the amount of time given for permeation. By experimenting with a simple computer program written to perform the iterations, it was determined that values of n beyond 50,000 were negligible to the results. Plotting Q/LC as a function of $D_H t/L^2$ shows that steady state is reached

when the graph approaches linearity (i.e. at long times). It was decided that the system will sufficiently reach steady state at $D_H t/L^2 = 0.4$ (shown in Figure 13 as adapted from Wilkinson⁵⁵).

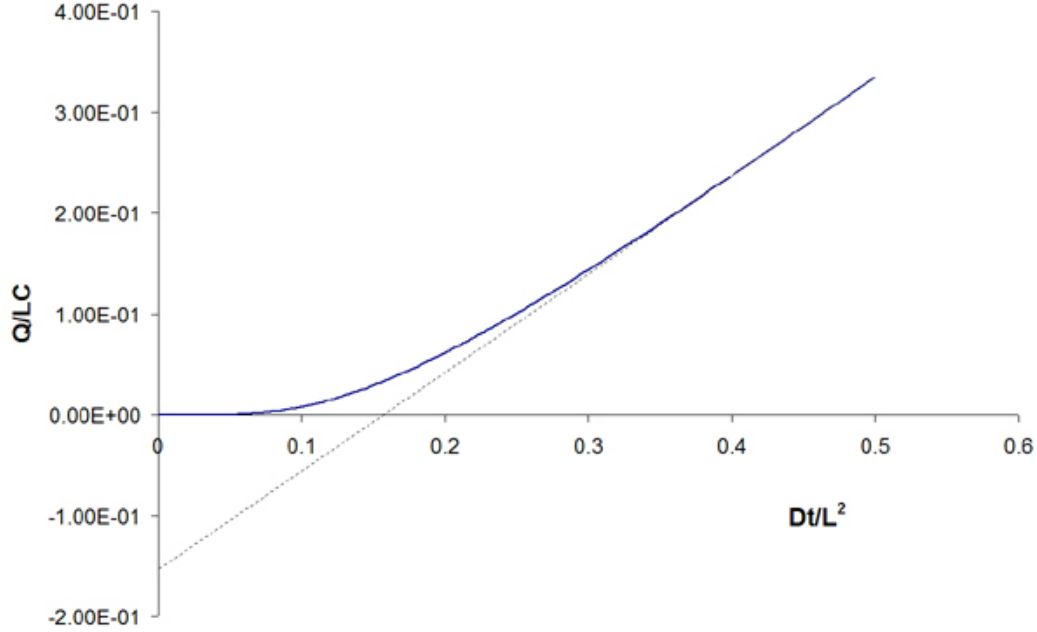


Figure 13: Diffusion of hydrogen through thin disk sample

The time to reach steady state can then be calculated from the thickness of the specimen and the diffusivity. The diffusivity of the material is a function of temperature given by the following Arrhenius relation:

$$D_H = D_o \exp\left(\frac{-E_d}{RT}\right) \quad [11]$$

where E_d is the activation energy for diffusion. From Oriani et al.⁵⁶, the value of D_o for stainless steel 316 is $1.74 \times 10^{-6} \text{ m}^2/\text{s}$ and E_d is $5.28 \times 10^4 \text{ J/mol}$. Figure 14 shows the time to reach steady state in the temperature range of 433 to 513 K. To reach steady state diffusion in a reasonable amount of time, tests were conducted at 453, 473, and 493 K. According to the graph in Figure 14, times to reach steady state are 78, 43, and 25 hours, respectively.

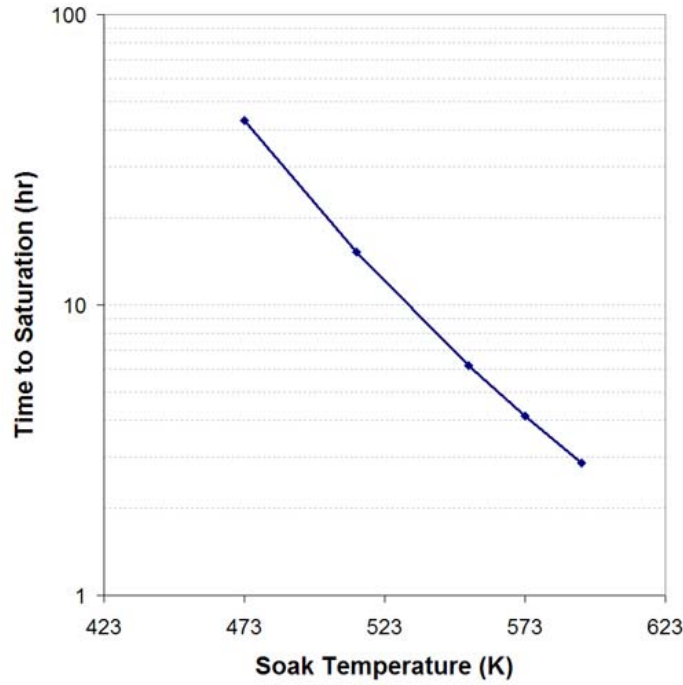


Figure 14: Time to reach steady state hydrogen diffusion for SS 316

As reported by San Marchi⁵⁷, the permeability of hydrogen through is relatively independent of composition and microstructure in most austenitic stainless steels. Due to their similarities in mechanical properties and chemistry, it was assumed that SS 316 and 316L would also have similar permeation properties. Therefore, tests were only performed on samples of SS 316L. The following equation describes the pressure required to yield a membrane of thickness L and radius R made from a material with yield strength σ_{ys} ⁵⁸.

$$P_{\max} = \frac{8}{3} \left(\frac{L^2 \sigma_{ys}}{(1 + \nu) R^2} \right) + P_N \quad [12]$$

Here P_{\max} is the maximum pressure before yielding the material and P_N is the pressure of the nitrogen sample gas. As shown in Figure 15 (adapted from research by UGINE & ALZ⁵⁹), a decrease in yield strength can be correlated with an increase of temperature, which also must be considered.

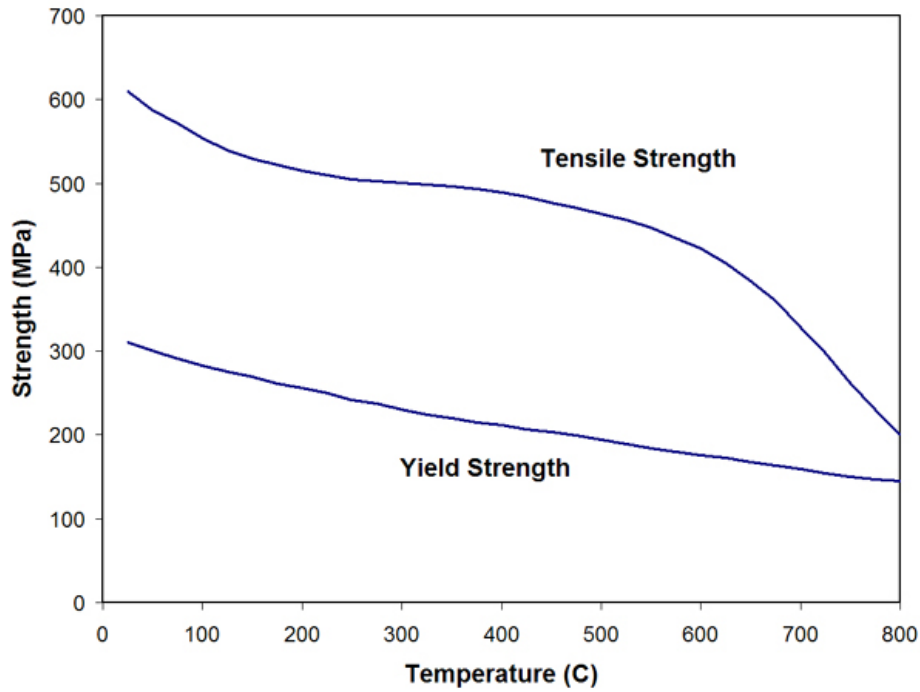


Figure 15: Strength of SS 316L as a function of temperature

A nitrogen supply regulated to 0.1 psi was used to purge and fill the storage bank of the permeated gas. Incorporating the parameters listed in Table 4 into equation 12, it was determined that the permeation test specimen could be safely pressurized to 1.8 MPa without yielding the material.

Table 4: Parameters used in calculation of maximum permeation pressure

L	R	ν	σ_{ys}	P_N
0.9 mm	12.5 mm	0.3	250 MPa	0.1 MPa

4.3.2 Tensile Tests

The supplied material was rolled at room temperature to a thickness of 0.5 mm. Using wire electrical discharge machining (EDM), the thin strips were machined to the sub-sized tensile specimen dimensions shown in Figure 2. They then underwent a thirty minute anneal at 1050°C argon atmosphere to re-crystallize and restore their fully austenitic structure. Optical metallography was used to confirm the microstructure.

Although the anneal was conducted in an inert environment, the surface was polished with 600 grit sand paper to remove any oxide that had formed.

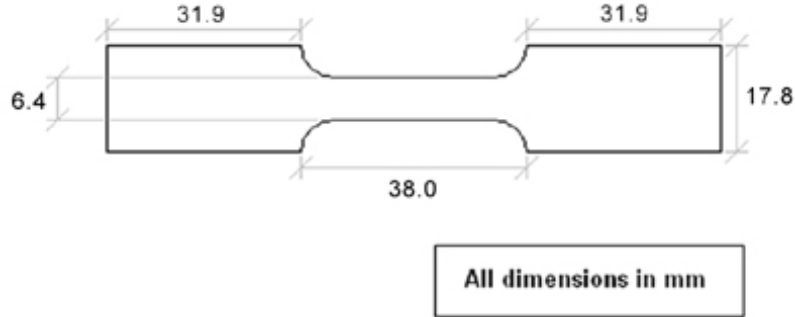


Figure 16: Dimensions of thin tensile specimens

After establishing the permeation characteristics of austenitic stainless steel 316, it was necessary to determine the duration of gaseous hydrogen soak required to reach complete saturation. To do so, a model was used to predict the concentration profile of a material of finite thickness with set concentration of hydrogen on either side. Based on a Fick's law solution for long periods of time, the following formula was reported by Wilkinson⁵⁵:

$$c_H = c_s \left[1 - \frac{4}{\pi} \sum_{n=1}^{\infty} \left(\frac{(-1)^n}{2n+1} \exp \left(\frac{-D_H (2n+1)^2 \pi^2 t}{4L^2} \right) \cos \left(\frac{(2n+1)\pi x}{2L} \right) \right) \right] \quad [13]$$

Here, L is half the sample thickness. As with equation 10, only 50 000 iterations were necessary in calculations of hydrogen concentration profiles. Based on a sample 0.5 mm thick, profiles were calculated for a pressure of 70 MPa at 373 K for varying storage times (Figure 17).

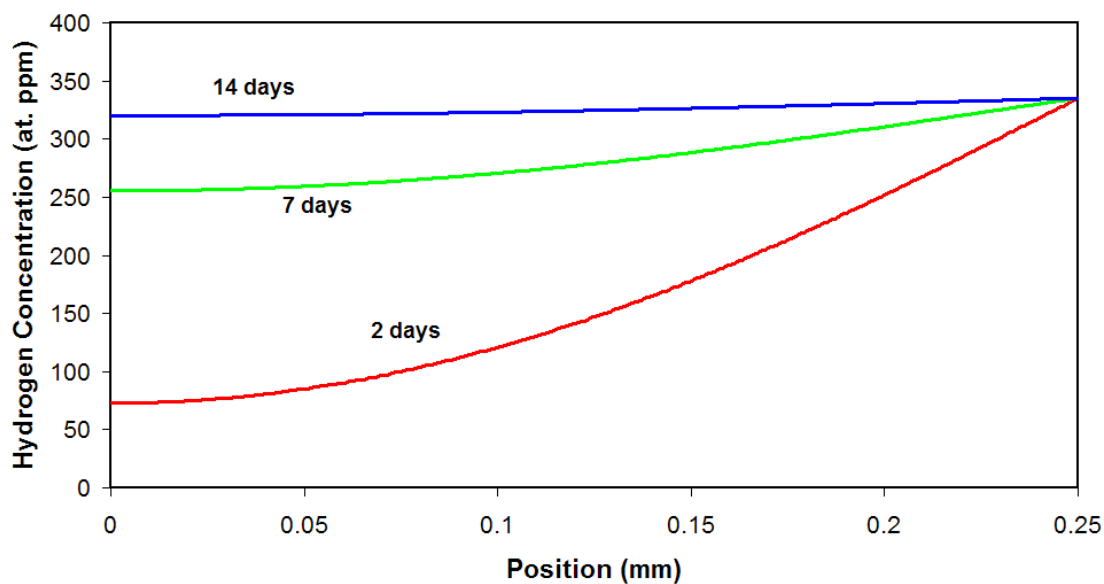


Figure 17: Hydrogen concentration profiles for samples stored in 70 MPa at 373 K

From the above graph, it was decided that the concentration at the center of the sample (i.e. $x = 0$) should be no less than 95% of the concentration at the surface. To demonstrate the effect of hydrogen saturation, two samples were immersed in 70 MPa hydrogen at 373 K for 14 days. A picture of the storage apparatus is shown in Figure 18.



Figure 18: High-temperature hydrogen charge apparatus

Following the soak period, the storage vessels were depressurized and the samples were immediately immersed in liquid nitrogen. The purpose of this step was to reduce the diffusivity of hydrogen through the metal. At such a low temperature (77 K), diffusion is negligible. For example, the depth of penetration (commonly estimated by \sqrt{Dt} ⁶⁰) at 77 K only reaches 3.7×10^{-18} m after 1 day. Even at room temperature, very little hydrogen will diffuse out of the specimens. Equation 13 was again used to estimate the hydrogen loss if the specimen were to remain in an evacuated chamber at room temperature for 1 hour, 1 day, and 1 week. As shown in Figure 19, even 1 week of diffusion at room temperature will have little effect on the hydrogen concentration in the bulk of the material. In this series of testing, samples were only out of liquid nitrogen for a matter of minutes.

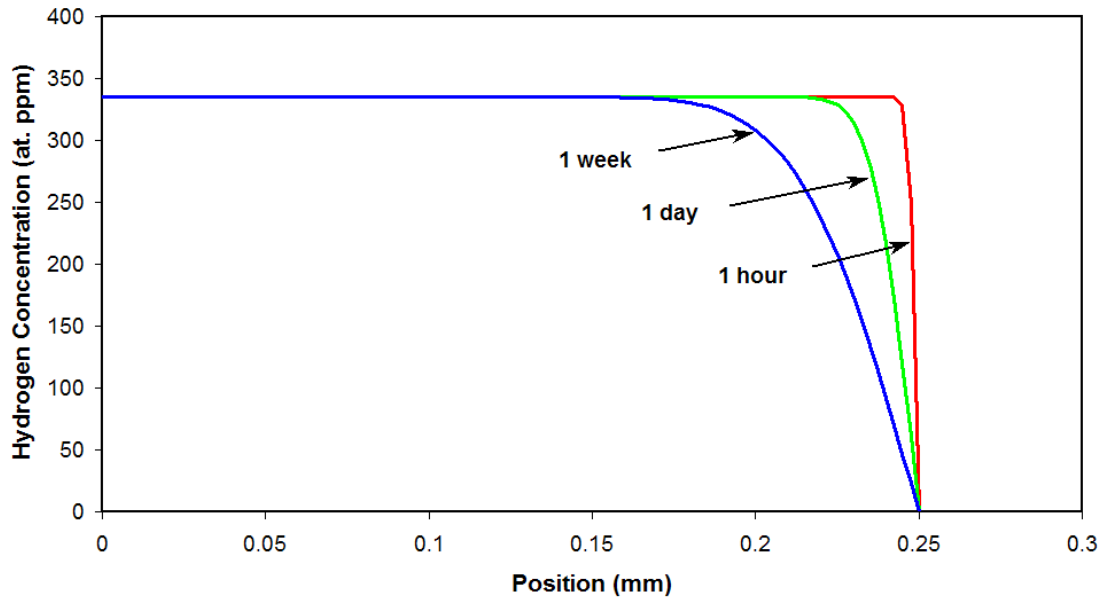


Figure 19: Estimated desorption of hydrogen from a saturated sample in contact with a vacuum

To be absolutely certain that as much hydrogen as possible remained in the samples, they were stored in liquid nitrogen until tested. To ensure that further annealing at this temperature did not affect the material properties, another two specimens were kept in air at 373 K for 14 days. These results were compared to results of testing two specimens that remained in air at room temperature (a summary of test conditions is shown in Table 5). For stress calculations, the thickness of each specimen was recorded (refer to Table 5).

Table 5: Thin tensile test conditions

Sample ID	Material	Storage Pressure (MPa)	Storage Temperature (K)	Storage Time (days)	Thickness (mm)
1	316	As-received			0.66
2	316	As-received			0.65
3	316	Ambient	373	14	0.66
4	316	Ambient	373	14	0.66
5	316	70 MPa	373	14	0.66
6	316	70 MPa	373	14	0.65
L1	316L	As-received			0.52
L2	316L	As-received			0.51
L3	316L	Ambient	373	14	0.50
L4	316L	Ambient	373	14	0.51
L5	316L	70 MPa	373	14	0.49
L6	316L	70 MPa	373	14	0.51

A Sintech testing frame equipped with serrated flat face wedge grips was used to pull the specimens in uniaxial tension until fracture. In accordance with ASTM test standard E8⁵⁴, all samples were tested at a crosshead displacement rate of 5.0 mm/minute.

4.4 Martensite Content Analysis

Quite often in testing of austenitic stainless steels, the ferritescope is used as a quick and convenient method of quantifying martensite content. Basically, the instrument creates a magnetic field and measures the response of the material. Since the ferritescope is calibrated using standard samples of known delta-ferrite concentrations, there is inherent concern of its compatibility with a martensite system. A series of tests were performed to determine if a martensite concentration could be accurately measured using a ferritescope.

4.4.1 Ferritescope Validity Testing

Although stainless steels 316 and 316L are regularly used in fabrication of high-pressure components and storage tanks, this section will focus on the behavior of 301LN. All three are austenitic stainless steels, but 301LN is much more unstable. Lower carbon content and the low nickel-to-nitrogen ratio reduce the stacking fault energy significantly, thus facilitating the formation of α' -martensite. Since an unstable austenitic stainless steel will more readily undergo phase transformation, a broader range of martensite contents can be used to evaluate the accuracy of the ferritescope.

Rectangular sections of 301LN stainless steel were supplied as slabs 20 mm x 100 mm x 2 mm. They were rolled in the longitudinal direction to a final thickness of 0.8mm. Because the rolling created large quantities of deformation-induced martensite, each sample was annealed at 1050°C for 30 minutes. Following the anneal, it was verified magnetically that no martensite was present.

To develop a full stress-strain relationship for characterization of the metal, one sample was pulled in uniaxial tension to failure. A summary of the derived mechanical properties is shown in Table 6. This relationship was used to estimate the necessary load to reach a given strain.

Table 6: Mechanical properties of SS 301LN

Material	σ_{ys} (MPa)	σ_{UTS} (MPa)	ϵ_f (%)
301LN	283.0	1316.4	46.3

A series of samples were then pulled to varying strains evenly distributed along the material's loading path, targeted at 1, 10, 15, 20, 25, 30, 35, and 40%. The actual strains were measured with an extensometer and are graphically represented with relation to the initial tensile test in the stress-strain curve in Figure 20. Both ferritescope and XRD measurements were taken to test their proficiencies.

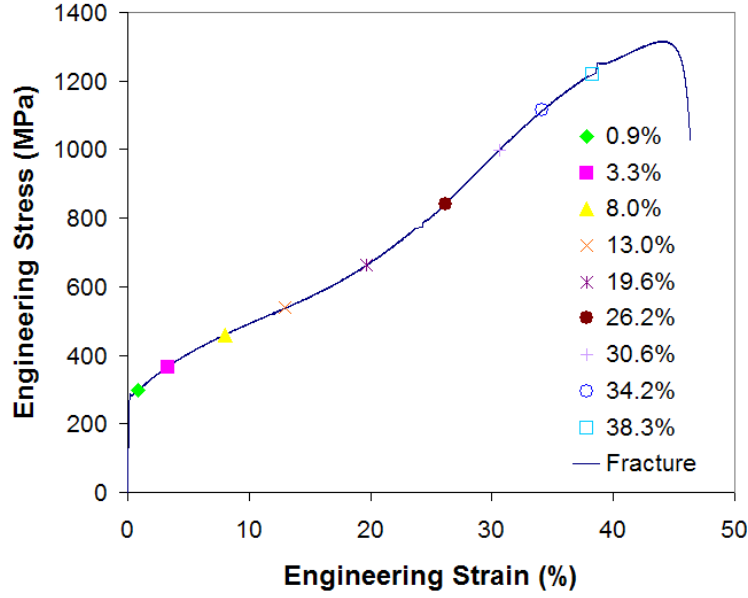


Figure 20: Actual applied strains for ferritescope validity test

A 20mm x 20mm section was removed from the center of each gauge section for analysis. A ferritescope (Fischer Feritscope® MP30) was used to estimate the mass fraction of magnetic martensite and a Rigaku Multiflex X-ray diffractometer was used for XRD measurements. All XRD data was processed and analyzed using GSAS and EPXGUI software^{61,62}. Crystallographic information of the two phases of interest were communicated to the program in the form of CIF files. Both having cubic structures, the austenite phase was identified with a lattice parameter of 3.591 Å and a $Fm\bar{3}m$ space group, and the martensite phase was identified with a lattice parameter of 2.873 Å and an $Im\bar{3}m$ space group. After each refinement, the phase fraction of the diffraction pattern was recorded.

Figure 21 shows the XRD patterns for the nine strained samples. As labeled on the right, the extent of strain imparted increases from the top graph to the bottom. The distinction between phases is clearly shown by the increasing and decreasing peak intensities; as strain increases, the austenite peaks get smaller as the martensite peaks get larger.

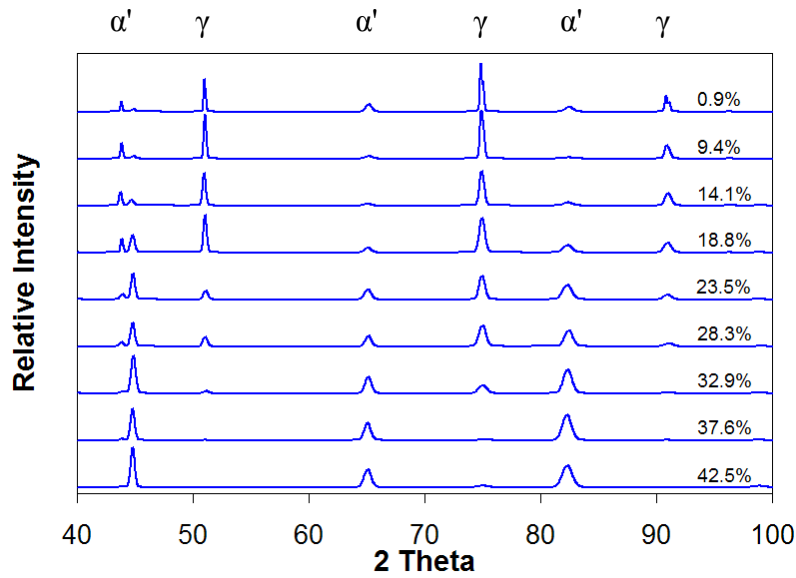


Figure 21: Diffraction patterns of deformed specimens

The results from the ferritescope and XRD measurements are shown in Table 7. Figure 22 provides a graphical representation of the results from both the ferritescope and XRD measurements, plotted as the martensite measurement of the sample versus the strain imparted.

Table 7: Martensite measurement results

Sample ID	Target Strain (%)	Applied Strain (%)	Ferritescope (wt%)	XRD (wt%)
1	As-received	0.0	0.0	0.0
2	1	0.9	2.6	6.3
3	10	9.4	8.9	13.1
4	15	14.1	12.7	11.5
5	20	18.8	19.8	29.7
6	25	23.5	34.2	56.5
7	30	28.3	40.6	60.2
8	35	32.9	49.6	84.8
9	40	37.6	50.6	93.6
10	Fracture	42.5	54.5	93.3

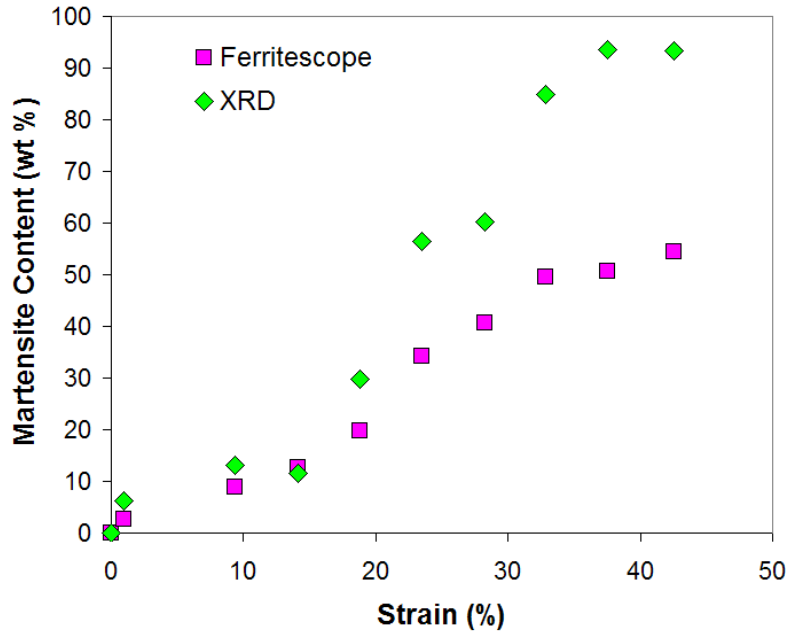


Figure 22: Martensite measurements from ferritescope and XRD

It was demonstrated that the ferritescope had precision and repeatability, but lacked accuracy. A very consistent calibration equation would be drawn from the measurements, but because it is based on a calibration with delta ferrite, results are unreliable – they do not reflect the actual martensite content. The XRD, on the other hand, provided more representative measurements, but the method was inconsistent; there was a larger variance between the calibration equation and the data points. This is largely due to the effect of texture on XRD results.

4.4.2 Magnetic Measurement Procedure

For α' -martensite content analysis in each series of tensile tests, it was necessary to have standard samples with known contents for reference. Because the martensite formed in both SUS 316 and 316L will have the same magnetic properties, reference specimens were prepared from SUS 316. Three reference specimens were prepared with varying martensite contents for assurance of an accurate measurement. To achieve this, the samples were plastically deformed at -40°C to create strain-induced α' -martensite. They were analyzed using the magnetic balance method^{63,64} that attributed a magnetic

force to the martensite content. The samples were then sectioned longitudinally, mounted in epoxy resin, and polished to 1.0 μm surface roughness. Because mechanical polishing may induce further phase transformation, the mounted sample was etched to remove a thin layer of possible altered material. The etchant used was composed of equal parts hydrochloric acid (HCl), nitric acid (HNO_3), and distilled water. Each sample was etched for approximately five minutes.

XRD analysis was performed on the mounted sample to determine the precise BCC α' -martensite content in terms of mass percentage. The analysis was conducted at the Earth and Ocean Sciences' Electron-Microbeam and X-Ray Diffraction Laboratory at the University of British Columbia. Resulting XRD scans for the three reference samples can be seen in Figure 23 to Figure 25. The blue line represents the response from the scan whereas the other two lines designate the angle and intensity of peaks of austenite and martensite (color designation is indicated in the top right corner). Because the strain-induced martensite would have a lattice parameter virtually identical to that of alpha-iron (approximately 2.877 Å), its pattern was used as a proxy for the martensite content analysis. The noise reported by the XRD scan is evident of crystallographic orientation and was responsible for inducing an error of up to 2%.

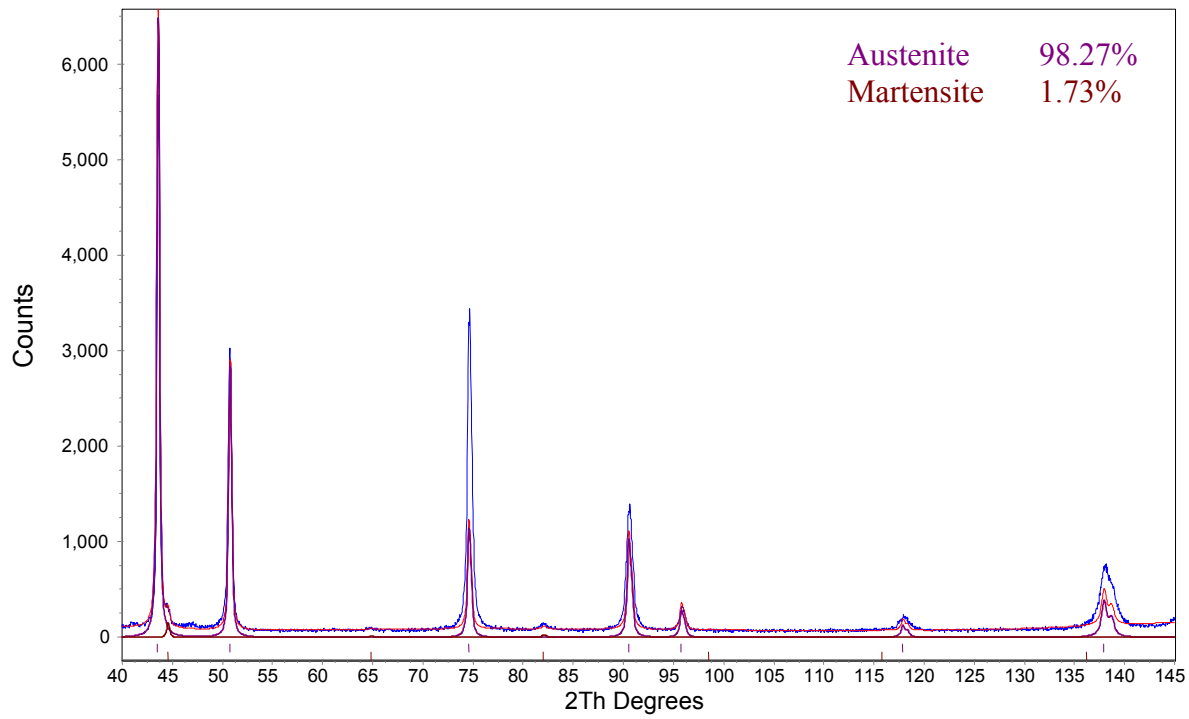


Figure 23: XRD scan of reference sample R1

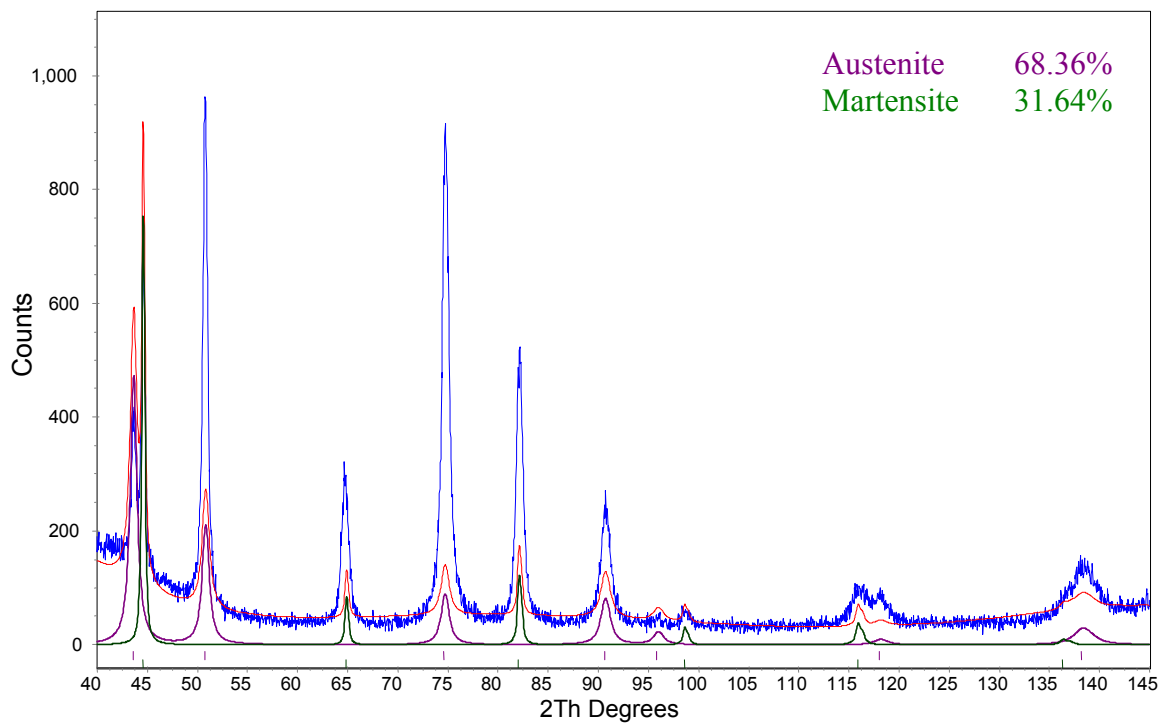


Figure 24: XRD scan of reference sample R2

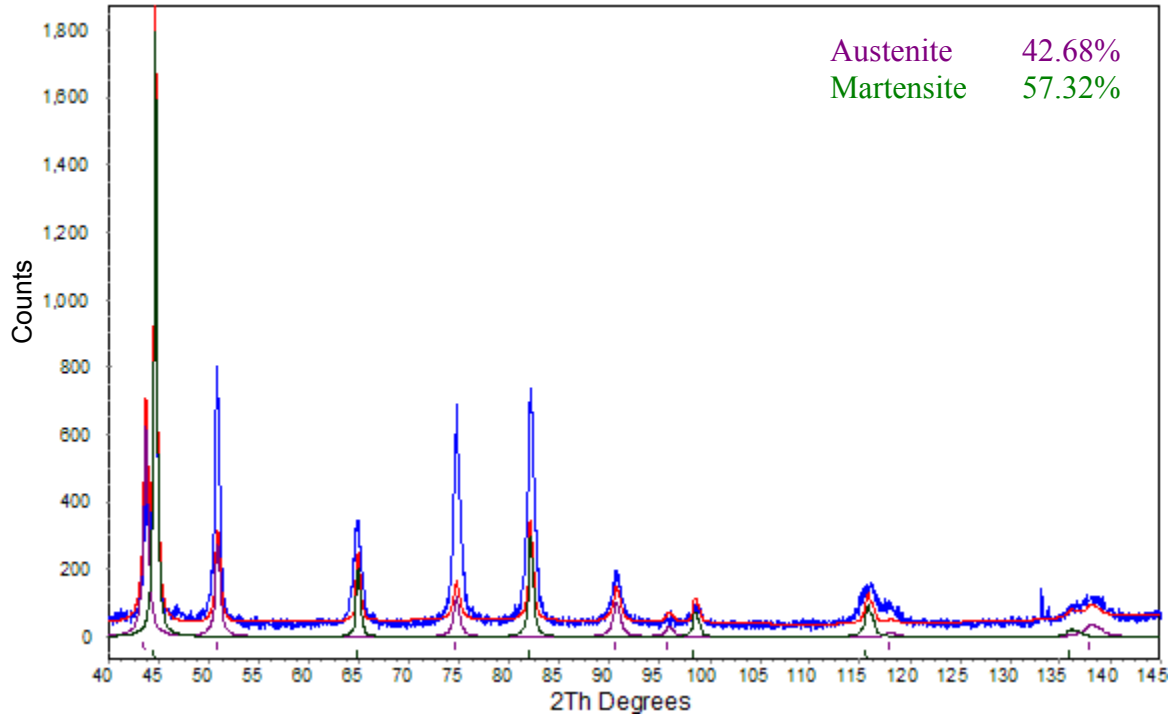


Figure 25: XRD scan of reference sample R3

A relationship can be made between the magnetic force and the martensite content, as shown in Table 8. The martensite content listed was derived from the intensity of the various peaks in the XRD pattern. It was assumed that strain-induced martensite was evenly distributed through the thickness and that martensite and austenite were the only phases present. These assumptions were later confirmed through optical microscopy.

Table 8: Reference sample martensite measurements

Sample ID	Martensite Content (wt %)	Magnetic Measurement (g)
R1	1.7	-64.0
R2	31.6	-674.6
R3	57.3	-1019.1

As adapted from methods reported by Radu et al.⁶³ and Talonen et al.⁶⁴, the magnetic attraction of martensite was used to quantify its content. Upon comparison to several other measurement techniques, the magnetic balance method was deemed a

“reliable and rapid way to measure α' -martensite content”⁶⁴. Also, it was found to be sensitive to very low martensite contents.

A powerful rare earth magnet was placed on an analytical balance and the mass was recorded. Using a sensitive servo-hydraulic actuator, the tensile sample was held in place slightly above the magnet – as close as possible, without touching it. A picture of the setup can be seen in Figure 26. The magnetic attraction to the specimen caused the mass measured by the balance to decrease. The mass reading was again recorded. A hydraulic actuator was lowered away from the specimen until it was outside of the magnetic field and the reading was the same as initially recorded. The difference in the recorded masses is representative of the magnetic attraction.

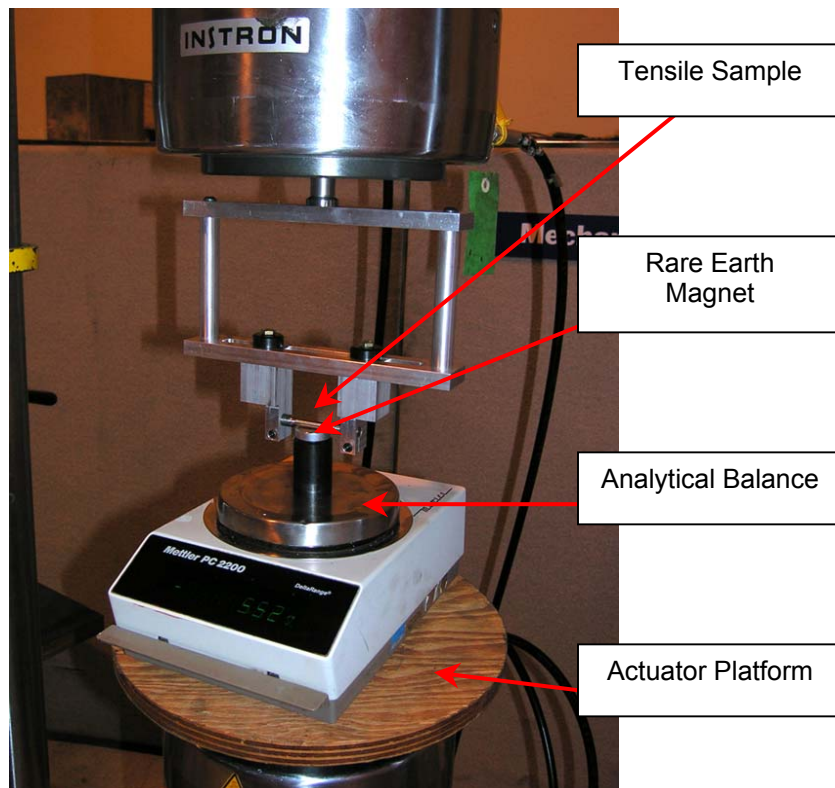


Figure 26: Magnetic balance method test setup

The force measured by the magnetic balance method is linearly proportional to the mass content of α' -martensite in the sample⁶⁴. By comparing the magnetic force to that of a sample of known α' -martensite concentration, the unknown content can be expressed as follows:

$$c_{\alpha'} = \frac{B_{meas}}{B_{ref}} c_{\alpha'_{ref}} \quad [14]$$

where $c_{\alpha'}$ is the α' -martensite content of the sample being tested, $c_{\alpha'_{ref}}$ is the α' -martensite content of the reference sample, B_{meas} is the change in mass reading of the measured sample being tested, and B_{ref} is the change in mass reading of the reference sample. By applying a linear fit to the reference points, Equation 1 can be represented as follows:

$$c_{\alpha'} = -0.0533 B_{meas} \quad [15]$$

As can be seen in Figure 27, the representative fit provides a reasonable estimation, with consideration to the impending limitations of slight sample variabilities. The R^2 figure was used to quantify the validity of the linear fit. A data set perfectly characterized by a certain equation would have an R^2 value of 1. Having a value of approximately 0.98, the generated equation was considered depictive of the experimental data.

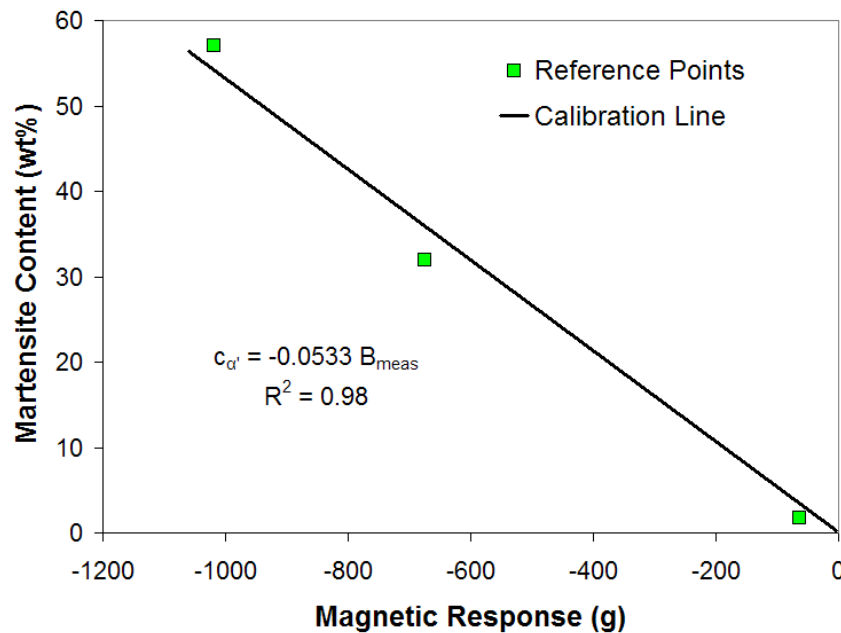


Figure 27: Magnetic response of reference samples

The material was supplied by Powertech Labs in the form of hot extruded bar. It was requested that the material be tested in the as-received condition for the purpose of replicating. To account for any α' -martensite formed during solidification or forming, both contributing to magnetic attraction, initial magnetic measurements and the corresponding calculations of martensite content were conducted (refer to Table 9 for values). Initial measurements were subtracted from post-test measurements to determine only the quantity of strain-induced α' -martensite. Testing by Talonen et al.⁶⁴ showed that changes in the dimensions due to plastic deformation had negligible influence on measured α' -martensite content.

Table 9: Initial magnetic attraction measurements

SUS 316			SUS 316L		
Sample ID	Initial Reading (g)	Martensite Content (%)	Sample ID	Initial Reading (g)	Martensite Content (%)
1	-2.11	0.112	L1	-5.51	0.294
2	-2.05	0.109	L2	-5.31	0.283
3	-2.23	0.119	L3	-5.24	0.279
4	-2.09	0.111	L4	-5.12	0.273
5	-2.27	0.121	L5	-4.46	0.238
6	-2.22	0.119	L6	-5.76	0.307

4.5 Microscopy

Three methods of microscopy were used to examine the material tested. Initially, a stereomicroscope was used to capture the fracture zones of tensile specimens. Surface cracking and general deformation trends can be seen from images taken at a magnification of 7 times.

The deformed gauge sections of the tensile specimens were sliced to expose their longitudinal cross-sections. After mounting in an epoxy resin and polishing with 0.03 μm alumina slurry, the sample was electropolished in a 900 mL perchloric and 45 mL hydrochloric acid solution. Electropolishing was performed to remove a thin layer of

material that may have been affected by mechanically polishing. The microstructure was revealed by etching with a solution of 50 mL distilled water, 10 mL hydrochloric acid, and 0.15 g potassium metabisulfite. Under a fume hood, the chemical attack continued until the surface attained a faint brown hue. A Zeiss optical microscope was used to take representative photos of the specimen microstructure at various magnifications.

Finally, the fracture surface of each specimen was viewed at high magnification with a Hitachi S-2500 SEM. The SEM was used to ascertain more detailed features to characterize the mode of failure. Representative micrographs were taken at a magnification of one thousand times.

5.0 Results

The tests conducted have supported findings from literature as well as presented new evidence for the mechanical behavior of SS 316 and 316L tested in various conditions. Mechanical response was compared with respect to stacking fault energy of the alloy, gaseous medium, test temperature, and hydrogen pressure. The effect of gaseously pre-charging thin tensile specimens was also determined. In this section, the results from the hydrogen environment and hydrogen charged tensile tests will be reviewed.

5.1 Hydrogen Environment Tensile Tests

Tensile tests were performed within a pressurized hydrogen environment in order to determine the effect of hydrogen gas on the mechanical properties of the alloys in question. Test conditions were varied with respect to test gas, temperature, and pressure with hopes to reveal the contributing factors to hydrogen embrittlement of austenitic stainless steels. In doing so, it was hoped to further develop procedure and criteria for high-pressure hydrogen compatibility testing.

5.1.1 Tensile Test Results

The tensile tests demonstrated the behavioral difference of the materials when tested in hydrogen versus helium, and at -40°C versus room temperature. Macroscopic pictures of the fractured samples can be seen in Figure 28 through Figure 35. It can be seen that each specimen fractured near the center of the gauge section.



Figure 28: 316 tested in 25 MPa He at 20°C



Figure 29: 316 tested in 25 MPa H₂ at 20°C



Figure 30: 316 tested in 25 MPa He at -40°C



Figure 31: 316 tested in 25 MPa H₂ at -40°C



Figure 32: 316L tested in 25 MPa He at 20°C



Figure 33: 316L tested in 25 MPa H₂ at 20°C



Figure 34: 316L tested in 25 MPa He at -40°C



Figure 35: 316L tested in 25 MPa H₂ at -40°C

The stress-strain relationship of SUS 316 seemed to be uninfluenced by a hydrogen atmosphere to strains well past the point of yielding. However, the elongation

and reduction in cross-sectional area were much lower when tested in hydrogen than in helium. A summary of the results, including 0.2% offset yield stress (σ_{ys}), ultimate tensile strength (σ_{UTS}), plastic elongation to failure (ϵ_f as measured from a 25.4 mm gauge length), and reduction of cross-sectional area, is located in Table 10.

Table 10: Summary of tensile test results for SUS 316

Sample	Temperature (°C)	Gaseous Medium	σ_{ys} (MPa)	σ_{UTS} (MPa)	ϵ_f (%)	Reduction of Area (%)
T1	20	25 MPa He	519	723	62.6	73.5
T2	20	25 MPa H ₂	525	736	50.4	44.2
T3	-40	25 MPa He	521	802	69.6	77.7
T4	-40	25 MPa H ₂	580	811	31.8	24.8

A comparison of the stress-strain curves is shown in Figure 36. Serrations in the data for tests performed at 20°C were the result of noise in load measurement rather than material characteristics. Following data processing, tests at -40°C were conducted using a load cell with a smaller range. As earlier mentioned, the extensometer was removed prior to fracture, so the strain data was calculated from the crosshead extension.

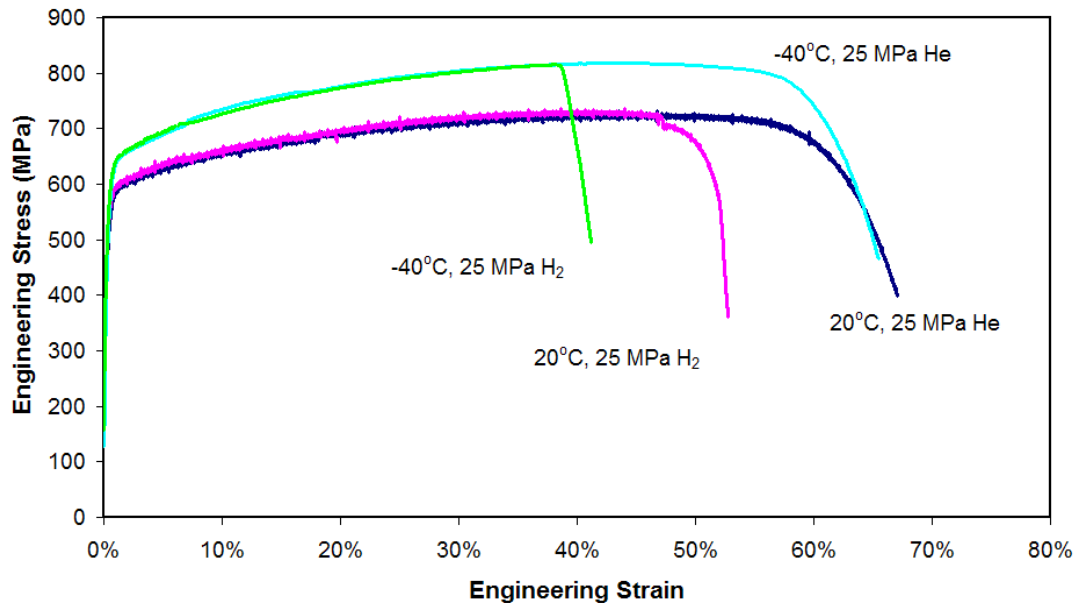


Figure 36: Stress-strain behavior of SUS 316 tested in helium and hydrogen

As with SUS 316, 316L had a very similar loading pattern whether tested in helium or hydrogen. This can be seen in Figure 37.

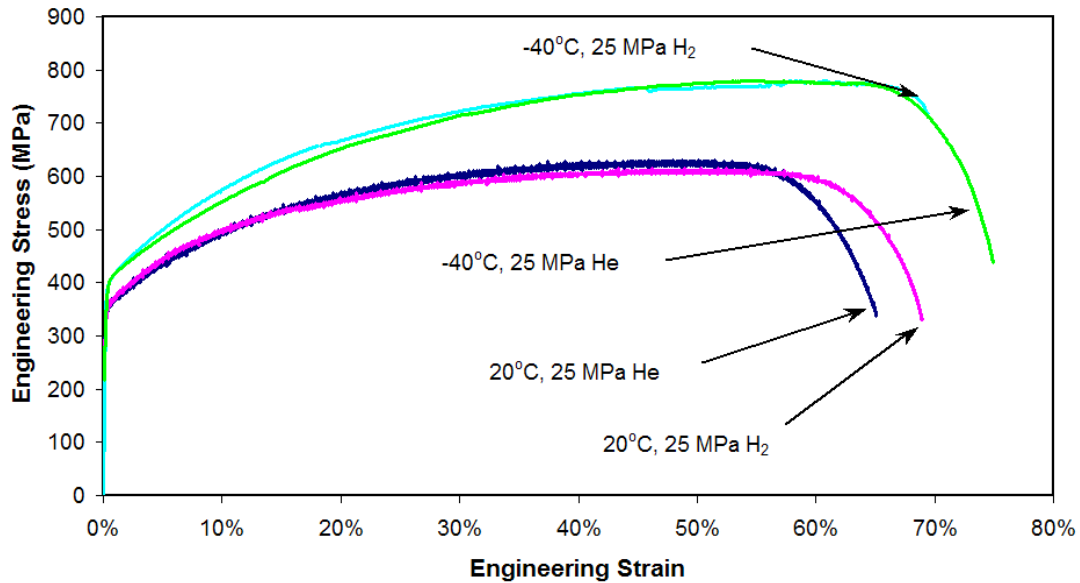


Figure 37: Stress-strain behavior of SUS 316L tested in helium and hydrogen

Even until the point of fracture, SUS 316L was seemingly unaffected by the hydrogen atmosphere. As shown in Table 11, along with the yield and tensile strengths, the elongation and reduction in cross-sectional area are similar. As measured by the magnetic method following fracture, martensite content also remained constant.

Table 11: Summary of tensile test results for SUS 316L

Sample	Temperature (°C)	Gaseous Medium	σ_{ys} (MPa)	σ_{UTS} (MPa)	ϵ_f (%)	Reduction of Area (%)
TL1	20	25 MPa He	349	631	65.2	76.9
TL2	20	25 MPa H ₂	350	615	68.0	75.3
TL3	-40	25 MPa He	395	780	75.7	76.5
TL4	-40	25 MPa H ₂	406	782	71.5	70.1

5.1.2 Stereo Microscopy

To determine the failure mechanism, the gauge sections of the fractured specimens were viewed with a stereomicroscope. As seen in Figure 38, a cup and cone failure signifies the ductile failure experienced by the sample tested in helium. Figure 39 clearly shows a brittle fracture mode in the sample tested in hydrogen, as surface cracking was observed across the length of the gauge section (i.e. not restricted to the necked region). In both cases, final fracture occurred after the onset of necking.

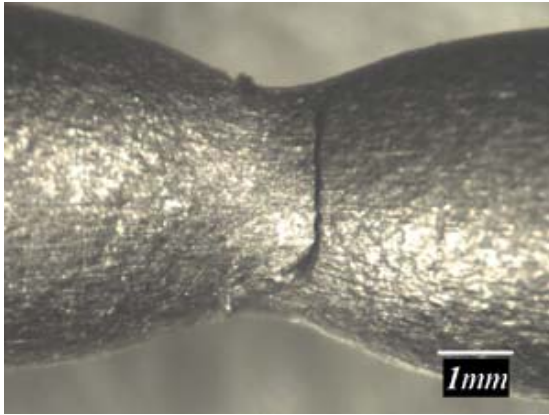


Figure 38: 316 tested in 25 MPa He at 20°C (7x)

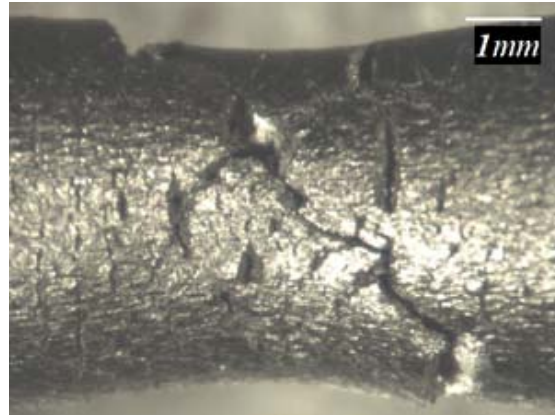


Figure 39: 316 tested in 25 MPa H₂ at 20°C (7x)

When tested at -40°C, SS 316 once again displays a ductile fracture zone with helium as a gaseous medium, and brittle surface cracks with hydrogen as a gaseous medium. A comparison is shown in Figure 40 and Figure 41. As seen here, the sample tested in helium fractured following the onset of necking, whereas the sample tested in hydrogen had yet to reach the point of localized deformation.

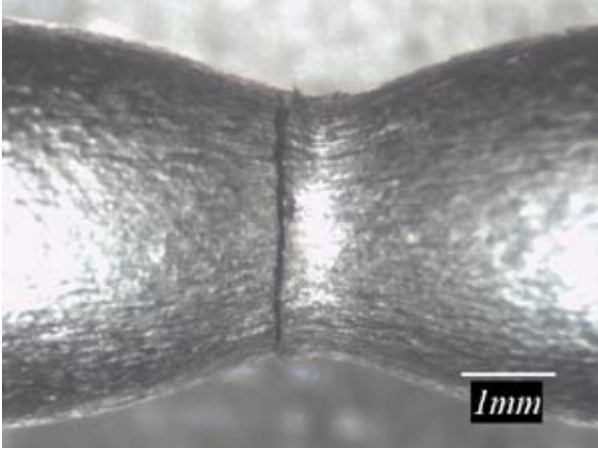


Figure 40: 316 tested in 25 MPa He at -40°C (7x)

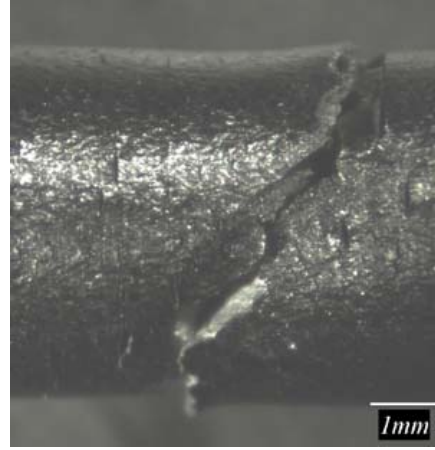


Figure 41: 316 tested in 25 MPa H₂ at -40°C (7x)

There is no clear distinction between the fracture zones when 316L is tested in hydrogen versus helium at room temperature. Figure 42 shows the fracture zone of the specimen tested in helium and Figure 43 shows the specimen tested in hydrogen.

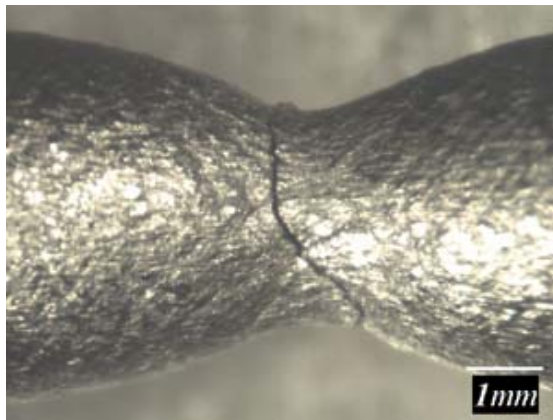


Figure 42: 316L tested in 25 MPa He at 20°C (7x)

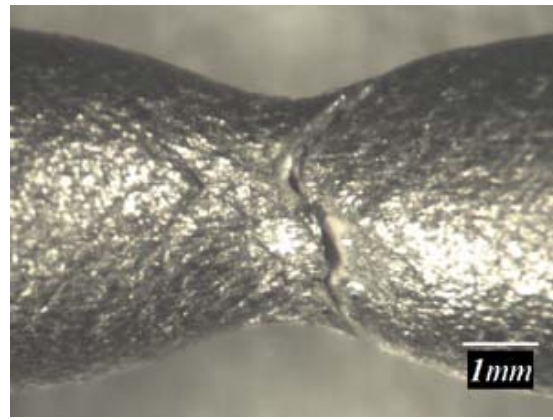
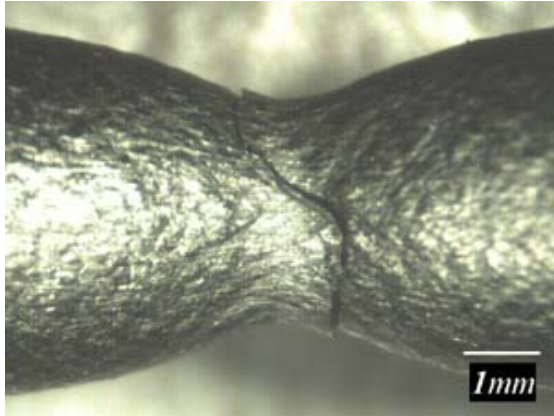
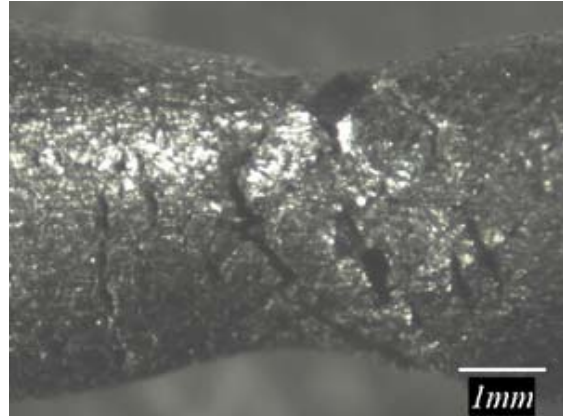


Figure 43: 316L tested in 25 MPa H₂ at 20°C (7x)

As opposed to its behavior at room temperature, SS 316L fails in a brittle fashion near its fracture zone when tested in a hydrogen atmosphere. Although the embrittlement occurs to a lesser extent, a comparison can be made between Figure 44 and Figure 45.



**Figure 44: 316L tested in 25 MPa He at -40°C
(7x)**



**Figure 45: 316L tested in 25 MPa H₂ at -40°C
(7x)**

5.1.3 Optical Microscopy

Prior to the metallographic examination of the fractured samples, the microstructures of both materials were examined for grain size and the presence of martensite. As shown in Figure 46 and Figure 47, the partially re-crystallized microstructure indicates that the material was supplied in the hot deformed state. It consisted mainly of the austenite phase with scattered presence of lath martensite. The grain size of the supplied SS 316 was approximately 20 μm and that of SS 316L was approximately 40 μm .

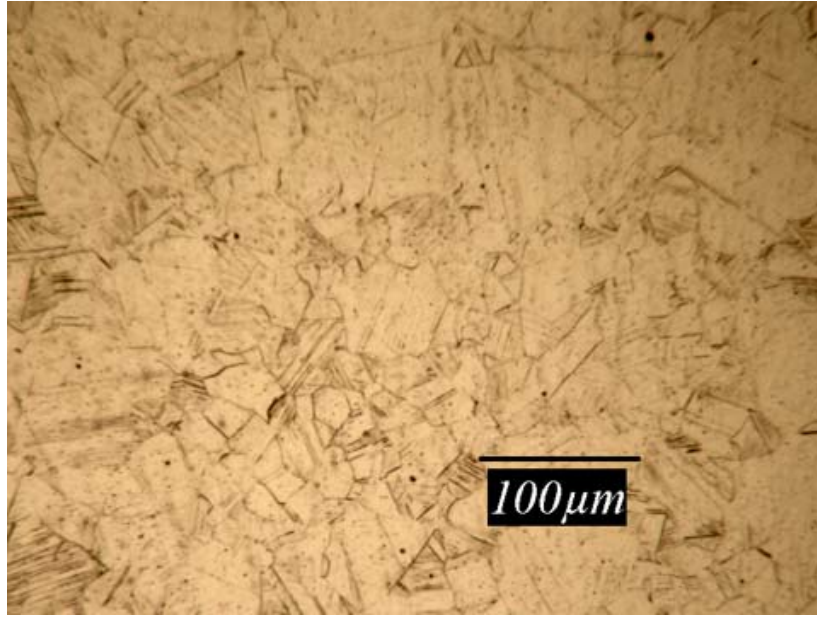


Figure 46: SS 316 microstructure as-received (200x)

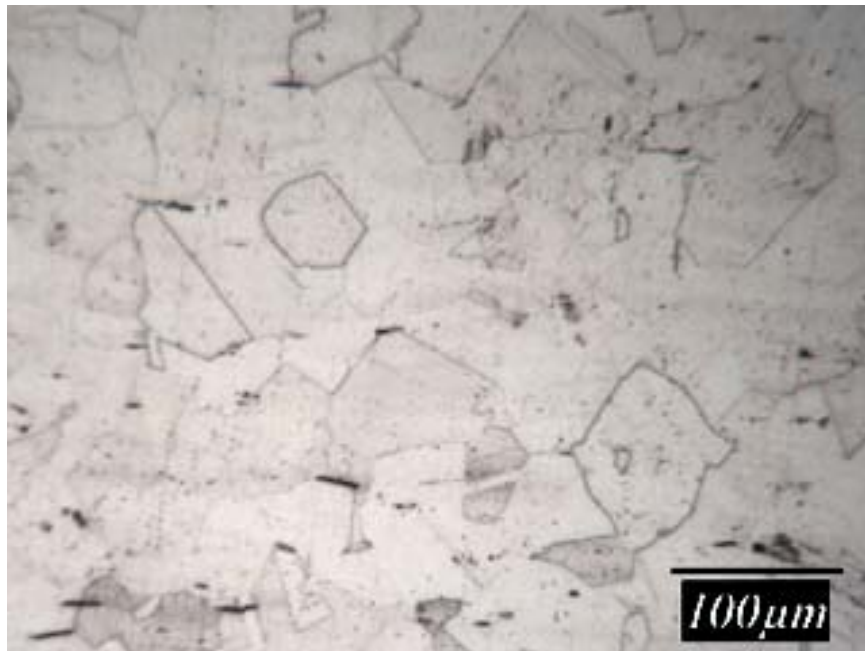


Figure 47: SS 316L microstructure as-received (200x)

Polished cross-sections of the fractured specimens were examined with an optical microscope. The principal intension here was to examine the distribution of martensite formed during deformation. Typically, each sample had a much higher concentration of

martensite at the necked region and fracture surface consistent with the magnitude of localized strain experienced. An example of the graduation can be seen in Figure 48.



Figure 48: Example of martensite distribution in hydrogen environment tensile sample

Areas of the gauge section that underwent uniform elongation displayed typical patterns of martensite formation. Evidence of martensite formation in each specimen (as indicated with a black arrow) is shown in Figure 49 through Figure 56. The laths of martensite are identified by their feathered appearance.



Figure 49: 316 tested in 25 MPa He at 20°C showing very little martensite (200x)

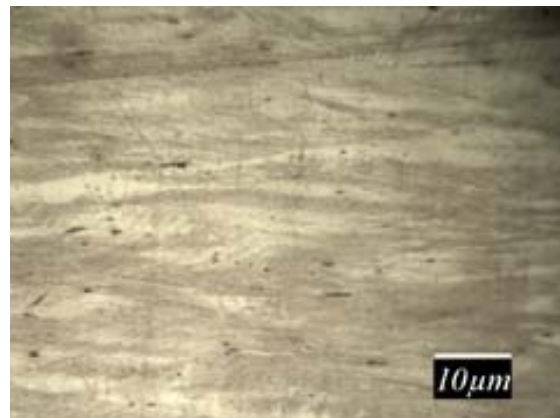


Figure 50: 316 tested in 25 MPa H₂ at 20°C showing nearly no martensite (500x)

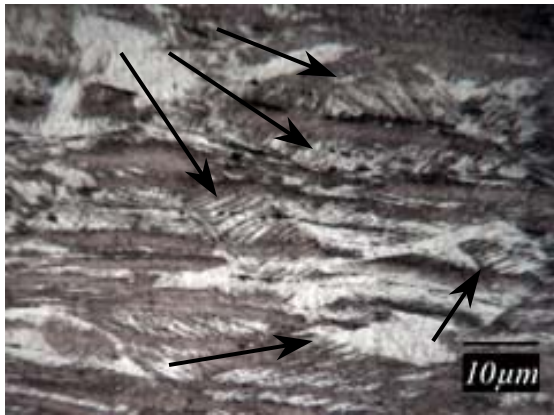


Figure 51: 316 tested in 25 MPa He at -40°C showing lots of martensite (500x)

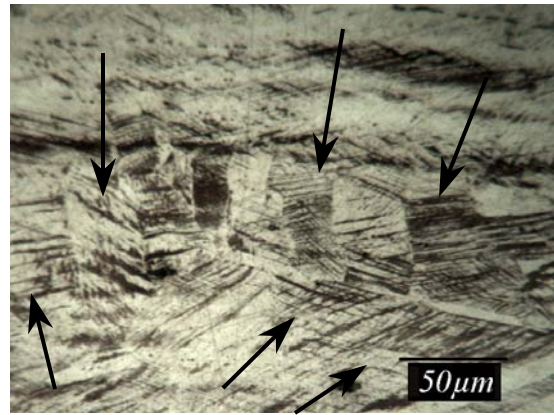


Figure 52: 316 tested in 25 MPa H_2 at -40°C showing lots of martensite (200x)

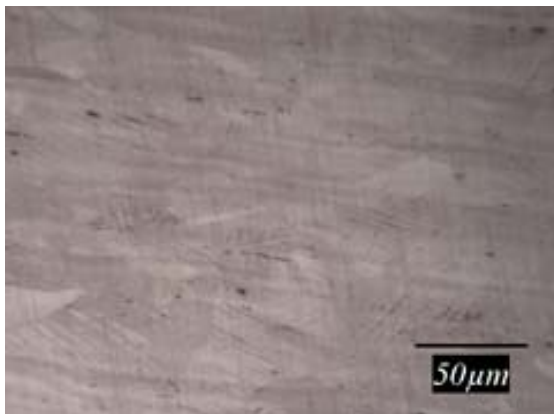


Figure 53: 316L tested in 25 MPa He at 20°C showing almost no martensite (200x)

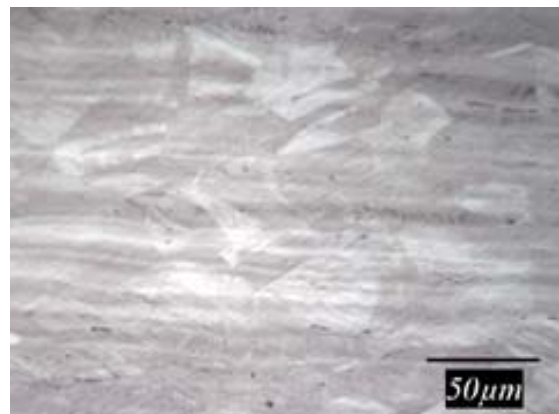


Figure 54: 316L tested in 25 MPa H_2 at 20°C showing almost no martensite (200x)

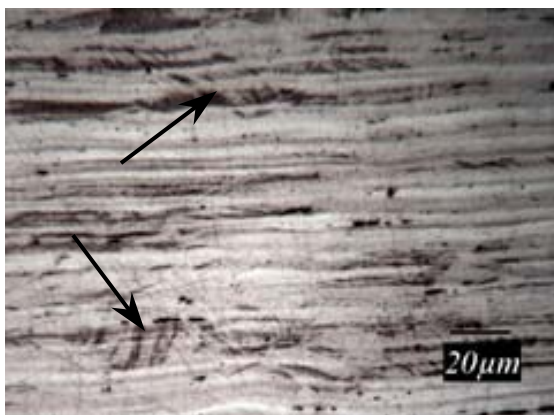


Figure 55: 316L tested in 25 MPa He at -40°C showing some martensite (200x)

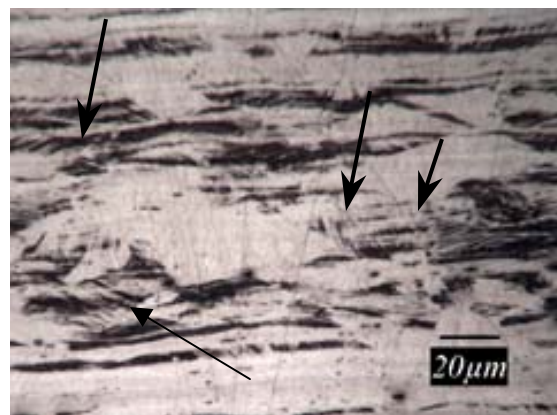


Figure 56: 316L tested in 25 MPa H_2 at -40°C showing some martensite (200x)

Those specimens that exhibited brittle cracks contained no signs of cracking in the bulk of the material. Most cracks initiated radially and propagated toward the center. Often, the crack terminated at a grain boundary, and continued to propagate axially in both directions along the same grain boundary. Similarly, at several points, the radial cracks branch off in the axial direction along grain boundaries. An example is shown in Figure 57. Special attention was paid to the area surrounding surface cracks found in samples fractured in hydrogen. It should be noted that martensite seems to be preferentially formed ahead of the propagating crack.

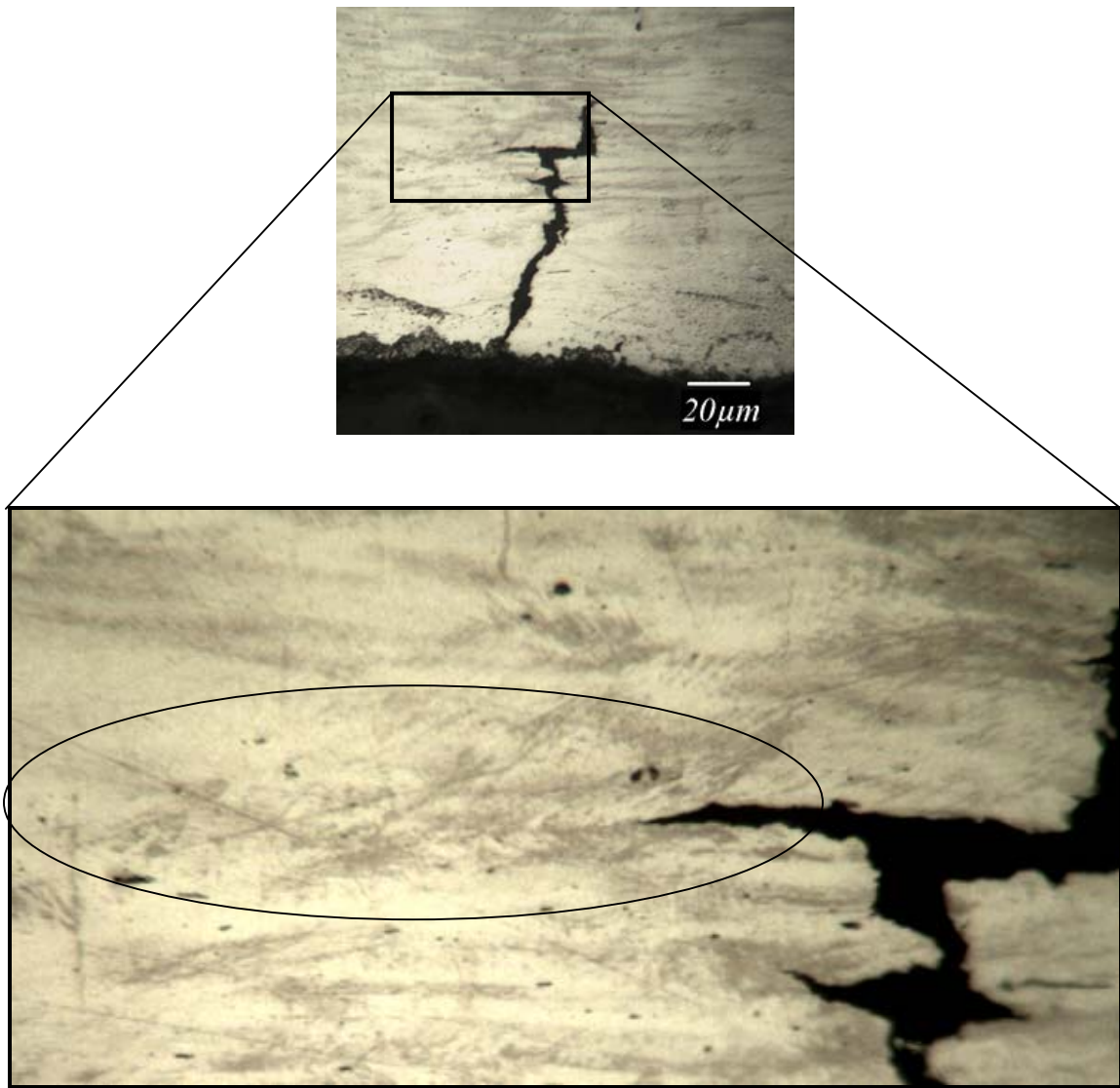


Figure 57: 316 tested in 25 MPa H₂ at 20°C showing martensite ahead of a crack tip (500x)

5.1.4 Scanning Electron Microscopy

Representative high magnification SEM micrographs were taken of the exposed fracture surfaces (Figure 58 to Figure 66). All specimens tested in helium displayed micro-void coalescence (indicative of ductile fracture). Specimens TL2 and TL4 (material 316L tested in hydrogen at room temperature and at -40°C, respectively) also displayed the same behavior. Specimen T1 (SS 316 tested at room temperature) displayed a predominantly brittle fracture surface, featuring intergranular cracking and

transgranular cleavage across the entire surface. Specimen T4 (SS 316 tested in hydrogen at -40°C) displayed a large area of ductile fracture near the center of the specimen (Figure 62).

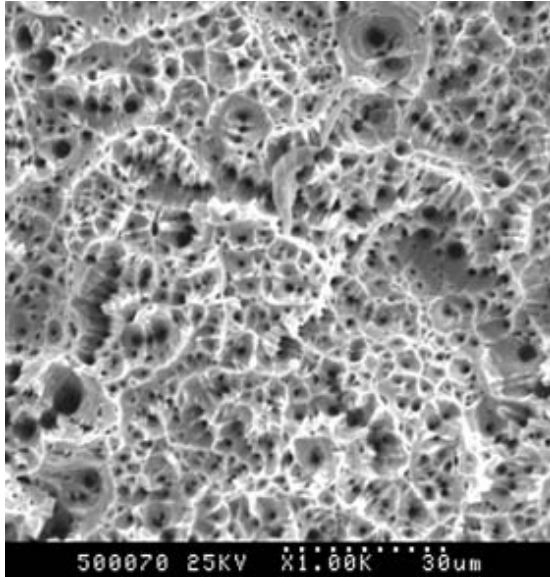


Figure 58: 316 tested in 25 MPa He at 20°C showing ductile fracture (1000x)

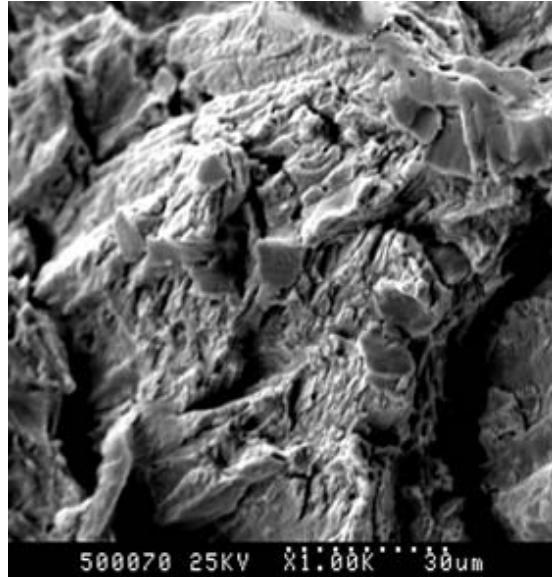


Figure 59: 316 tested in 25 MPa H_2 at 20°C showing brittle fracture (1000x)

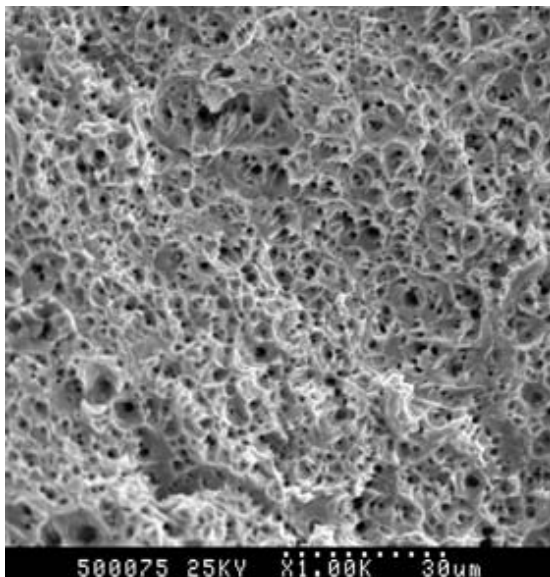


Figure 60: 316 tested in 25 MPa He at -40°C showing ductile fracture (1000x)

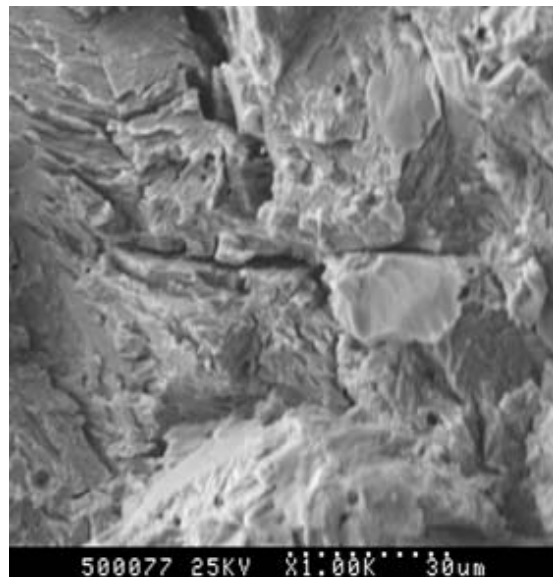


Figure 61: 316 tested in 25 MPa H_2 at -40°C showing brittle fracture (1000x)

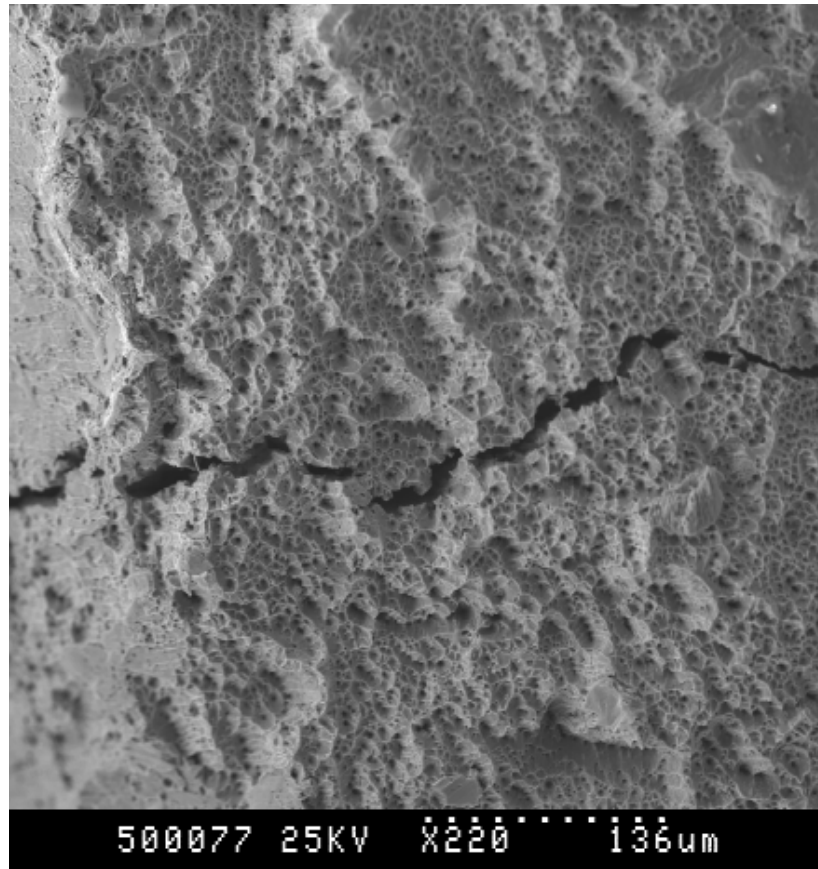


Figure 62: 316 tested in 25 MPa H₂ at -40°C showing ductile features near center (220x)

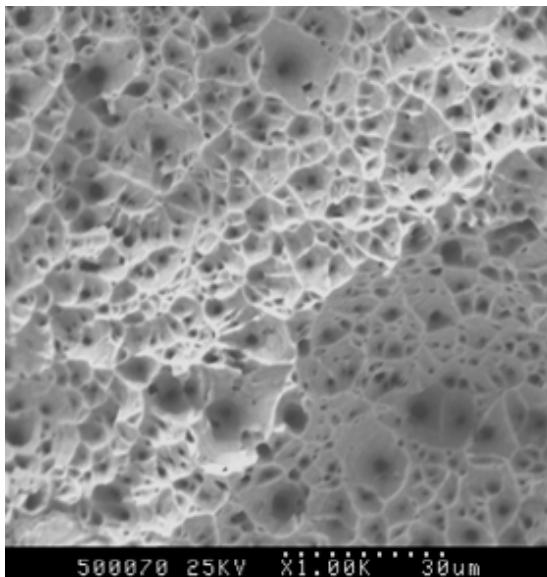


Figure 63: 316L tested in 25 MPa He at 20°C showing ductile fracture (1000x)

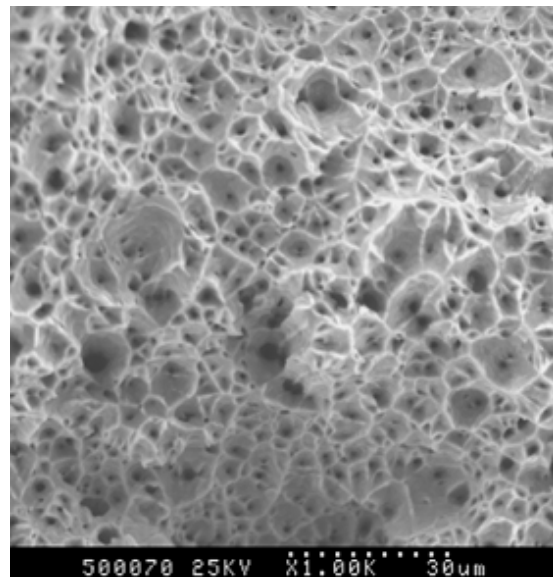


Figure 64: 316L tested in 25 MPa H₂ at 20°C showing ductile fracture (1000x)

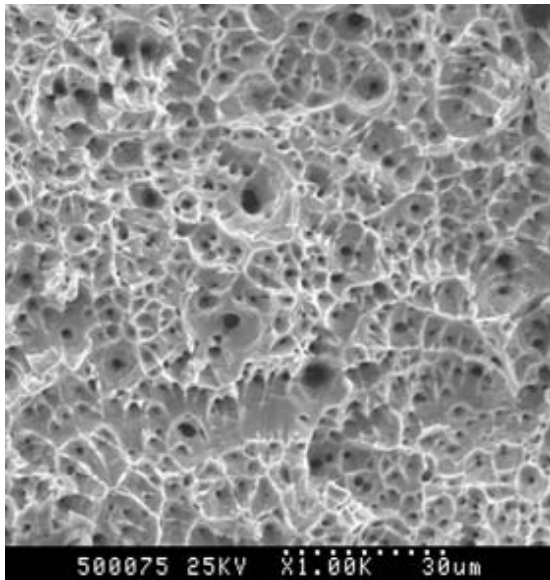


Figure 65: 316L tested in 25 MPa He at -40°C showing ductile fracture (1000x)

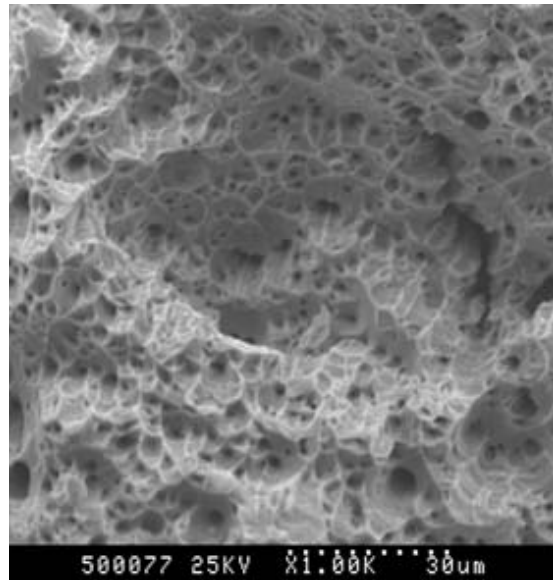


Figure 66: 316L tested in 25 MPa H₂ at -40°C showing ductile fracture (1000x)

While the features of sample TL4 are predominantly ductile, there were areas near the edge displaying planar fracture, assumably faces of surface cracks. These are most likely the regions failure was initiated. An additional SEM picture is shown in Figure 67.



Figure 67: 316L tested in 25 MPa H₂ at -40°C showing brittle-to-ductile transition (300x)

5.1.5 Martensite Content Analysis

The magnetic response of each fractured tensile sample was measured and the martensite content was calculated. It is clear that martensite was formed more readily in samples of SS 316, than 316L. Also, as expected, both materials experienced a higher degree of phase transformation at -40°C. SS 316 formed much less martensite when tested in hydrogen as opposed to helium, however it reached a higher strain to failure in a helium atmosphere. A summary of the results can be found in Table 12.

Table 12: Martensite content of fractured tensile specimens

Sample	Material	Temperature (°C)	Gaseous Medium	Pressure (MPa)	Martensite Content (wt%)
T1	316	20	He	25	2.9
T2	316	20	H ₂	25	2.5
T3	316	-40	He	25	44
T4	316	-40	H ₂	25	15
TL1	316L	20	He	25	0.2
TL2	316L	20	H ₂	25	0.2
TL3	316L	-40	He	25	7.7
TL4	316L	-40	H ₂	25	8.8

5.2 Hydrogen Charge Tensile Tests

As determined from the hydrogen environment tests, cracks were noticed at the surface but absent in the bulk of the material. It should then be questioned whether the embrittlement effect is location specific due to the solute hydrogen concentration. Hydrogen charge tensile tests were used to show the dependence of bulk hydrogen concentration on hydrogen embrittlement. Prior to performing gaseous hydrogen charging, permeation tests were used to confirm that hydrogen was entering the material.

5.2.1 Permeation Test Results

The permeation tests adequately satisfied their primary purpose by proving that hydrogen will enter into and diffuse through the material. As seen in Figure 68 the results are plotted as the hydrogen concentration measured from the gas chromatograph versus the residence time. Also shown in the plot, a linear fit was applied to each set of data points. The data clearly shows that hydrogen gas permeated the material and permeation results were strongly dependant on temperature. The correlation with temperature followed a linear relationship, as would be expected for an Arrhenius process. In the discussion section, these results will be analyzed to determine the permeability of the material.

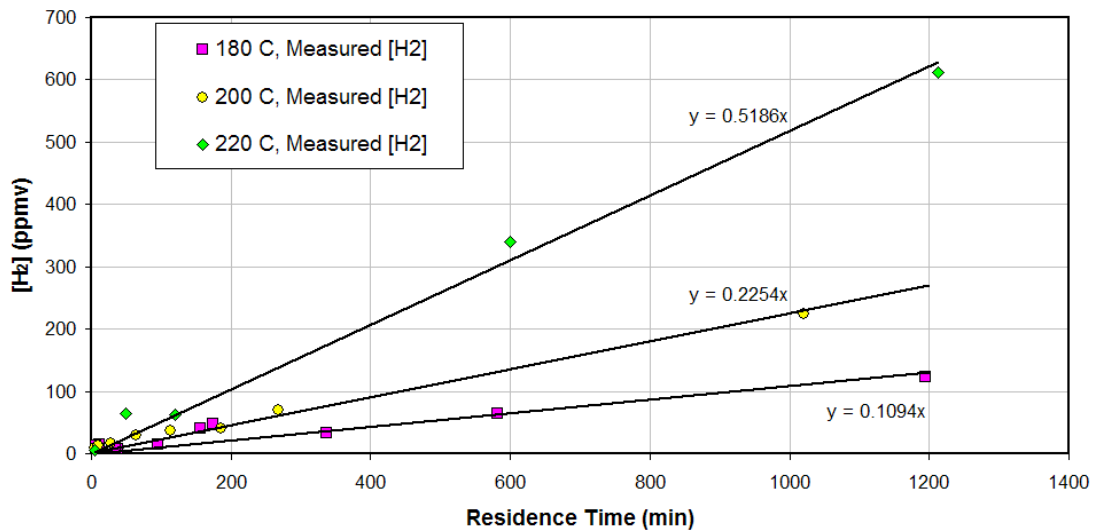


Figure 68: Permeation test results

5.2.2 Tensile Test Results

Each thin tensile specimen failed at the center of the gauge section. Macroscopic pictures were taken of each fractured specimen and can be seen in Figure 69 through Figure 80.



Figure 69: 316 sample 1 tested as received



Figure 70: 316 sample 2 tested as received



Figure 71: 316 sample 3 charged in 100°C air



Figure 72: 316 sample 4 charged in 100°C air



Figure 73: 316 sample 5 charged in 100°C H₂



Figure 74: 316 sample 6 charged in 100°C H₂



Figure 75: 316L sample L1 tested as received



Figure 76: 316L sample L2 tested as received



Figure 77: 316L sample L3 charged in 100°C air



Figure 78: 316L sample L4 charged in 100°C air



Figure 79: 316L sample L5 charged in 100°C H₂



Figure 80: 316L sample L6 charged in 100°C H₂

To determine the measurable material properties for each test and to compare results, data was organized into stress-strain curves. Results for SS 316 are shown in Figure 81 and those for SS 316L are shown in Figure 82. A summary of the test conditions and results is located in Table 1 (reported values of ϵ_f were calculated from a 25.4 mm gauge length). It can be seen that no appreciable pattern is noticed from one test condition to the next, and variations most likely due to experimental variability.

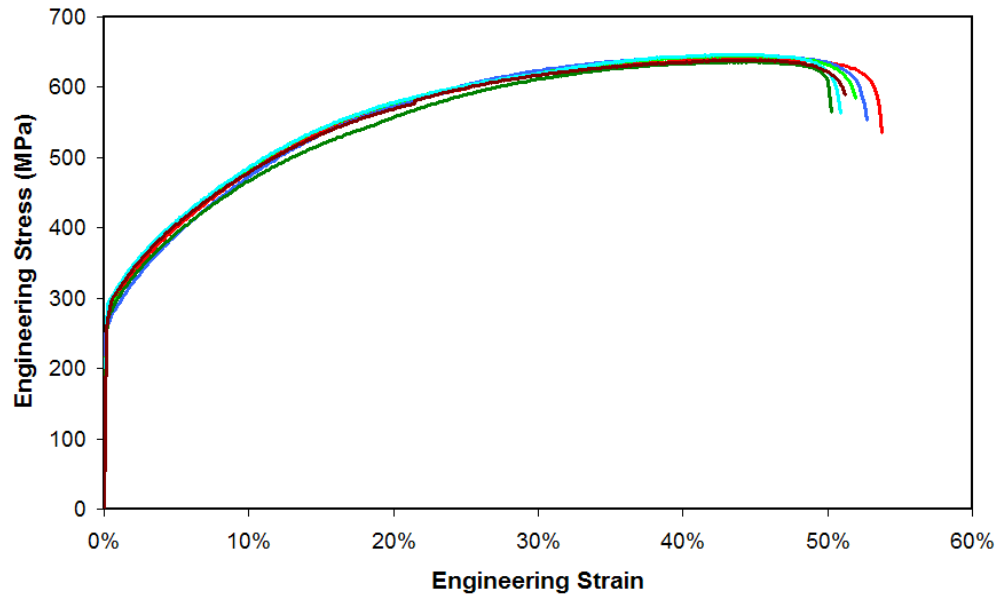


Figure 81: Stress-strain curves of samples 1 through 6

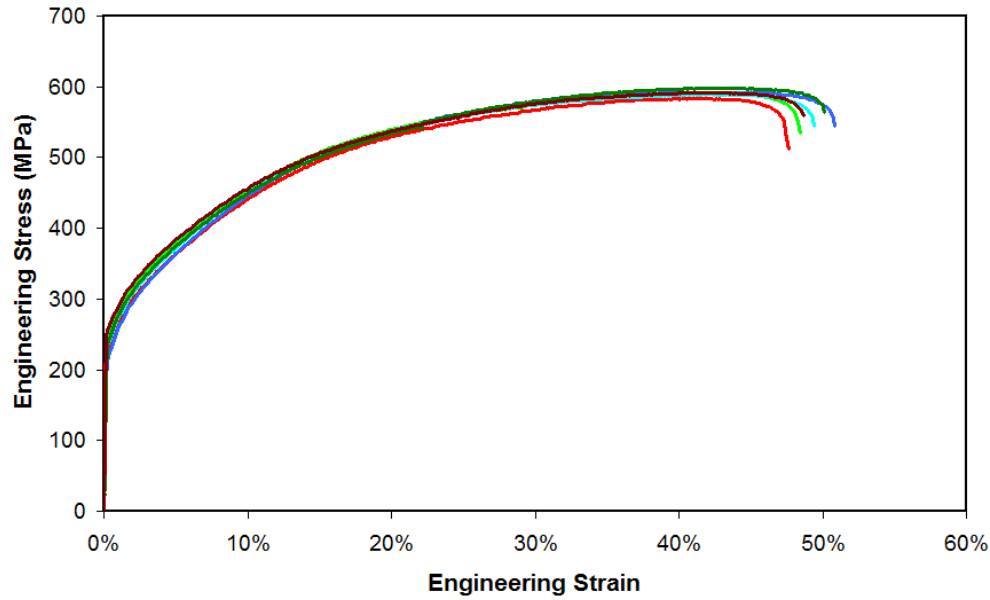


Figure 82: Stress-strain curves of samples L1 through L6

Table 13: Hydrogen charge tensile test results

Specimen ID	Material	Charge Conditions			σ_{ys} (MPa)	σ_{UTS} (MPa)	ϵ_f (%)
		T (days)	T (K)	Medium			
1	316	As-received			281.6	640.3	58.0
2	316	As-received			268.9	645.0	60.1
3	316	14	373	Air	284.7	644.6	59.4
4	316	14	373	Air	297.8	646.6	56.3
5	316	14	373	70 MPa H ₂	274.7	636.5	59.0
6	316	14	373	70 MPa H ₂	285.6	638.9	59.8
L1	316L	As-received			233.6	583.7	51.8
L2	316L	As-received			218.9	592.2	53.5
L3	316L	14	373	70 MPa H ₂	242.3	590.7	54.8
L4	316L	14	373	70 MPa H ₂	240.8	589.2	55.8
L5	316L	14	373	70 MPa H ₂	241.9	597.8	57.3
L6	316L	14	373	70 MPa H ₂	262.7	591.6	55.3

5.2.3 Scanning Electron Microscopy

Scanning electron microscopy was used to characterize the fracture of each thin tensile specimen in each tested condition. Representative micrographs are shown in Figure 83 through Figure 94 taken at magnifications of 300 and 1000 times. It was only necessary to examine one specimen from each test condition. Similar to the tensile data, there was no appreciable differences observed in the fracture surfaces of specimens charged in different conditions. All surfaces were comprised mostly of microvoid coalescence, typical of the ductile failure predictably exhibited by austenitic stainless steels 316 and 316L.

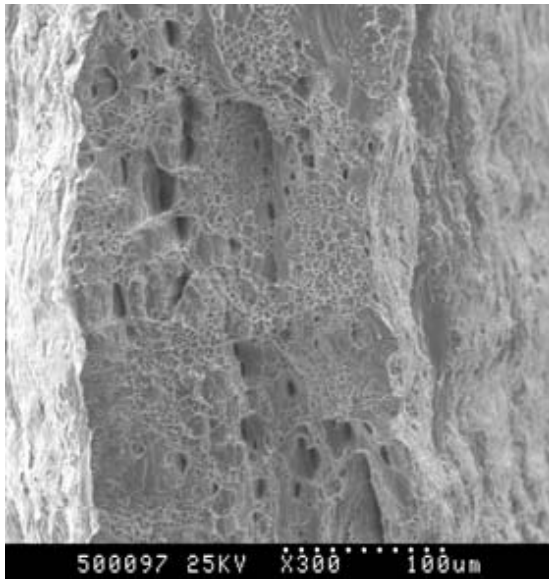


Figure 83: Sample 1 tested as-received (300x)

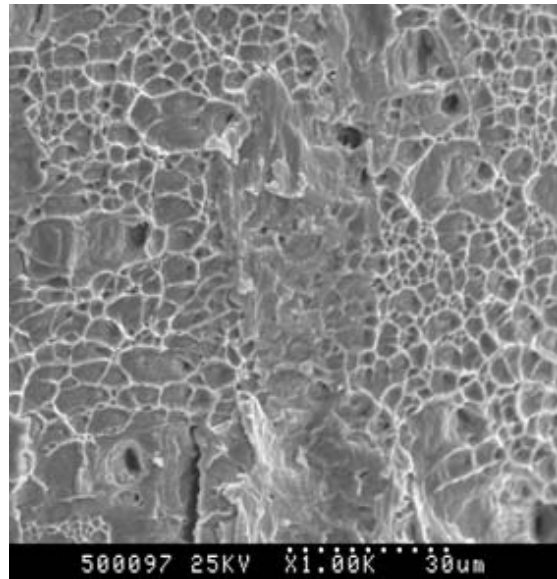


Figure 84: Sample 1 tested as-received (1000x)

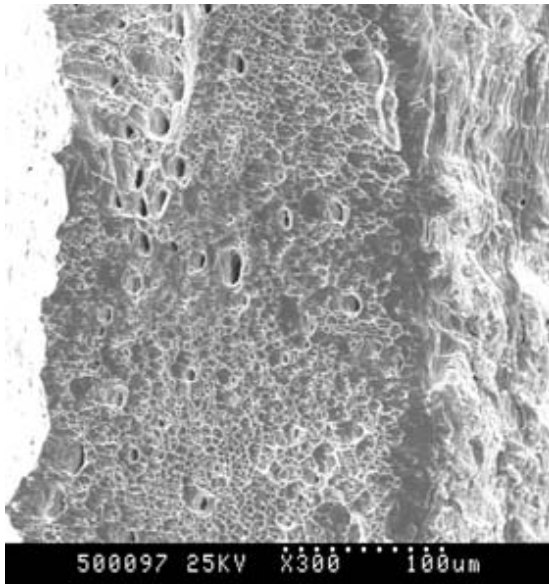


Figure 85: Sample 4 thermally aged (300x)

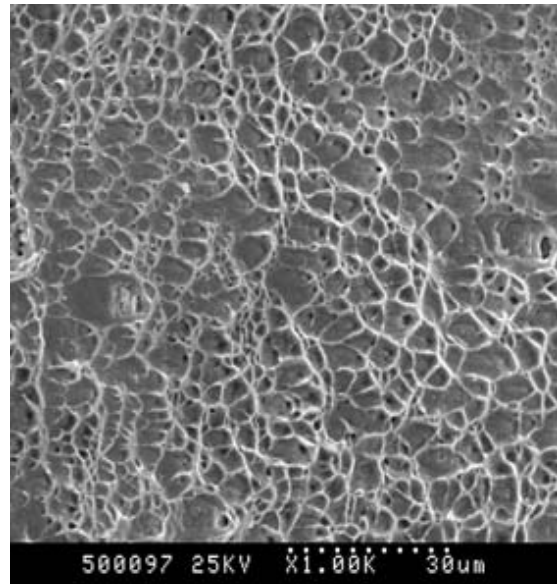


Figure 86: Sample 4 thermally aged (1000x)

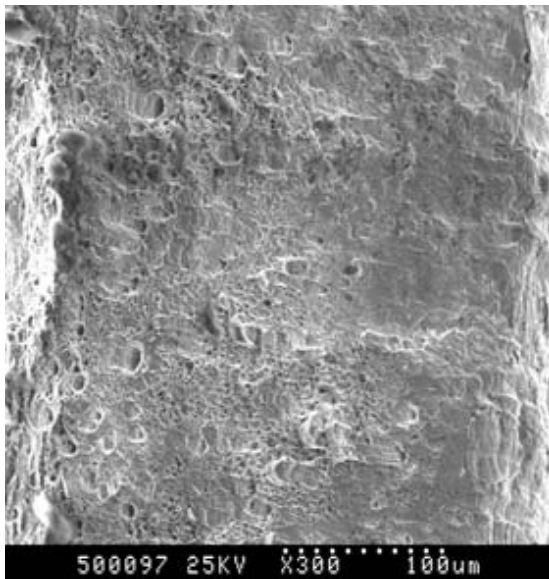


Figure 87: Sample 6 hydrogen charged (300x)

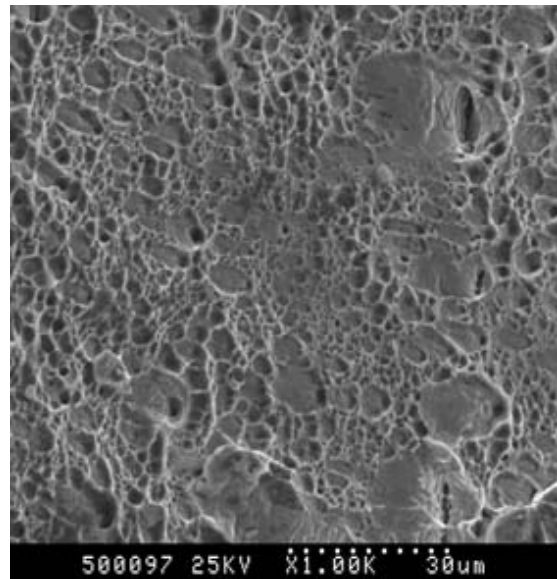


Figure 88: Sample 6 hydrogen charged (1000x)

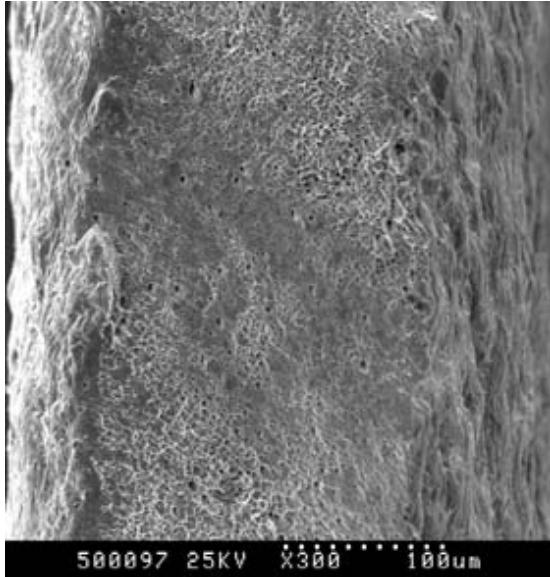


Figure 89: Sample L1 tested as-received (300x)

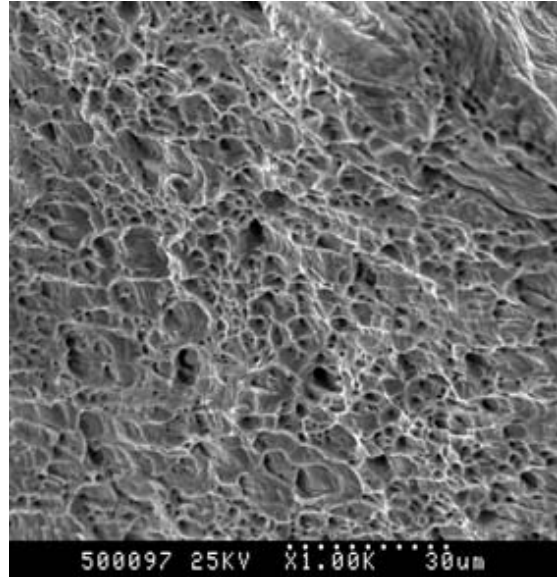


Figure 90: Sample L1 tested as-received (1000x)

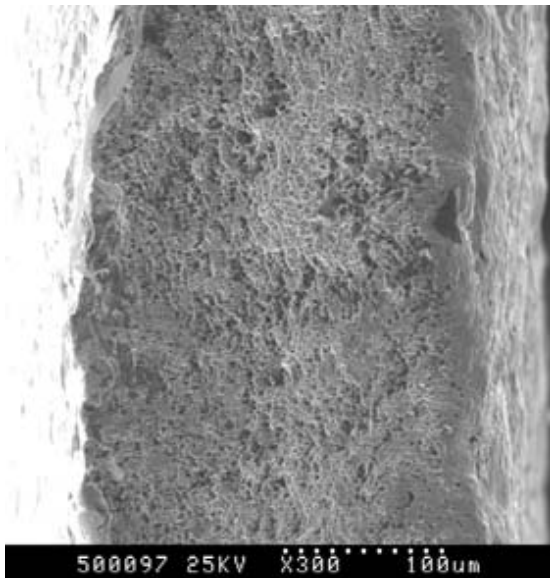


Figure 91: Sample L4 thermally aged (300x)

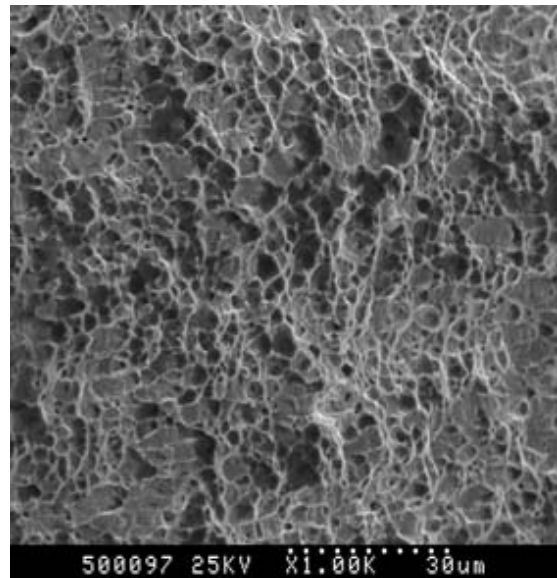


Figure 92: Sample L4 thermally aged (1000x)

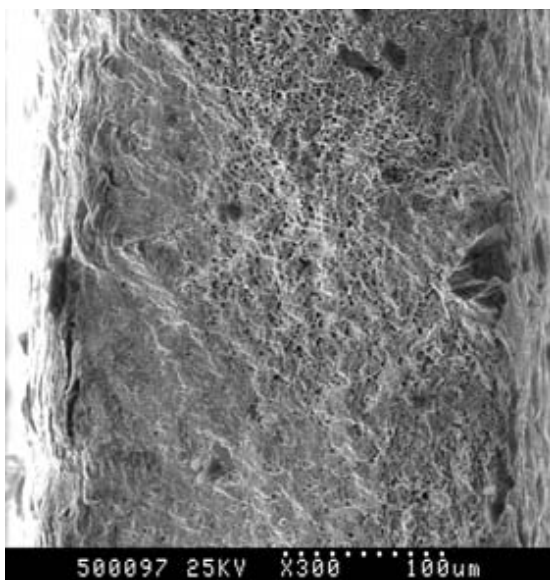


Figure 93: Sample L6 hydrogen charged (300x)

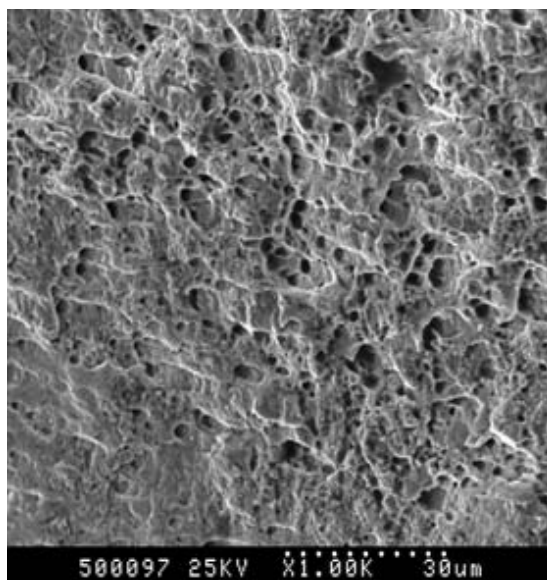


Figure 94: Sample L6 hydrogen charged (1000x)

6.0 Discussion

In the results section of this thesis, we have compared changes in material properties of SS 316 and 316L under different test conditions. Following are notable observations worthy of further discussion.

- Permeation properties of hydrogen through austenitic stainless steel
- Influence of phase stability on hydrogen embrittlement
- Martensite's role in hydrogen embrittlement
- Bulk versus surface effects of solute hydrogen
- Effect of temperature on both phase stability and hydrogen embrittlement
- Dependence of embrittling effects on hydrogen gas pressure

By reviewing the results and observations and comparing to literature, these points will be systematically discussed in preparation for the conclusions drawn in section 8.0.

6.1 Permeation Properties of SS 316L

As expected, the permeability of SS 316L was measured to be slightly different than values reported in literature. This was likely due to the presence of a surface oxide layer, which is more representative of the state of the steel used in hydrogen components. Fick's Law of diffusion (equation 16) was used to check the validity of the results and to calculate a permeability value.

$$J = P_H \frac{\sqrt{P}}{L} \quad [16]$$

where J is the flux, and P_H is the permeability. Flux is alternatively expressed in equation 17.

$$J = \frac{n_H}{At} \quad [17]$$

where n_H is moles of hydrogen, and A is exposed area. Expressions for the number of moles of hydrogen and nitrogen gas:

$$n_H = P_H \frac{At}{L} \sqrt{P} \quad [18]$$

$$n_N = \frac{P_N V}{RT} \quad [19]$$

can be combined to give the atomic ratio:

$$\frac{n_H}{n_N} = P_H \frac{At}{L} \sqrt{P} \frac{RT}{P_N V} \quad [20]$$

where n_N is moles of nitrogen, and P_N is nitrogen pressure. A plot of molar ratio versus time then provides a linear relation with a slope in terms of P_H . Using slopes of the linear curve fits shown in Figure 68, a value for permeability was calculated at each of the three temperatures. Results for measured permeabilities are located in Table 14.

Table 14: Measured permeability values

T (K)	P_H (mol m/(s m ² MPa ^{1/2}))
453	3.21×10^{-12}
473	6.34×10^{-12}
493	1.40×10^{-11}

Like diffusivity, permeability follows an Arrhenius-type dependence on temperature:

$$P_H = P_o \exp\left(\frac{-E_p}{RT}\right) \quad [21]$$

Here, P_o is permeability at absolute zero, and E_p is permeation energy. By taking the natural log of Equation 23, it is represented as:

$$\ln(P_H) = \ln(P_o) + \frac{-E_p}{RT} \quad [22]$$

A plot of $\ln(P_H)$ versus $1/T$ would then produce a linear fit with a slope of $-E_p/R$ and y-intercept of $\ln(P_o)$. As shown in Figure 95, a very reasonable linear fit can be applied to a plot of $\ln(P_H)$ versus $1/T$, having a R^2 value of 0.9953.

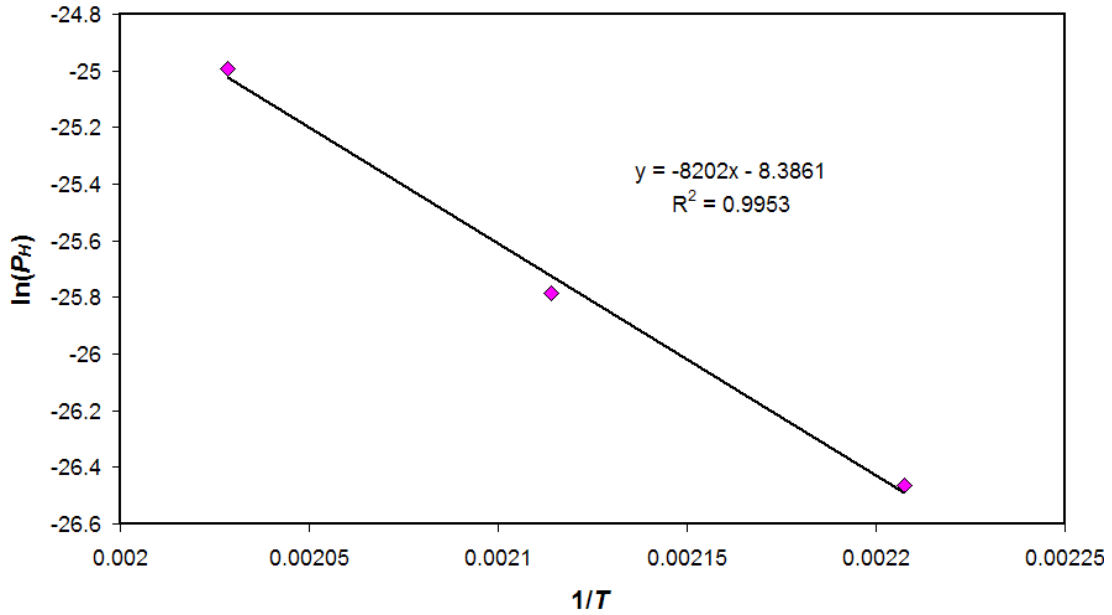


Figure 95: Permeation test $\ln(P_H)$ versus $1/T$

As reported by Oriani et al.⁵⁶, a polished sample of SS 316 (free of surface oxides) has a P_o value of $4.82 \times 10^{-4} \text{ mol m/(s m}^2 \text{ MPa}^{1/2})$ and an E_p value of $6.49 \times 10^4 \text{ J/mol}$. As calculated from the linear fit shown in Figure 95, permeation testing resulted in a P_o value of $2.28 \times 10^{-4} \text{ mol m/(s m}^2 \text{ MPa}^{1/2})$ and an E_p value of $6.82 \times 10^4 \text{ J/mol}$. Not only did the results provide additional material properties relevant to the investigation, but they also confirmed that hydrogen sufficiently penetrates the material. The obtained data validates the calculations for hydrogen saturation and confirms that the estimated hydrogen concentration in the tensile samples should be correct.

6.2 Phase Stability and Hydrogen Embrittlement

The chemistries of the two alloys tested differed only in their nickel contents. Seemingly, this has a subtle effect on their mechanical properties, but great influence on their SFEs and, thus, their phase stabilities. By comparing the performance of the two alloys, it clearly demonstrated that phase stability is an important factor in resistance to hydrogen embrittlement of austenitic stainless steels. Based on the test results, Figure 96 illustrates the generalized regimes of austenite stability as a function of temperature and nickel content. It can be seen here that stability of the austenite phase is primarily dependent on nickel content, but enhanced with a decrease in temperature. Embrittlement will occur when the austenite phase is unstable, whether the instability is due to chemistry or temperature.

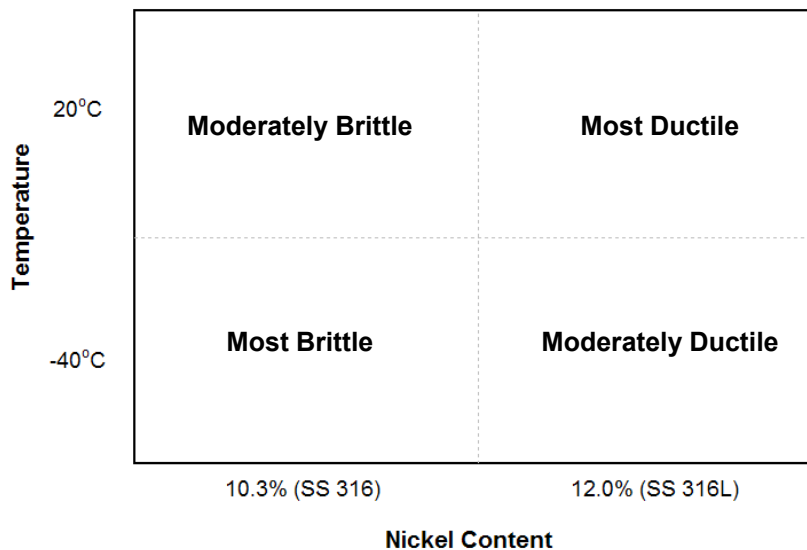


Figure 96: Austenite phase stability grid

A separate issue remains regarding hydrogen's participation in the phase transformation. At all temperatures, the ductility of SS 316L revealed no dependence on gaseous atmosphere – elongation and reduction of area were the same regardless of the presence of helium or hydrogen. Alternatively, it was more difficult to compare the martensite formation in SS 316. It can be argued that since more martensite was formed

in a helium environment than in hydrogen, martensite must not be responsible for the failure, but the samples were pulled to different strains before the martensite measurement was made. Because there were large variations in elongation to failure, the martensite contents cannot be directly compared. To adequately evaluate, samples should be deformed to equal strains in each condition and martensite content measurements should be taken. Since martensite is a stronger phase than austenite, a method for detecting its formation is by examining the shape of the stress-strain curve. As shown in Figure 36 and Figure 37, whether tested in helium or hydrogen, the shape of the deformation curve remains the same. Similar results were found in testing performed by Han et al.¹³. Although further testing should be performed to confirm it, this is evidence that hydrogen did not affect the stability of the austenite phase.

Several researchers have claimed that the presence of solute hydrogen will decrease the stability of the austenite phase^{27-29,32}. Although their methods and test practices are sound, the conditions are very different and are not relevant to a strictly gaseous system. Cathodic charging will nominally produce much larger hydrogen concentrations at the surface, with an enormous gradient, than can be obtained under the most extreme operating conditions in a gaseous environment expected in the hydrogen vehicle industry³⁰. The metallic lattice is heavily strained and spontaneous phase transformation can occur. Also, aside from the phase transformation, the simple presence of large hydrogen concentrations will impose a compressive stress at the surface of the material. For these reasons, it is extremely important to test materials according to their intended use. Previous claims made about hydrogen embrittlement based on cathodically charged samples may not necessarily apply to pressurized gas conditions.

6.3 Martensite's Role in Hydrogen Embrittlement

Supporting the findings in this thesis, reporting by Han et al.¹³ opposed the idea that strain-induced martensite contributes to hydrogen embrittlement of stable austenitic stainless steels. Rather than resulting from the formation of strain-induced martensite, it was claimed that hydrogen embrittlement was due to a low value of stacking fault energy. Since the martensite phase is nucleated from a stacking fault, the two cases are strongly

related. A lower value of stacking fault energy results in a slip system providing more faulted planes (i.e. increased nucleation of martensite). An alternate suggestion is that the growth of the martensite phase, rather than its nucleation, is hindered. Their results give the initial impression that a higher content of martensite reduces the consequences of testing in a hydrogen atmosphere. This is not necessarily true. A change in temperature will not only affect the rate of martensite formation, but also the diffusivity of hydrogen. At very low temperatures, hydrogen diffusion in austenitic stainless steels slows appreciably. The failure mechanism faces competing influences: hydrogen diffuses faster through strain-induced martensite than austenite, and martensite is formed more easily at low temperatures, but low enough temperatures will nearly halt hydrogen diffusion.

Work by Shivanyuk et al.¹² compared behavior of materials of varying stacking fault energies. It was shown that a lower stacking fault energy promoted transformation from austenite to martensite, but the manner in which they decrease the stacking fault energy altered the chemistry of the specimen. In order to directly compare the effect of martensite content, all other variables must be eliminated, including a change in chemistry. Because the martensite transformation is diffusionless and does not involve a change in chemistry, the samples of similar chemistry can be fully austenitic or contain martensite. To be able to directly compare the results, the variable of chemistry must first be eliminated.

6.4 Surface Versus Bulk Hydrogen Concentration

From the tests performed, it can be concluded that hydrogen embrittlement is more prevalent when hydrogen exists at the material surface at relatively low concentrations (~335 atomic ppm). This is evident by first comparing the lack of embrittlement in samples that are gaseously pre-charged and tested in air versus those simply tested in pressurized hydrogen. By looking at their stress-strain curves and their fracture surfaces, no change is seen between the charged and uncharged conditions. By charging specimens at 100°C in 70 MPa hydrogen, the bulk hydrogen concentration will be larger than the surface concentration of uncharged samples tested in 25 MPa hydrogen.

Although different experiments were performed, Brass and Chêne⁶⁵ used similar sample preparation as in the aforementioned hydrogen charge tests. By gaseously charging thin specimens in 18 MPa hydrogen at 600°C, they reported an absorbed hydrogen concentration of 2854 atomic ppm. Their work, however, included no results from mechanical testing for basis of comparison. Because the temperature has greater influence on the surface concentration than the pressure (see equations 6, 11, and 21), a higher solute hydrogen concentration can be reached. Although it is possible to perform the same tests in more severe conditions, testing was performed according to industry standards with respect to maximum operating temperature and pressure¹. In other words, it may be possible to induce hydrogen embrittlement by increasing hydrogen charge temperature, but the situation is not realistic and is beyond a worst-case scenario.

Witnessing a greater effect from hydrogen environment than hydrogen charge testing supports the hydrogen enhanced decohesion mechanism of embrittlement. It has been stated that hydrogen atoms are attracted to the tensile field ahead of a crack tip⁸⁻¹⁰. According to the HEDE theory, the presence of solute hydrogen atoms decreases the electron charge density between the metallic atoms, resulting in the tensile separation of atoms in a planar nature^{12,13,15}. This is also evidenced in the formation of surface cracks when tested in a hydrogen atmosphere.

6.5 Effect of Temperature on Hydrogen Embrittlement

Aside from the well established effect temperature has on the strength of a material, it also had a significant effect on hydrogen embrittlement. The results of the hydrogen environment tensile tests show that decreasing test temperature to -40°C has a significant effect on the ductility of SS 316. In both alloys, the mode of failure remained ductile when tested in helium at a low temperature. The values of elongation and reduction in cross-sectional surface area varied only marginally. Once tested in 25 MPa hydrogen gas at -40°C, the elongation to failure of SS 316 dropped by over 35%, as opposed to a drop of only 12% at room temperature (the reduction in cross-sectional surface area behaved similarly). Considering the large drop in elongation to failure, it is more surprising to see areas of ductility in the fracture surface (see Figure 62). Hydrogen

even had a slight effect on the ductility of SS 316L at -40°C . The stereo micrograph in Figure 45 shows multiple surface cracks and the SEM micrograph in Figure 67 show fracture of a planar nature in sample TL4. The elongation to failure dropped by about 4%, while the reduction in cross-sectional surface area dropped by about 15%. In the case of brittle fracture, the elongation-to-failure is likely an over-estimation due to difficulties in re-assembling a fractured piece.

In a way, the results are counter-intuitive because such a drop in temperature corresponds to an extremely large drop in diffusion of hydrogen. Not only will there be a decrease in the interstitial movement of hydrogen through the lattice, but the surface concentration will be much smaller. According to Herms et al., the brittle fracture of an alloy is limited to the depth of hydrogen penetration². In the testing performed, ductile regions were observed in the center of the sample tested in hydrogen at -40°C , but the depth of brittle fracture exceeds the expected depth of hydrogen penetration by several orders of magnitude.

In all cases of hydrogen atmosphere testing, brittle surface cracks were formed across the entire gauge section. At room temperature, localization of plastic deformation concentrates the formation of surface cracks to the neck region. Here, the brittle surface cracks propagate across the entire fracture surface, creating a brittle fracture surface. According to research by Glenn Beltz et al., a fracture surface will be ductile “if dislocation emission occurs at a lower load than that required for crack propagation”⁶⁶. Figure 97 (adapted from Beltz et al.⁶⁶) illustrates two cases of crack propagation. On the left, a sharp surface crack intersecting a slip plane experiences mode I loading (i.e. opening of the crack faces in the absence of shear). The upper right image portrays a situation where dislocation emission occurs at a lower load and, thus, crack-tip blunting occurs. Since crack propagation ceases, the remaining ligament is eventually overloaded, failing in a ductile fashion. In the lower right image, a load high enough for dislocation emission cannot be achieved before the crack propagates by cleavage decohesion.

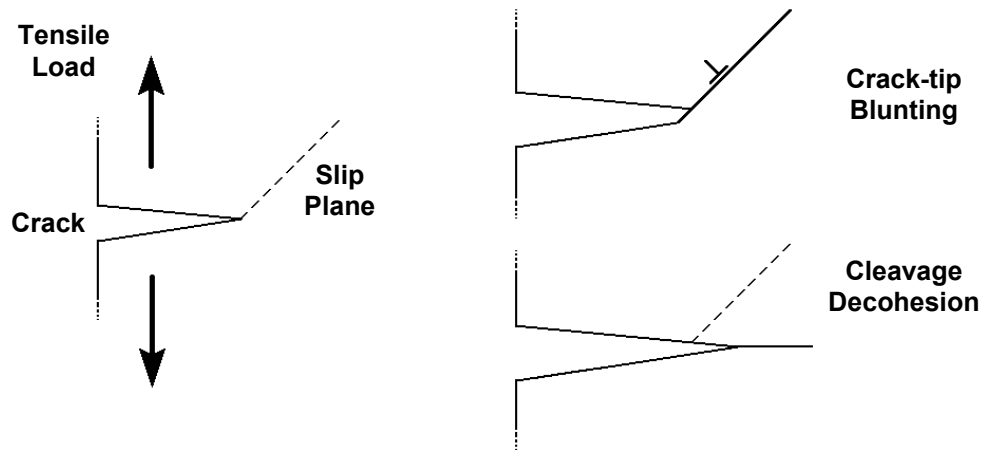


Figure 97: Surface crack experiencing dislocation emission versus crack propagation

In a -40°C hydrogen atmosphere, it seems as though dislocation emission occurs more readily than crack propagation in both SUS 316 and 316L. Whether this change is due to change in material properties as lower temperatures or the inherent phase transformation, it is still unclear. A study performed by G. Xu et al. indicates that blunting of a propagating cleavage crack may be caused by background plastic relaxation⁶⁷. An increase in volume associated with the austenite-to-martensite transformation may provide such a plastic relaxation. As previously mentioned, hydrogen is attracted to the tensile field ahead of a crack tip due to a chemical potential gradient⁸⁻¹⁰. The absorption of hydrogen may also play a role in stress relaxation. Alternatively, it is possible that the strain-induced phase transformation provides the local strengthening required for shifting modes of crack propagation. The load necessary for dislocation emission then occurs below that of brittle cleavage propagation, thus permitting a ductile overload of the remaining ligament.

7.0 Future Work

The concentration of hydrogen exposed to the surface of hydrogen environment tensile samples is a function of pressure as well as temperature. According to equation 6 (page 15), the surface concentration is proportional to the square root of the applied gas pressure. As it has been determined that embrittlement occurs largely due to surface effects of hydrogen concentration, it is imperative that materials be tested in pressures equal to or greater than the intended operating pressure.

To support future work, prototype test equipment was designed and built to provide testing up to 85 MPa hydrogen pressure. With the new test equipment, a material's susceptibility to hydrogen environment embrittlement can be characterized over a complete range of test pressures. Difficulties remain, however, in maintaining a gas-tight seal at low temperatures. The nitrile o-rings used are effective in preventing leaks at room temperature, but a decrease in temperature causes a decrease in the material's compliance, preventing it from forming an acceptable seal. To remedy the situation, the equipment can be modified to include a method of locally heating the elastomer seal. Care must be taken to avoid implementing potential ignition sources in areas of potential hydrogen leaks.

A test program must also be developed to help establish hydrogen's influence in the formation of martensite. To do so, a tensile sample can be strained to a desired value, and then removed and magnetically tested for martensite content. The process can be repeated numerous times to develop a relationship between strain and martensite formation in a given environment. By comparing the results between hydrogen and helium atmospheres at various temperatures and pressures, the effect of hydrogen can be determined in any condition. Alternatively, the presence of martensite ahead of a growing crack can be examined using a fatigue precracked compact tension specimen. In a helium atmosphere, the compact tension specimen can be loaded to propagate the precrack. The helium should then be replaced with hydrogen and the crack propagated further. A metallographic examination could then reveal if a difference exists between martensite formation in the regions of crack propagation in helium versus hydrogen.

The fatigue behavior of a material in a hydrogen atmosphere is another area of interest within the field of hydrogen compatibility testing. Components for hydrogen storage and delivery are experiencing constantly fluctuating stresses. For lifecycle assessment, it is important to study the effects of hydrogen on the initiation and propagation of a fatigue crack. The newly developed high-pressure equipment can also be adapted to accommodate specimens for cyclic loading applications necessary for fatigue studies. The cycles required to nucleate a crack and the crack growth rate can be quantified over a range of applied stress intensities and contrasted to that in air.

8.0 Conclusions

Although much more testing is required to approach certainty, many of the questions posed have been answered in this thesis. The most obvious of the conclusions is that SS 316L outperforms SS 316 with regards to hydrogen embrittlement resistance. The mechanical properties are very similar, but having higher nickel content provides 316L with a higher stacking fault energy, and thus higher austenite phase stability. When selecting an austenitic stainless steel compatible with high-pressure hydrogen environments, after satisfying strength and toughness requirements, requirements for stacking fault energy should be addressed.

The result most relative to the field of material testing and certification for use in the hydrogen industry is that hydrogen environment embrittlement is dominant at the material surface. Once a crack forms, a constant supply of hydrogen to its tip will facilitate propagation via the decohesion model of hydrogen embrittlement. This discovery helps focus the testing for material compatibility testing in pressurized hydrogen environments. It was determined that hydrogen environment tensile testing is more useful than hydrogen charge testing in inducing hydrogen embrittlement. Tests can be performed for much cheaper because they are quicker and involve less preparation. The test also better replicates the natural state of high-pressure hydrogen components. It is important, however, to refine performance qualifications. Stainless steel 316 has proven to be adequate for high-pressure use through years of service and very few unexpected failures. The hydrogen environment tensile tests caused embrittlement because very large stresses and strains were involved.

In reality, stresses will remain below those required to yield the material, so embrittlement will not normally occur. Thus, it is suggested that a proper test for material compatibility involve imposing a predetermine amount of strain in a hydrogen environment of the intended operating pressure. The imposed strain should be based on a reasonable safety factor of the strain to reach the material's yield point. Since the most important goal is to prevent the formation of stress concentrations caused by surface cracks, the sample would be removed from the hydrogen environment and examined for such cracks. A set of pass/fail criteria would need to be established based on numerous

additional hydrogen environment tensile tests and evidence from the history of successful and unsuccessful candidate materials.

References

- [1] Philip Horacek, P.Eng. Gas Systems Engineering, *Powertech Labs, Inc.* Personal communication, June 8th, 2007.
- [2] E. Herms, J.M. Olive, and M. Puiggali. “Hydrogen Embrittlement of 316L Type Stainless Steel”. *Materials Science and Engineering A272* (1999) 279-283.
- [3] S.C. Chou and M.M. Makhlof. “The Effect of Ion Implanting on Hydrogen Entry Into Metals”. *Metallurgical and Materials Transactions A 30* (1999) 1535-1540.
- [4] Richard A. Oriani, John P. Hirth, and Michael Smialowski. “Hydrogen Degradation of Ferrous Alloys”. *Noyes Publications* (1985).
- [5] C. Gabrielli, G Maurin, L. Mirkova, H. Perrot, and B Tribollet. “Transfer Function Analysis of Hydrogen Permeation Through an Iron Membrane in a Devanathan Cell”. *Impedance Contributions Online 2* (2004) P1.1-P1.9.
- [6] H.G. Nelson. *Treatise on Materials Science and Technology 25* (1981) 291.
- [7] H.W. Liu and P.J. Ficalora. “Catalytic Dissociation, Hydrogen Embrittlement, and Stress Corrosion Cracking”. *International Journal of Fracture Mechanics 8 2* (1972) 223-226.
- [8] C. Pan, W.Y. Chu, Z.B. Li, D.T. Liang, Y.J. Su, K.W. Gao, and L.J. Qiao. “Hydrogen Embrittlement Induced By Atomic Hydrogen and Hydrogen-Induced Martensites in Type 304L Stainless Steel”. *Materials Science and Engineering A351* (2003) 293-298.

- [9] Tsong-Pyng Perng and C.J. Altstetter. "Effects of Deformation on Hydrogen Permeation in Austenitic Stainless Steels". *Acta Metallurgica* 34 9 (1986) 1771-1781.
- [10] Daniel P. Abraham and Carl J. Altstetter. "Hydrogen-Enhanced Localization of Plasticity in an Austenitic Stainless Steel". *Metallurgical and Materials Transactions* 26A (1995) 2859-2871.
- [11] Wolfgang Losch. "Hydrogen Embrittlement: A New Model for the Mechanism of Reduction of Metallic Cohesion". *Scripta Metallurgica* 13 (1979) 661-664.
- [12] V.N. Shivanyuk, J. Foct, V.G. Gavriljuk. "On a Role of Hydrogen-Induced ϵ -Martensite in Embrittlement of Stable Austenitic Steel". *Scripta Materialia* 49 (2003) 601-606.
- [13] G. Han, J. He, S. Fukuyama, and K. Yokogawa. "Effect of Strain-Induced Martensite on Hydrogen Environment Embrittlement of Sensitized Austenitic Stainless Steels at Low Temperatures". *Acta Materialia* 46 13 (1998) 4559-4570.
- [14] A. Toshimitsu Yokobori Jr., Takenao Nemoto, Koji Satoh, and Tetsuya Yamada. "The Characteristics of Hydrogen Diffusion and Concentration Around a Crack Tip Concerned With Hydrogen Embrittlement". *Corrosion Science* 44 (2002) 407-424.
- [15] V.G. Gavriljuk, V.N. Shivanyuk, and J. Foct. "Diagnostic Experimental Results on the Hydrogen Embrittlement of Austenitic Steels". *Acta Materialia* 51 (2003) 1293-1305.
- [16] Harrison C. White. "Atomic Force Constants of Copper From Feynman's Theorem". *Physical Review* 112 4 (1958) 1092-1105.

- [17] J.D. Hermida, and A. Roviglione. “Stacking Fault Energy Decrease in Austenitic Stainless Steels Induced By Hydrogen Pairs Formation”. *Scripta Materialia* 39 8 (1998) 1145-1149.
- [18] Pekka Nevasmaa. “Predictive Model for the Weld Metal Hydrogen Cracking in High-Strength Multipass Welds”. *Acta University of Oulu* 191 (2003).
- [19] Y. Liang, D.C. Ahn, P. Sofronis, R.H. Dodds Jr., D. Bammann. “Effect of Hydrogen Trapping on Void Growth and Coalescence in Metals and Alloys”. *Mechanics of Materials* 40 (2008) 115-132.
- [20] I.M. Robertson. “The Effect of Hydrogen on Dislocation Dynamics”. *Engineering Fracture Mechanics* 64 (1999) 649-673.
- [21] P. Sofronis, Y. Liang, and N. Aravas. “Hydrogen Induced Shear Localization of the Plastic Flow in Metals and Alloys”. *European Journal of Mechanics A/solids* 20 (2001) 857-872.
- [22] V.N. Shivanyuk, B.D. Shanina, A.V. Tarasenko, V.G. Gavriljuk, and J. Foct. “Effect of Hydrogen on Atomic Bonds in Austenitic Stainless Steel”. *Scripta Materialia* 44 (2001) 2765-2773.
- [23] A.G. Varias and A.R. Massih. “Hydride-Induced Embrittlement and Fracture in Metals – Effect of Stress and Temperature Distribution”. *Journal of the Mechanics and Physics of Solids* 50 (2002) 1469-1510.
- [24] K. Sieradzki and P. Ficalora. “The Mechanism of Hydrogen Embrittlement Adsorption or Decohesion”. *Scripta Metallurgica* 14 (1980) 641-644.
- [25] J. Völkl, and H. Wipf. “Diffusion of Hydrogen in Metals”. *Hyperfine Interactions*, 8 (1981) 631-638.

- [26] J. Toribio. "The Role of Crack Tip Strain Rate in Hydrogen Assisted Cracking". Corrosion Science, 39 9 (1997) 1687-1697.
- [27] Q. Yang, and J.L. Luo. "Martensite Transformation and Surface Cracking of Hydrogen Charged and Outgassed Type 304 Stainless Steel". Materials Science and Engineering A288 (2000) 75-83.
- [28] Q. Yang, L.J. Qiao, S. Chiovelli, and J.L. Luo. "Critical Hydrogen Charging Conditions for Martensite Transformation and Surface Cracking in Type 304 Stainless Steel". Scripta Materialia 40 11 (1999) 1209-1214.
- [29] N. Narita, C.J. Altstetter, and H.K. Birnbaum. "Hydrogen-Related Phase Transformations in Austenitic Stainless Steels". Metallurgical Transactions 13A (1982) 1355-1365.
- [30] M. Hoelzel, S.A. Danilkin, H. Ehrenberg, D.M. Toebbens, T.J. Udovic, H. Fuess, and H. Wipf. "Effects of High-Pressure Hydrogen Charging on the Structure of Austenitic Stainless Steels". Materials Science and Engineering A 384 (2004) 255-261.
- [31] S. Sugiyama, H. Ohkubo, M. Takenaka, K. Ohsawa, M.I. Ansari, N. Tsukuda and E. Kuramoto. "The Effect of Electrical Hydrogen Charging on the Strength of 316 Stainless Steel". Journal of Nuclear Materials 283-287 (2000) 863-867.
- [32] Adriana Estela Pontini and Jorge Daniel Hermida. "X-Ray Diffraction Measurement of the Stacking Fault Energy Reduction Induced By Hydrogen in an AISI 304 Steel". Scripta Materialia 37 11 (1997) 1831-1837.

- [33] T. Inamura, K. Takashima, and Y. Higo. “Crystallography of Nanometre-Sized α' -Martensite Formed at Intersections of Mechanical γ -Twins in an Austenitic Stainless Steel”. *Philosophical Magazine* 83 8 (2003) 935-954.
- [34] J.C. Bavay. “Austenitic Stainless Steels” in *Stainless Steels*, P. Lacombe, B. Baroux, G. Beranger, Editors (1993) 551-591.
- [35] I. Karaman, H. Sehitoglu, Y.I. Chumlyakov, and H.J. Maier. “The Deformation of Low-Stacking-Fault-Energy Austenitic Steels”. *JOM* 54 7 (2002) 31-37.
- [36] Kevin Spencer. “The Work Hardening of Austenitic Stainless Steels, Applied to the Fabrication of High-Strength Conductors”. PhD Thesis, McMaster University (2004).
- [37] L. Remy and A. Pineau. “Observation of Stacked Layers of Twins and ϵ Martensite in a Deformed Austenitic Stainless Steel”. *Metallurgical Transactions* 5 (1974) 963-965.
- [38] S. Allain, J.P. Chateau, O. Bouaziz, S. Migot and N. Guelton. “Correlations Between the Calculated Stacking Fault Energy and the Plasticity Mechanisms in Fe-Mn-C Alloys”. *Materials Science Engineering A* 387-389 (2004) 158-162.
- [39] Alfredo Juan, Lilian Moro, Graciela Brizuela, and Estela Pronsato. “The Electronic Structure and Bonding of an Hydrogen Pair Near a FCC Fe Stacking Fault”. *International Journal of Hydrogen Energy* 27 (2002) 333-338.
- [40] G.B. Olson, Morris Cohen. “A Mechanism for the Strain-Induced Nucleation of Martensitic Transformations”. *Journal of the Less-Common Metals* 28 (1972) 107-117.

- [41] Amar K. De, David C. Murdock , Martin C. Mataya , John G. Speer and David K. Matlock. “Quantitative Measurement of Deformation-Induced Martensite in 304 Stainless Steel by X-Ray Diffraction”. *Scripta Materialia* 50 (2004) 1445-1449.
- [42] S. Ganesh Sundara Raman, K.A. Padmanabhan. “Tensile Deformation-Induced Martensitic Transformation in AISI 304LN Austenitic Stainless Steel”. *Journal of Materials Science Letters* 13 (1994) 389-392.
- [43] C.M. Lepienski, N.K. Kuromoto, J.F.P. Souza, C.E. Foerster, F.C. Serbena, S.L.R. Silva. “Effect of Hydrogen on Mechanical Properties of Nitrided Austenitic Steels”. *Philosophical Magazine* 86 33-35 (2006) 5407-5418.
- [44] D. Hwang, L.H. Chiu, D.L. Johnson. “Gas-Phase Hydrogen Permeation and Diffusion in Vanadium”. *Journal of Materials Science Letters* 10 (1991) 605-607.
- [45] G.B. Olson and Morris Cohen. “Kinetics of Strain-Induced Martensitic Nucleation”. *Metallurgical Transactions* 6A (1975) 791-795.
- [46] J.R. Patel, and M. Cohen. “Criterion for the Action of Applied Stress in the Martensitic Transformation”. *Acta Metallurgica* 1 (1953) 531-538.
- [47] Vijay Shrinivas, S.K. Varma, and L.E. Murr. “Deformation-Induced Martensitic Characteristics in 304 and 316 Stainless Steels During Room-Temperature Rolling”. *Metallurgical and Materials Transactions* 26A (1995) 661-670.
- [48] P.J. Ferreira, and P. Müllner. “A Thermodynamic Model for the Stacking-Fault Energy”. *Acta Metallurgica* 46 13 (1998) 4479-4484.
- [49] Lin Li and T.Y. Hsu (Xu Zuyao). “Gibbs Free Energy Evaluation of the FCC (γ) and HCP (ϵ) Phases in Fe-Mn-Si Alloys”. *Calphad* 21 3 (1997) 443-448.

- [50] I.A. Yakubtsov, A. Ariapour, and D.D. Perovic. "Effect of Nitrogen on Stacking Fault Energy of FCC Iron-Based Alloys". *Acta Materialia* 47 4 (1999) 1271-1279.
- [51] J.H. Huang and C.J. Altstetter. "Internal Hydrogen-Induced Subcritical Crack Growth in Austenitic Stainless Steels". *Metallurgical Transactions A* 22 (1991) 2605-2618.
- [52] J. Chêne, M. Aucoin, R. Arnould-Laurent, P. Tison, J.-P. Fidelle. "Hydrogen Transport by Deformation and Hydrogen Embrittlement in Selected Stainless Steels". *Hydrogen Effects in Metals. The Metallurgical Society of AIME* (1980) 583-595.
- [53] F.P. Pickering. "Physical Metallurgical Development of Stainless Steels". *Proc. Conf. Stainless Steels, Gothenburg* (1984) 2-28.
- [54] ASTM International. "Standard Test Methods for Tension Testing of Metallic Materials" Designation E8 (2001) 60-81.
- [55] David S. Wilkinson. *Cambridge Solid State Science Series. Mass Transport in Solids and Fluids* (1999).
- [56] Richard A. Oriani, John P. Hirth, and Michael Smialowski. "Hydrogen Degradation of Ferrous Alloys". *Noyes Publications* (1985).
- [57] C. San Marchi. "Technical Reference on Hydrogen Compatibility of Materials – Austenitic Stainless Steels: Type 316". *Sandia National Laboratories* (2005).
- [58] Michael F. Ashby. "Materials Selection in Mechanical Design" 2nd Ed., Woburn, Massachusetts. *Butterworth-Heinemann* (1999).

- [59] UGINE & ALZ, Arcelor Group. Material data sheet UGINOX 18-12ML. <<http://www.ugine-alz.com>>. Accessed July 2007.
- [60] Chad Sinclair. Advanced Phase Transformation, MTRL 575, University of British Columbia. Lecture Notes (2006).
- [61] A.C. Larson, R.B Von Dreele. “General Structure Analysis System (GSAS)”. Los Alamos National Laboratory.
- [62] B.H. Toby. EXPGUI, a graphical user interface for GSAS. Journal of Applied Crystallography 34 (2001) 210-213.
- [63] M. Radu, J. Valy, A.F. Gourgues, F. Le Strat, and A. Pineau. “Continuous Magnetic Method for Quantitative Monitoring of Martensitic Transformation in Steels Containing Metastable Austenite”. Scripta Materialia 52 (2005) 525-530.
- [64] J. Talonen, P. Aspegren, and H. Hänninen. “Comparison of Different Methods for Measuring Strain Induced α' -Martensite Content in Austenitic Steels”. Materials Science and Technology 20 (2004) 1506-1512.
- [65] A.M. Brass, J. Chêne. “Hydrogen Uptake in 316L Stainless Steel: Consequences on Tensile Properties”. Corrosion Science 48 (2006) 3222-3242.
- [66] Glenn E. Beltz, Don M. Lipkin, Lisa L. Fischer. “Role of Crack Blunting in Ductile Versus Brittle Response of Crystalline Materials”. Physical Review Letters 82 22 (1999) 4468-4471.
- [67] G. Xu, A.S. Argon. “Critical Configurations for Dislocation Nucleation From Crack Tips”. Philosophical Magazine A 75 2 (1997) 341-367.